ENHANCEMENT OF PROLIFERATION OF SCHWANN CELLS ON MAGNETIC SILK FIBROIN SCAFFOLDS

A thesis

Submitted by

Aashna Taneja

In partial fulfillment of the requirements

for the degree of

Master of Science

In

Biomedical Engineering

TUFTS UNIVERSITY

May 2013

ADVISOR: David L. Kaplan

ABSTRACT

Peripheral nerve injury affects 2.8% of patients with trauma, presenting a critical clinical issue. The neurons regenerate their axons after injury and Schwann cells within the denervated nerve pathways support the regenerating axons. In the past decade, studies related to Schwann cells have mainly focused on delivering the cells to the repair site to promote neural cell growth but have not focused on enhancing the growth of Schwann cells to further help in increase the rate of axon regeneration. The goal of this project was to enhance the growth of Schwann cells by developing silk fibroin electrospun mats to mimic the hierarchical structure of the extracellular matrix in combination with biocompatible and biodegradable Fe_3O_4 nanoparticles with magnetic stimulations.

To accomplish this goal, varying concentrations of Fe_3O_4 nanopowders were used with silk solution to prepare electrospun mats at different voltages. A series of experiments was carried out to characterize the electrospun mats such as Scanning Electron microscopy (SEM), Transmission Electron Microscopy (TEM), Fourier Transform Infrared Spectroscopy (FTIR), X-Ray Powder Diffraction (XRD), Thermogravimetric Analysis (TGA), Superconducting Quantum Interference Device (SQUID) magnetometer testing and Instron Mechanical testing. Schwann cells (ATCC) were seeded on the mats and Alamar blue cell viability studies revealed that the growth of Schwann cells was enhanced on the mats with 7 wt. % Fe_3O_4 on Day 1. In addition, magnetic silk fibroin electropun mats had no impact on the growth and proliferation of Schwann cells indicating that these mats had no cytotoxic effects on Schwann cells. Based on these results, magnetic silk fibroin electrospun mats could be pursued as scaffolds for neural tissue engineering.

ACKNOWLEDGEMENTS

Firstly, I would like to thank my advisor Professor David Kaplan for giving me an opportunity of being a Masters student in his lab. His constructive criticism and constant guidance contributed a lot towards the accomplishment of this thesis.

I would like to extend my thanks to my committee members, Professor Peggy Cebe and Professor Qiaobing Xu for taking out the time to read my dissertation and for donating their invaluable expertise to the development of this work.

I owe sincere and earnest thankfulness to Lee W. Tien for his support, time and help that he offered at every step of the way. His thoughtful insight, knowledge and much needed criticism opened the doors for new possibilities.

Special thanks to all the people who helped me understand the techniques and equipment useful for completion of my project including Professor Peggy Cebe for helping me with XRD analysis, James D. White for teaching me ELISA detection and for donating some of his material and others at Northeastern University and Harvard university for helping me getting trained on TEM and with SQUID magnetometer. Much thanks to my colleagues at 200 Boston Avenue, especially Rod Jose and Roberto Elias for sharing their knowledge and their generosity throughout. I would also like to thank Milva Ricci for being so helpful in every possible way and Martin Hunter for all the trainings.

Most importantly, I will always be indebted & thankful to my parents, Mukesh Taneja and Asha Taneja for their unconditional love, encouragement and support that they provided me with all my life. I will never be able to repay you back for what you have given me in this lifetime. To the best brother in whole entire world, Nishant Taneja, for his love, support, encouragement and naughty acts to keep me enthusiastic, entertained and motivated to achieve my goals. This work is dedicated to you all. I would like thank my dad and my brother again for the emotional strength they provided me with all these years when mom

went away to become a beautiful angel. Mom, you were deeply missed every second. Thanks for showering your blessings from the heaven and your love, teachings, time and everything you taught me that helped me achieve my goals.

Lastly, I would like to thank my Master, Sandy Glassman and the Quemere family for being so loving, supportive and helpful and my extended family and friends back home, especially my nephew Taavish for his innocent love.

TABLE OF CONTENTS

List of Table

List of Figures

List of Figures

List of Figures

List of Figures

ENHANCEMENT OF PROLIFERATION OF SCHWANN CELLS ON MAGNETIC SILK FIBROIN SCAFFOLDS

CHAPTER 1: INTRODUCTION

1.1 TISSUE ENGINEERING TO ACHIEVE REGENERATION

In most of the major tissues and organs, the human body has limited regenerative capacity. Promising to repair damage following traumatic injury or disease, the field of regenerative medicine has been spurred by this fact. Small molecules, gene delivery, and stem cells are among the multiple therapeutic strategies that are being explored but primary approach to achieving regeneration remains tissue engineering (Feinberg et al., 2012). In order for the studies in the field of tissue engineering to progress into their clinical applications, some of the major challenges including (1) developing functional polymers, (2) exploring more sources of human cells, and (3) finding ways to keep the engineered construct viable in vitro and in vivo are still required to be addressed (Levenberg & Langer., 2004).

Injection of cells alone, development of encapsulated systems and transplantation of cells onto scaffolds are some of the main regenerative tissue engineering approaches. But, the latter approach, which permits experimental manipulation at three levels: the cells, the polymer scaffolds and the construction method, to achieve optimal construct, appears to be the dominant method used in research on tissue engineering (Yeong et al., 2004).

Shown in Figure 1 are various approaches in tissue engineering using cells, scaffolds, or their combination (Levenberg & Langer., 2004).

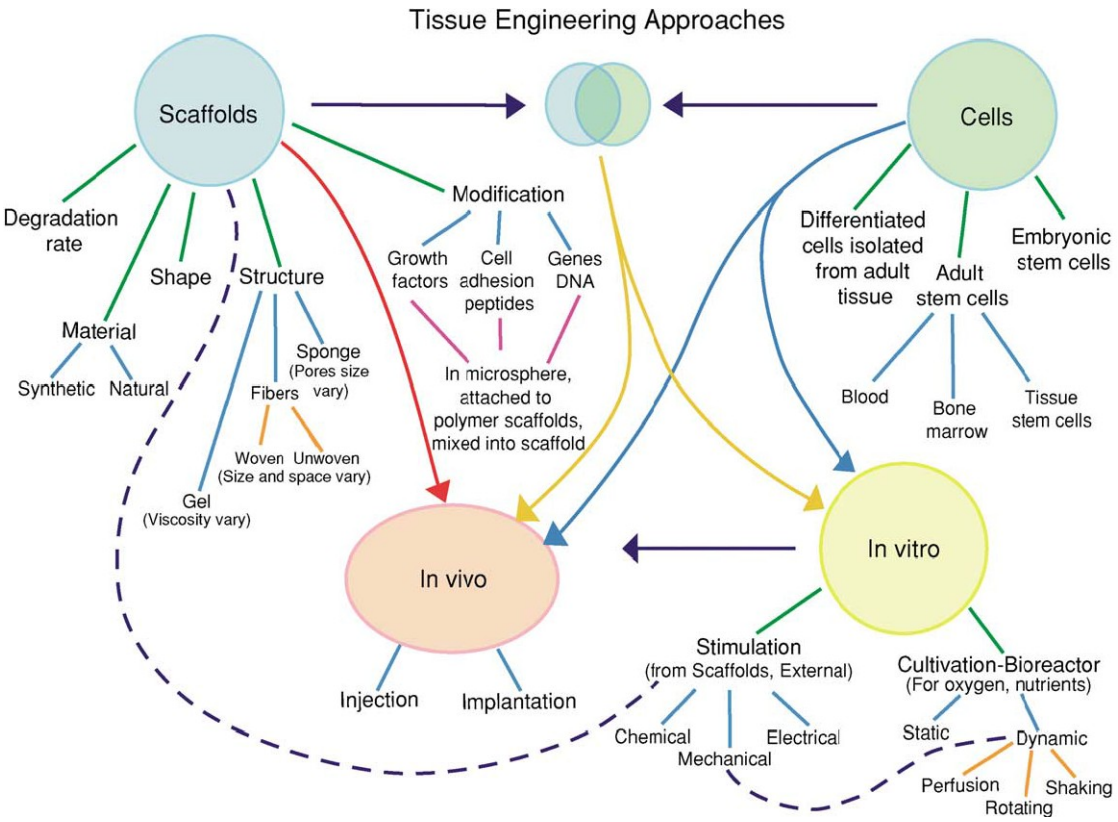

Figure 1: Various approaches in tissue engineering using cells, scaffolds, or their combination. Prior to surgical implantation or injection in vivo, the cells or engineered constructs can be cultivated and stimulated in vitro. In addition to different methods of cultivation or stimulation, various parameters affecting the scaffolds and various cell types used are shown (Levenberg & Langer., 2004)

1.2 NEURAL TISSUE ENGINEERING AND CURRENT CLINICAL APPROACHES

Peripheral nerve trauma complicates five per cent of all open wounds in the extremities due to sports and road accidents (Huang et al., 2006).As cited in the same paper, nerve is also disrupted by traction during complicated births, incidence of these lesions being 0.12% of all births .Spinal cord injury (SCI) is being sustained by approx. 10000 Americans every year. Damage to or disconnection of axons, loss of neurons and glia, and demyelination are the functional deficits following spinal cord injury. Not only the initial mechanical insult determine the SCI pathology but the secondary processes which include

ischemia, anoxia, free-radical formation, and excitotoxicity that occur over hours and days following injury, also determine the SCI pathology (Huang et al., 2006).

Treatment for peripheral nerve injury normally consists of the use of an autologous nerve graft or direct end-to end surgical reconnection of the damaged nerve ends. Small defects or gaps in the never can be repaired by Suturing the ends of the two nerve ends. However, this approach is not required for longer nerve gaps the reason being that any any tension introduced into the nerve cable would inhibit nerve regeneration. Therefore, an autologous nerve graft that is harvested from another site in the body is used to span the injury site for larger nerve defect (Schmidt & Leach., 2003). Disadvantages, associated with the use of autologous peripheral nerve grafts include the need for a second surgical procedure in order to harvest the tissue with the related problems of potential for infection, donor site morbidity as well as the development of neuropathic pain. Other limitations are potential mismatches in size and fasciculation patterns between the grafted nerve and proximal and distal nerve stumps to be bridged besides the amount of nerve that can be harvested (Deumens et al., 2010).

For their potential usefulness in the bridging of peripheral nerve lesions a number of non-autologous sources have also been explored as an alternative to autologous tissues. Therefore, both allogenic (same species) and even xenogenic (different species) tissues have been taken into consideration. Inspite of sufficient supply of such alternatives, a number of risk factors are associated with them like immunogenic mismatching besides the possible transmission of disease.

Integra Neurosciences Type I collagen tube (NeuraGen Nerve Guide) and SaluMedica's SaluBridge Nerve Cuff are some of the devices which are FDA approved for short nerve defects (Schmidt & Leach, 2003). NeuroMatrix™ or NeuroFlex™ from Collagen Matrix Inc., Neurotube from Synovis Micro Companies Alliance; and Neurolac from Polyganics BV are other FDA and/or CE approved nerve conduits (Table 1) (Deumens et al., 2010).

Table 1: FDA/CE approved nerve conduits (Deumens et al., 2010).

FDA/CE approved nerve conduit/graft	Company	Biodegradability	Conduit Length(cm)
SaluBridge™	SaluMedica	Non-biodegradable	6
Neurotube™	Synovis Micro Companies Alliance	Biodegradable	4
Neuromatrix™ or Neuroflex™	Collagen Matrix Inc.	Biodegradable	2.5
Neurolac™	Polyganics BV	Biodegradable	3
Neuragen™	Integra Neurosciences	Biodegradable	3

1.3 ELECTROSPUN SCAFFOLDS FOR NERVE REGENERATION

Referred to as the tissue engineering triad, cells, scaffolds and growth-stimulating signals are the key components of engineered tissues. The scaffold attempts to mimic the function of the natural extracellular matrix and the main role of the scaffolds are (i) to provide temporary mechanical support to the newly grown tissue by defining and maintaining a 3D structure (ii) to serve as an adhesion substrate for the cell, aiding with the localization and delivery of cells when they are implanted and (iii) to channel the development of new tissues with the appropriate function (Yeong et al., 2004).

A nonwoven mat derived from electrospun nanofibers typically exhibits a high porosity and large surface area due to the small feature size which result in enabling a a nanofiber-based scaffold to closely mimic the hierarchical structure of the extracellular matrix (ECM), an environment critical for signal transduction, cell attachment/ migration, and nutrient transport (Xie et al., 2009). Several studies have been done to study the cell morphology on nanofiber-based scaffolds. For example, Xie et al. (2009) reported that embryonic stem cells (ESCs) seeded on nanofibers could be induced to differentiate into neural lineages. In another study, Mao et al. (2009) studied the influence of the diameter of electrospun

fibers on the differentiation and proliferation of neural stem cells. Silk fibroin nanofiber-based scaffolds have also been of great interest for several cell studies. For instance, Li et al. (2006) reported that electrospun silk fibroin based scaffolds supported hMSC growth and differentiation toward osteogenic outcomes. Also, Hu et al. (2012) reported that regenerated electrospun silk fibroin nanofibers can promote Schwanncell adhesion, growth and proliferation, and have excellent biocompatibility.

1.4 IRON OXIDE NANOPARTICLES INCORPORATED SCAFFOLDS

According to Kim et al. (2011), in response to an external magnetic field, Iron oxide nanoparticles have magnetic properties that have attracted interests not only for in vivo tracking or imaging agents of neuronal cells but also for positioning cells. Not only due to their magnetic properties but also for their relative non toxicity, biodegradability, high surface area-to-volume ratio and biocompatibility, Iron oxide nanoparticles are of great interest. As cited by Ziv-Polat et al. (2012), for various biomedical applications, e.g., DNA separation, magnetic resonance imaging (MRI,) hyperthermia, diagnostics, cell labeling and sorting, and X-ray contrast agents, gene and delivering drugs to a target organ and/or tissue across the blood brain barrier (BBB) and magnetic stimuli sensitive polymeric systems, the use of iron oxide magnetic nanoparticles has already been demonstrated.

Since they are not toxic and can be metabolized by living organisms, Fe_3O_4 nanoparticles are of special interest for biomedical applications (Chicea et al., 2009). To produce magnetic scaffolds made of different materials, iron oxide nanoparticles have been incorporated in the recent studies in the field of tissue engineering . For example, Zhang et al. (2009) reported the fiber formation mechanism for both pure PAN and the Fe_3O_4 nanoparticles suspended in PAN solutions. Ziv-Polat et al. (2012) reported that magnetic fibrin hydrogel scaffolds prepared by the interaction of thrombin-conjugated iron oxide magnetic nanoparticles with fibrinogen increased the growth of nasal olfactory mucosa (NOM) cells.

Studies aimed at investigating the effects of iron oxide particles on stem cells have been listed in Table 2 (Markides et al., 2012)

The surfaces of these particles can be modified by creating of few atomic layers of organic polymer or inorganic metallic (e.g. gold) or oxide surfaces (e.g. silica or alumina), suitable for further functionalization by the attachment of various bioactive molecules. Nanoparticle coatings can be comprised of several materials such as inorganic or polymeric which further classifies to natural (Gelatin, dextran, chitosan etc.) and synthetic (PVP, PLGA, PEG, PVA etc.) (A.K. Gupta, M. Gupta., 2005).

Table 2: List of studies aimed at investigating the effects of iron oxide particles on stem cells and results (Markides et al., 2012)

Particle used	Biological polymer	Particle size	Cells type	Particle concentration	Toxicity assay	Result
Feridex (FDA approved)	Dextran	80–150 nm	rMSC & mMSC	25 μg/mL	Live/dead (7 days after labelling) differentiation assays	No loss of cell viability observed after 7 days with or without either TA
Ferric oxide (noncommercial)	Poly-L-lysine	15 nm	HUC	20 μg/mL	MTT (5 days continued culture) cellular apoptosis—annexin V/PI double stainassay	
Noncommercial	Silica	110 nm	hMSCs	200 μg/mL	MTT (1 hr and 24 hrs) Trypan Blue	No reduction in viability after 1 hour. No reduction in cell proliferation
Feridex	Dextran	80–150 nm	hMSC	100 μg/mL	FACS (fluorescence-activated cell sorting) to evaluate cell death—to determine if iron oxide incorporation affects surface markers expression	No reduction in viability after 12 hours
Iron fluorescent particle	Polystyrene	900 nm	pMSC		Trypan Blue MTT Morphological observations Differentiation studies	Cells maintained viability and retained label for up to 3 months. Differentiation capacity not altered
Manganese oxide nanoparticles	Mesoporous silica	65 nm	mMSCs		MTS	75% cell viability Limited cell differentiation in the osteogenic lineage
Commercially available		1630 nm	rMSCs	2.8 μg/mL	Trypan Blue	Did not affect cell viability
Feridex	Dextran	150 nm	ESCs	50 μg/mL	Trypan Blue	Did not affect cell viability
	HEDP		rMSC	25, 50, 100 μg/mL	MTS	Cell viability not affected at lower concentrations but viability decreased to 70% at 100 μg/mL
Feridex	uncoated	80–150	hMSC	50–250 μg/mL	Comet assay	Did not affect viability

1.5 SILK AS A BIOMATERIAL

For thousands of years for textile industry fibers from the Bombyx mori (domesticated) silk worm have been used. Silk gets its mechanical strength, softness, and elasticity from Silk fibroin, which is the interior structural protein of silk and which consists of the heavy and light chains and forming the filaments of the silk fiber. Sericin which is water-soluble protein glue, bonds the fibroin together to form the natural silk fiber. As stated by Hu et al. (2006), silk fibroin finds application in the fields of biomedical and biotechnological engineering e g. tissue regeneration, biosensors, cell adhesion and growth, drug release as well as the potential starting material for the preparation of medical devices.

Due to the dominance of hydrophobic domains consisting of short side chain amino acids in the primary sequence, silks are generally composted of β-sheet structures which permit tight packing of stacked sheets of hydrogen bonded anti-parallel chains of the protein (Vepari & Kaplan, 2007). Three structural models, termed silk I, II and III, have been reported to exist in silk fibroin. Silk I refers to the water-soluble structure existing within the silkworm gland before spinning, Silk II is the insoluble extended beta-sheet conformation which forms after the spinning of silk fibers from the spinneret of the silkworm and Silk III is an unstable structure observed at the water air interface (Valluzzi and Gido, 1997; Valluzzi et al., 1999).

As described by Wang et al. (2010), compared to other natural degradable materials, silk fibroin exhibits superior mechanical properties, variable degradation rates ranging from weeks to months in vivo due to control of crystallinity, exceptional biocompatibility with low inflammatory and immunogenic response, various processing windows, and all aqueous material processing options to form films, fibers, gels, sponges and microspheres

In vitro evaluation of electrospun silk fibroin scaffolds for vascular cell growth has been investigated by Zhang et al. (2009) in which and human coronary artery smooth muscle cell (HCASMC) and Human aortic

endothelial (HAEC) were cultured on electrospun silk fibroin scaffolds. Within 5 days after seeding, the observation of SEM and confocal images revealed that there was alignment and elongation of HCASMCs on random nonwoven nanofibrous silk. According to Yang et al. (2007), like many other biomaterials, Silk fibroin, is capable of inducing substantial axon regeneration and tissue repair of relatively small (1 cm) defects. Excellent axon growth and glial cell migration from DRG explants in vitro has been observed more recently through silk fibroin conduits containing GDNF and NGF, as well as topographical cues provided by aligned silk fibroin nanofibers, (Madduri et al., 2010). Based on the study of MSCs on porous silk scaffolds, Wang et al. (2011) has reported that after 3 weeks of cultivation, the spatial cell arrangement and the collagen type-II distribution in the MSCs-silk scaffold constructs resembled those in native articular cartilage tissue.

1.6 EFFECT OF MAGNETIC FIELD ON NERVE CELLS

In recent years, research studies, possibly inspired by nature, have focused on the relationship between magnetic fields and neuron activities (Chen et al., 2007). As mentioned by Johnsen & Lohmann. (2005), many animals, including birds, mole rats, molluscs and fishes can sense the Earth's magnetic field and use it as a signal for guiding movements over both long and short distances. Their study further mentioned that in several animals, that are known to orient to the Earth's magnetic field, such as honeybees, salmon, trout, sea turtles, the magnetic mineral, magnetite (Fe_3O_4), has been detected mostly in the form of single-domain crystals. Such crystals are minute (~50 nm diameter), permanently magnetized bar magnets that twist into alignment with the Earth's magnetic field if allowed to rotate freely.

The magnetite crystal, most likely needs to contact the nervous system in order to function as a magneto receptor in animals (Johnsen & Lohmann., 2005). Magnetite has been found in a region of the upper beak of the bobolink that is innervated by the ophthalmic nerve and also in trout's olfactory cells that is

innervated by the ros V nerve, which has units that also respond to magnetic stimuli (Johnsen & Lohmann., 2005). Although linkage between the magnetic crystals and the nervous system has been hypothesized for more than two decades, direct anatomic evidence has still not been established.

As cited by Chen et al. (2007), effects of both static and alternating magnetic fields on neuron activities such as firing frequency, pulse sequence, polarity and amplitude, have been confirmed and extensively investigated. Numerous hypotheses have been proposed but the underlying mechanism of neuron response to magnetic field is still unknown.

1.7 RESEARCH OBJECTIVE

The overall goal of the thesis was to investigate the effect of magnetite (Fe_3O_4) nanoparticles on the growth and proliferation of neuronal Schwann cells (ATCC). To achieve this goal, magnetic silk fibroin mats were prepared using electrospinning method by incorporating Fe_3O_4 nanoparticles and cell studies were performed on these mats using Schwann cells.

1.8 INTODUCTION TO EXPERIMENTS

The work in the thesis is divided into 3 separate but complimentary experiments.

1. Experiment 1 describes the initial set up, techniques and equipment used to fabricate the magnetic silk scaffolds along with the details of the parameters used.

2. Experiment 2 explains in detail different ways used to characterize the scaffolds. Various structural analysis and image analysis techniques were used and magnetic measurements were performed.

3. Experiment 3 describes the study of Schwann cells on magnetic silk scaffolds prepared in the initial part of the project. Growth and proliferation as observed over a period of 7 days and neurite outgrowth and release of neurotrophic factors was monitored.

CHAPTER 2-BACKGROUND

2.1 PHYSIOLOGY AND ANATOMY OF THE NERVOUS SYSTEM

The nervous system is composed of two parts, peripheral nervous system (PNS) and central nervous system (CNS) that vary in their function and physiology. The PNS consists of sensory neurons and motor neurons that detect stimulus from receptors and inform the CNS and run from the CNS to muscle and glands, also known as effectors, that take action respectively. The CNS consists of spinal cord and brain which is protected by bone-skull and vertebrate and is filled with fluid and tissue that helps in insulating the brain and spinal cord (Figure 2) (Huang & Huang., 2006).

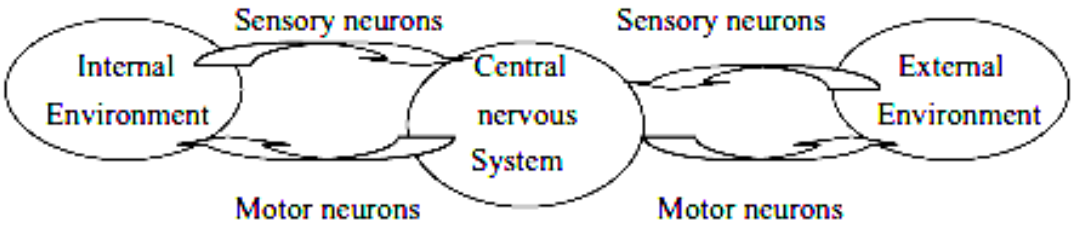

Figure 2: Cellular components of the nervous system (Huang & Huang., 2006)

The two cell types that the nervous system is mainly composed of are neurons and neuroglia. Neurons mainly consist of a cell body or soma and axon and dendrite extensions. Outside the spinal cord are located clusters of nerve soma ,also known as ganglia. Electrical signals are carried by dendrites to the neuron cell body and the impulses are conducted away through axon. Glial cells or neuroglia including Schwann cells in the PNS and oligodendrocytes in the CNS function as support cells and help in function of neurons. Neurons are less abundant than the glial cells and cannot undergo mitosis but can regenerate a severed portion or develop new processes under certain conditions. Unlike neurons, glial cells have some capacity to regenerate.

In the PNS, axons are surrounded by sheaths of Schwann cells (Figure 3) (Heath & Rutkowski., 1998). Neurilemma, a basement membrane similar to that found in epithelial layers forms the outer surface of the Schwann cell layer. As an alternative, in many axons, an insulating sheath formed by dense layers of successive wrapping of the cell membrane of Schwann cells surrounds the axon which function to increase the velocity of propagation of the nerve impulse, especially the axons that extend up to 1m. On the contrary, the continuous basement membrane and sheath of Schwann cells does not surround the axons (Schmidt & Leach., 2003).

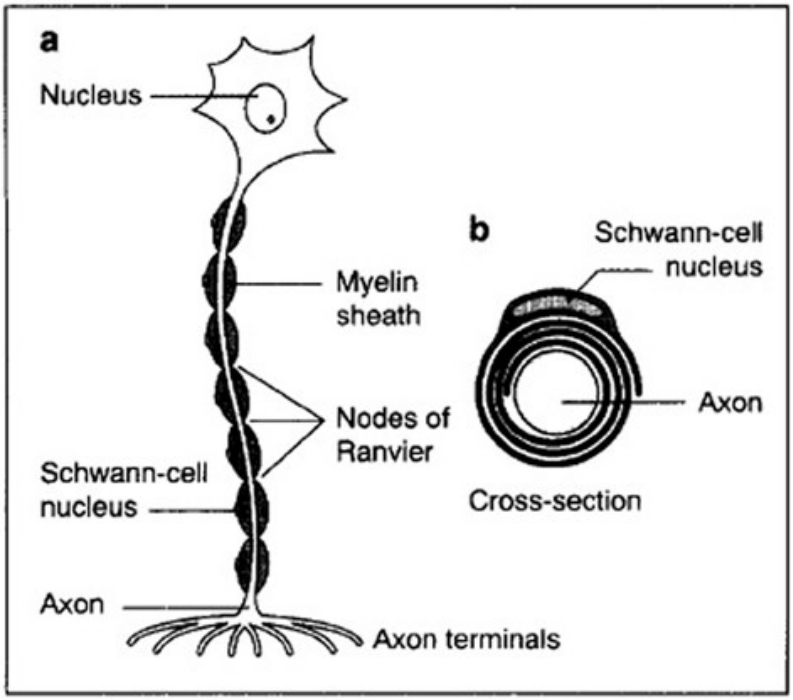

Figure 3: Peripheral motor neuron (Heath & Rutkowski., 1998)

ANATOMY OF THE PERIPHERAL NERVOUS SYSTEM

Motor and sensory axons bundles together by means of a support tissue form a peripheral nerve in the form of an anatomically defined trunk (Figure 4) (Siemionow & Brzezicki., 2009). The innermost layer, Endoneurium, comprising of oriented collagen fibers surrounds individual axons and their Schwann cells. Next, the layer surrounding groups of axons forms fascicles and is composed on many layers of flattened cells (fibroblasts) and collagen. The outermost layer, epineurium, binds individual nerve fascicles into a nerve trunk and comprises of loose fibrocollagenous tissue. The support tissue that bundles the axons together is well vascularized by capillaries or vessels that penetrate the nerve from surrounding arteries and veins (Schmidt & Leach., 2003).

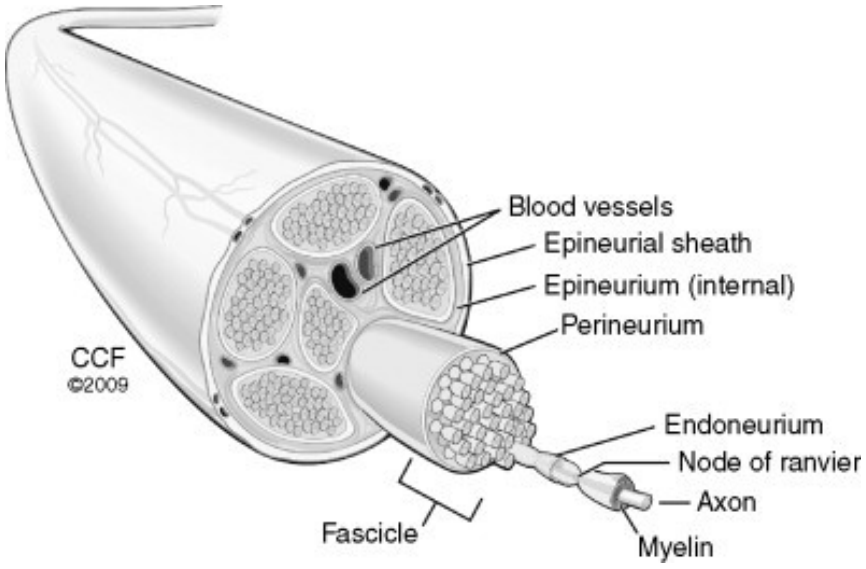

Figure 4: Anatomical overview of the PNS. Figure was adapated from Siemionow & Brzezicki., 2009.

2.2 NERVE INJURY AND REGENERATION

The extent of the injury forms the basis of classification of human nerve injuries. The first clinical classification scheme (Seddon, 1943) was based on 3 types of nerve fiber injury and subsequent sparing or loss of nerve continuity. Neurapraxia is referred to the injuries caused by nerve compression with or without demyelination, axonotmesis are the injuries caused by axon transection with both perineurium and epineurium remaining intact and neurotmesis is referred to as the nerve transection where the continuity of the epineurium is interrupted. Recovery of these injuries basically depends on remyelination (Figure 5) (Bahr & Bonhoeffer, 1994), axon regeneration without surgical reunion through the original endoneurial pathways and via surgical reunion of proximal and distal nerve stumps to support regeneration into the disrupted endoneurial tubes (Wood et al., 2011).

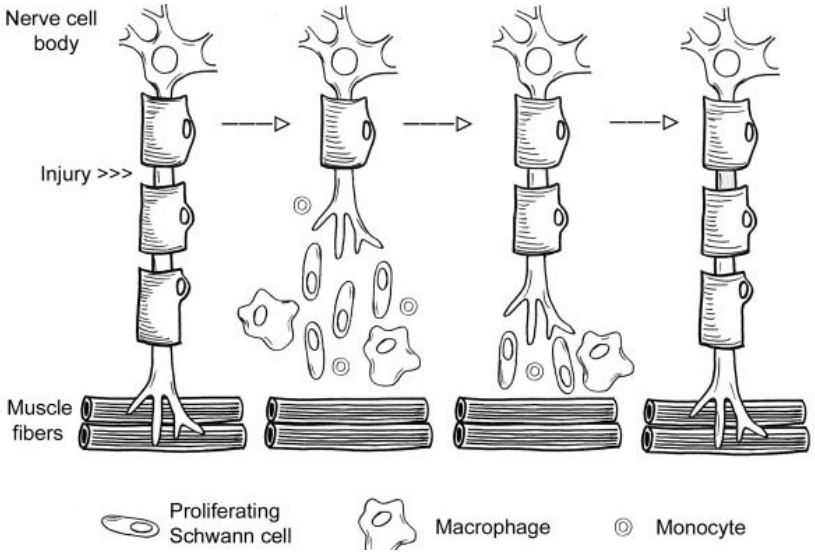

Figure 5: Responses to axotomy in the PNS. Figure adapted from Bahr & Bonhoeffer, 1994.

As described by Wood et al. (2011), Sunderland's system of classification expands upon that of Seddon by dividing nerve injuries into five different degrees of injury severity as opposed to three (Sunderland, 1978) (Figure 6).Neurapraxia and axonotmesis of Sunderland's classification are similar to the first and

second degree of Seddon's classification.The third and fourth degree injury occur due to disruption in endoneurium (while perineurium and epineurium remain intact) and all the neural and internal supporting elements (epineurium remains intact), respectively. Neurotmesis is classified as Sunderland's fifth degree injury and is similar to the third degree of injury according to Seddon's where complete transaction of nerve occurs.treatment and surgical intervention are necessary for recover after the fifth degree injury (Wood et al., 2011).

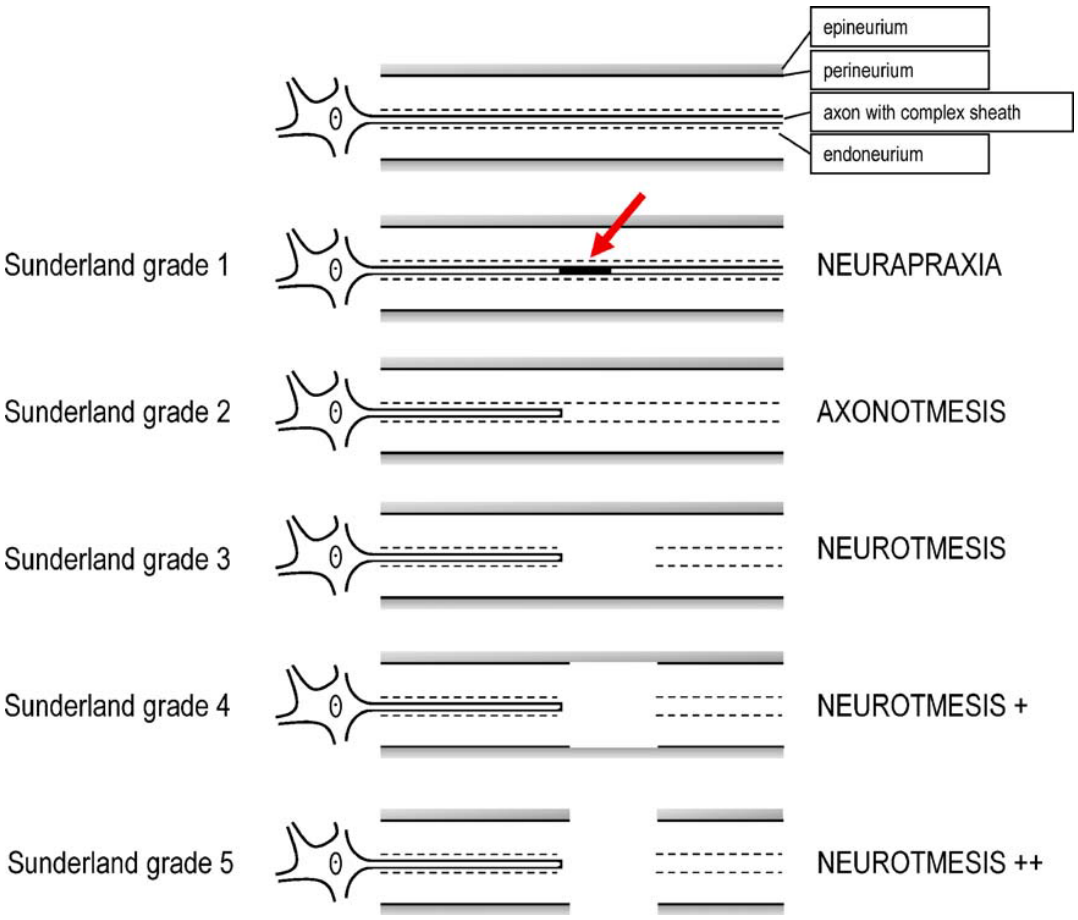

Figure 6: Schematic representation of the five degrees of nerve injury according to Sunderland (Sunderland, 1951).Figure adapted from Deumens et al., 2010.

A major difference between PNS and CNS lies in the fact that peripheral nerves can regenerate whereas CNS axons cannot ,in their native environment (Schmidt & Leach., 2003). In CNS, cellular debris, myelin, oligodendrocytes, microglia and astrocytes form an impermeable glial scar and block the regenerating neuron from reaching the synaptic target (Figure 7) (Bahr & Bonhoeffer., 1994). Implantation of nerve grafts to support axon extension or supplying nerve growth factors to the site of injury are the two important strategies that are used to promote axonal extension (Schmidt & Leach., 2003).

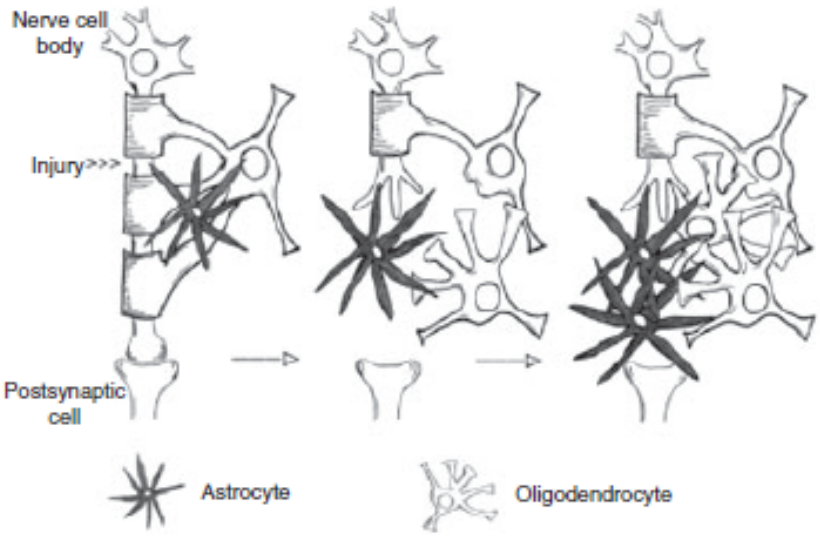

Figure7: Response to axotomy in CNS. Figure adapted from Bahr & Bonhoeffer., 1994.

To bridge the gaps between nerve stumps, nerve grafts are essential and have been a topic of wide experimentation and research due to the limited supply of autografts. Enormous efforts, in the last few decades, have been focused on understanding the requirements for successful peripheral axon regeneration at molecular and cellular level (Deumens et al., 2010) and as a result, therapeutic strategies have made it possible to treat most severe types of PNI. Glycosaminoglycans and ECM proteins have also been modified to function as scaffolds for various in-vivo and clinical studies (Huang & Huang et al., 2006). Some clinically evaluated materials used as an aid for successful nerve regeneration have been

shown in Table 3 (Nectow et al., 2011).Some materials such as silk, collagen etc. have also been used for in-vivo applications (Table 4) (Nectow et al.,2011).

Table 3: Some clinically evaluated materials (Nectow et al., 2011)

Materials	*Fabrication methods*	*Nerve*	*Defect size (in mm)*	*Outcomes*
Autologous tissues				
Muscle	Vein filled with muscle grafts	Varied	5–60	85% of patients with "good" recovery or better[a]
Nerve	Autologous graft	Varied	Varied	Gold standard
Vein	Autologous graft	Nonessential sensory	≤30	Good results; all patients considered surgery "helpful"
	Autologous graft	Sensory	10–30	91% of patients with "good" recovery or better[a]
Biopolymers				
Type I collagen (NeuraGen)	Collagen conduit	Digital	10–20	88% of patients with "good" recovery or better[a]
Synthetic materials				
PGA (Neurotube)	PGA conduit	Digital	Up to >8	>74% of patients with "good" recovery or better[a]
	PGA conduit	Digital	≤40	>89% of patients with "good" recovery or better[a]
PLCL (Neurolac)	PLCL conduit	Hand nerves	≤20	Sensory outcomes not significantly different from autograft

Table 4: Some materials evaluated In-Vivo (Nectow et al., 2011)

Materials	*Fabrication methods*	*Animal, nerve*	*Defect size (in mm)*
Biopolymers			
Agarose	Polysulfone conduit, agarose hydrogel with LN-1/NGF gradient	Rat, sciatic	20
Chitosan	Chitosan conduit with internally aligned PGA filaments	Dog, sciatic	30
Collagen	NeuraGen conduits	Human, brachial plexus	≤20
	Collagen conduit with longitudinal collagen filaments	Dog, peroneal	30
Fibrin	Silicone conduit with GDNF released from fibrin matrix	Rat, sciatic	13
Gelatin	Genipin-crosslinked gelatin conduit	Rat, sciatic	10
Keratin	Silicone conduit with keratin hydrogel	Mouse, tibial	4
Silk	Silk fibroin conduit with longitudinal silk fibers	Rat, sciatic	10
	Silk fibroin conduit	Rat, sciatic	8
Synthetic materials			
PCL	PCL conduit with GDNF microspheres	Rat, sciatic	15
Poly(hydroxybutyrate)	PHB conduit, alginate hydrogel with glial growth factor	Rabbit, common peroneal	20, 40
Poly(D,L-lactide)	Porous conduit with surface microgrooves	Rat, sciatic	10
PLGA	PLGA/Pluronic F127 conduit	Rat, sciatic	10
Polyurethane	Polyurethane-collagen conduit	Rat, peroneal	7

2.3 ROLE OF SCHWANN CELLS IN PERIPHERAL NERVE REGENERATION

Although various experiments support the theory that Schwann cells enhance nerve migration by releasing various bioactive factors and offering highly preferred substrate for axon, the underlying mechanism behind the dynamic axon/Schwann cell relationship is still unknown (Evans et al., 2000). Numerous cell adhesion molecules such as L1, Ncadherin, gamma1 integrins and neural cell adhesion molecules are secreted by Schwann cells along with structural and adhesive ECM molecules such as laminin and collagen. Other functions of Schwann cells include synthesizing and secreting various neurotrophic factors to enhance nerve regeneration, forming a sheath around axon to serve as a guide and aid in its growth, clearing out debris to create favorable environment for nerve growth and most importantly, myelinate axons (Bunge et al., 1994).

In the normal nerve, Schwann cells appear to be quiescent, having heterochromatin-rich nuclei and relatively electron dense cytoplasm. However, upon nerve injury the Schwann cells in the distal nerve undergo extensive change associated with axonal degeneration. Schwann cells proliferate and form columns reaching their peak of proliferation by days 2–4. They serve as scaffolds for regenerating axons by expressing adhesion molecules on the surface plasma membrane and produce various tropic factors for regenerating axons (Evans et al., 2000).

Various experiments have shown that Schwann cells, along with acellular matrices can stimulate axons to elongate faster to the distance needed .Schwann cells play a major role in leading peripheral axons to the distal nerve stump and in synapse formation. The ability of Schwann cells to promote nerve regeneration has been a research area of intense focus (Huang & Huang et al., 2006).

Some of the recent studies focused on delivering Schwann cells to the site of injury have been summarized in Table 5 (Pfister et al., 2011).

Table 5: Engineered Nerve Conduits Tested in Animal and Human Models with SC (Pfister et al., 2011).

Natural Degradable Conduits

Conduit Material	Luminal Matrix	Cells	GF	Model
Chitin		SC, BMSC		Rat sciatic
Collagen	Collagen or empty	SC		Rat sciatic
Collagen (Kevlar reinforced)	Saline or empty	SC		Rat sciatic

Synthetic Degradable Conduits

Outer Conduit Material	Luminal Matrix	Cells	GF	Model
Poly-3-hydroxybutyrate (PHB)	Alginate, fibronectin hydrogel	SC	rhLIF	Rat sciatic
Poly-3-hydroxybutyrate (PHB)	Fibrin gel	SC, dMSC		Rat sciatic
Poly-D/L-lactic acid (PDLLA)			bFGF	Rat sciatic
	Micropatterned lumen	SC		Rat sciatic
Polylactic acid (PLA) or Silicone	Collagen gel	SC		Rat sciatic
	PLLA fibers, Matrigel			Rat sciatic
Polylactic-co-glycolic acid (PLGA)	Rat tail glue, laminin	SC		Rat sciatic
Polylactic-co-golycolic acid (PLGA)	Collagen gel	EMSC		Rat sciatic
Polylactic-co-glycolic acid (PLGA, foam)	PLGA channels, laminin	SC		Rat sciatic
Trimethylenecarbonate-ε-caprolactone (TMC/CL)	Fibrin gel, Matrigel	SC		Rat median

Table 5(contd.)

Synthetic Nondegradable Conduit				
Outer Conduit Material	Luminal Matrix	Cells	GF	Model
Polyacylonitrile / polyvinyl-chloride (PAN/PVC)	Matrigel	SC		Rat sciatic
Silicone	Aligned collagen fibrils	Fibro-blasts, SC		Rat sciatic
Silicone	Blood plasma	SC		Rat sciatic
Silicone	Gelatin	BMSC		Rat sciatic

Apart from these studies, Xu et al. (1995) has shown that Schwann cells, when implanted with Matrigel, can aid axonal regeneration across spinal cord transections in adult rats at levels above that of Matrigel alone. Kierstead et al. (2005) extended these studies to show that Schwann cell transplantation in combination with demyelination enhanced axonal growth in rat spinal cord injuries. Another study by Guest et al. (1997) supports the extension of these studies to human therapies: grafts of human Schwann cells in the injured nude rat spinal cord were found to create a highly integrated cord-graft interface and allowed a small population of neurons to regenerate across the graft and re-enter the spinal cord.

2.4 SILK SCAFFOLDS AND SCHWANN CELLS

Unique and favorable physiochemical and biological properties of naturally derived biomaterial silk fibroin have led to its various applications in the fabrication of scaffolds in the field of tissue engineering (Altman et al., 2003).

Inspite of being explored for various fields of tissue engineering, electrospun silk fibroin scaffolds have not been studied broadly for nerve tissue engineering (Zhang et al., 2009).

Xu et al. (2011) and Hu et al. (2012) reported that the electrospun SF mats supported the survival and growth of the Schwann cells cultured onto the mats, and the mat extract showed no significant cytotoxic effects on the proliferation of the Schwann cells. In another study by Yang et al. (2007) it was shown that silk fibroin supports the cell growth of DRG and facilitates the survival of Schwann cells without exerting any significant cytotoxic effects on the cell phenotype or cell functions.

Recently, Huang et al. (2012) reported that p75 immunoreactive Schwann cells were found throughout partially degummed 10 mm Spidrex® silk fibroin conduits in abundance and were associated with regenerating axons and that there was an apparent one-to-one relationship between N52 immunoreactive axons and p75 immunoreactive Schwann cells. Schwann cells have also been shown to grow and proliferate on PLGA-Silk Fibroin-Collagen 50:25:25 biocomposite scaffolds without any cytotoxicity (Wang et al., 2010)

2.5 RESPONSE TO SCHWANN CELLS TO IRON OXIDE NANOPARTICLES

Various fields of biosciences, biotechnology, medicine, environmental technology etc. have exploited applications of many biocompatible materials exhibiting variety of response to external magnetic field. Magnetic properties of such composite materials arise due to the presence of iron oxides nanoparticles or microparticles. These materials can not only be used as contrast agents for magnetic resonance imaging but also to generate heat during magnetic field exposure(Hyperthermia), to separate difficult to handle samples and to target drug or various other factor to a desired place (Šafařík et al., 2011).

Magnetic field controllable materials comprise of micro and nanoparticles, magneto rheological fluids, ferrofluids, films, nanowires and nanotubes, biological structures modified magnetically etc (Šafařík et al., 2011). The most common magnetically responsive materials include iron oxide(ferrites or magnetitie)

nano or microparticles that are dispersed in an inorganic matrix or a polymer (Safarik and Safarikova 2009).

Magnetic particles have found numerous applications such as (Šafařík et al., 2011):

1) Selective separation of biological materials with diamagnetic properties: Magnetically responsive materials can be separated from other materials in a complex sample with the help of external magnetic field.
2) Delivering and targeting the particles: Various magnetic materials coated with drugs can be guided to a desired location with the help of an external magnetic field and kept there until required.
3) Modification of biological materials: Diamagnetic biological materials such as cells can be magnetically modified using magnetic particles or magnetically labeled of biologically active compounds such as antibodies or enzymes.

In the field of neural tissue engineering, Kim et al. (2011) reported that Iron oxide nanoparticles synergistically promoted the neurite outgrowth in the presence of the nerve growth factor. Iron oxide nanoparticles prolonged the neurite length in dose dependent manner and a neural specific marker protein was upregulated by the iron oxide nanoparticles. On the contrary, Pisanic II et al. (2007) had results showing that exposure to increasing concentrations of anionic MNPs (magnetic nano-particles) results in a dose dependant decreasing viability and capacity of PC12 cells to extend neurites in response to their known biological cue, i.e. nerve growth factor. Dunning et al. (2004) used dextran coated superparamagnetic iron oxide particles to label Schwann cells and OECs (Olfactory ensheathing cells) that were transplanted into focal areas of demyelination in adult rat spinal cord, to visualize the cells using magnetic resonance imaging (MRI).It was also specified that SPIO-labeled SCs and OECs were able to myelinate normally after transplantation into focal areas of demyelination.

Surprisingly, not a lot of studies have been done to understand the behavior of Schwann cells towards magnetic particles and the influence of magnetic stimulation on their growth and proliferation.

2.6 ELECTROSPINNING

ELECTROSPINNING OVERVIEW AND EVOLUTION

Electrospinning employs electrostatic force to stretch and accelerate a charged polymer solution jet and is known to produce submicron diameter fibers. Because of the ease with which a wide range of polymers can be electrospun to produce nanoscale fibers, this technique has found tremendous growth and attention commercially and in the research field (Gevelber et al., 2010)

Briefly, in this process, a syringe pump controls the polymer liquid flow rate and delivers the liquid to a small diameter nozzle as shown in (Figure 8) (Gevelber et al., 2010). A high-voltage power supply generates an electric field between the nozzle and a grounded collector placed at a distance away from the nozzle. As an outcome of electric forces, the drop of solution on the tip of the nozzle forms a conical projection, called a Taylor cone .When the applied electric field strength overcomes the surface tension, a straight jet is ejected from the tip of Taylor cone. This jet remains straight for some distance and then it bends and follows a looping and spiraling path. Meanwhile, solvent is evaporated as the jet flies to the collector. Ultimately, the jet solidifies and deposits on the grounded collector forming a nonwoven fiber mat (Gevelber et al., 2010).

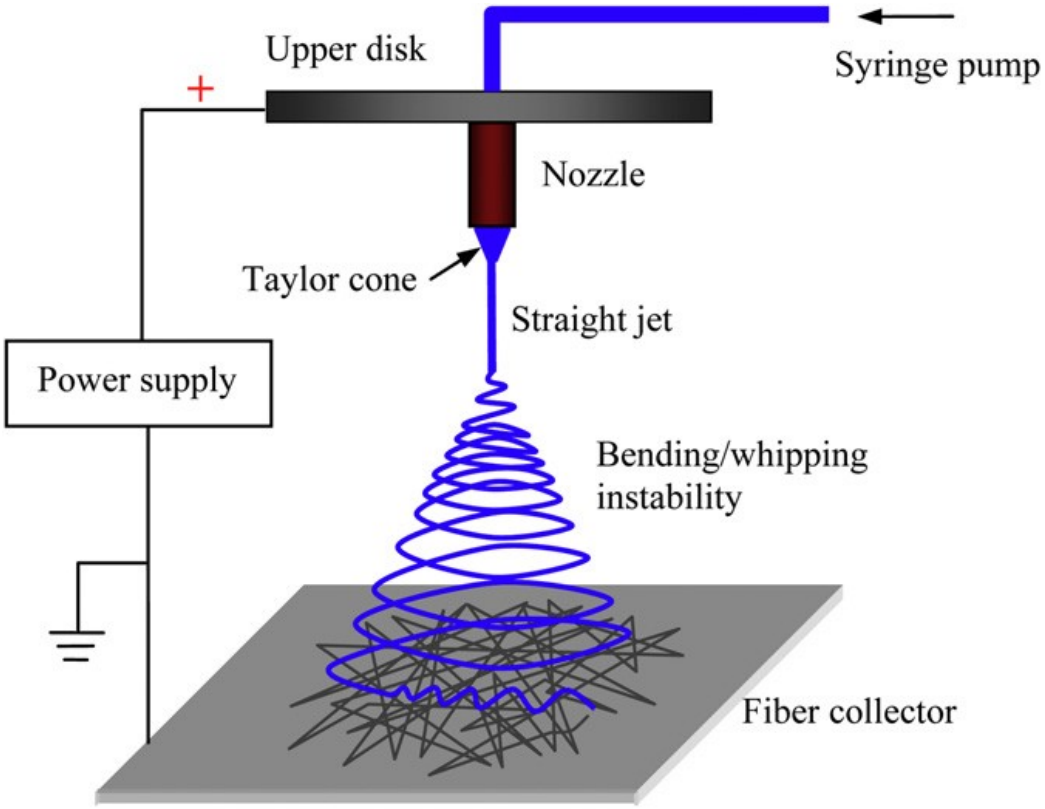

Figure 8: Schematic of Electrospinning setup (Gevelber et al., 2010).

The process of electrospinning, previously known as 'electrostatic spinning', was first inspected by Zeleny in 1914, and was found to be a practical technique for spinning small-diameter polymer fibers. Formhals was issued the first US patent, in 1934 after all the technical difficulties related to fiber formation were overcome, for the process and setup used to spin synthetic fibers (Zhang et al., 2009).

Since electrospinning allowed fabrication of fibers at nanoscale, it became popular in the early 1990s because of the emerging field of nanotechnology. To date, more than 50 different polymers have been successfully electrospun into ultrafine fibers (Zhang et al., 2009).

Summary of a few polymers which have been successfully electrospun into super fine fibers is listed in Table 6 (Huang et al., 2003).

Table 6: Polymers that have been spun in solution form (Huang et al., 2003).

No.	Polymer	Solvent	Concentration	Prospective
1	Nylon6,6,PA-6,6	Formic acid	10 wt.%	Protective clothing
2	Polyurethanes, PU	Dimethyl formamide Dimethyl formamide	10 wt.% 10 wt%	Protective clothing Electret filter
3	Polybenzimidazole, PBI	Dimethyl acetamide	10wt.%	Protective clothing nanofiberreinforced composites
4	Polycarbonate, PC	Dimethylformamide:tetrahydrofuran(1:1) Dichlormethane Dimethylformamide:tetrahydrofuran(1:1) Dimethylformamide:tetrahydrofuran(1:1)	10 wt.% 15 wt.% 14-15 wt.% 20 wt.%	Protective clothing Sensor, filter Electret filter
5	Polyacrylonitrile, PAN	Dimethyl formamide Dimethyl formamide Dimethyl formamide Dimethyl formamide	600 mgPAN/10-5M3 Dimethylformamide 15 wt.%	 Carbon nanofiber
6	Polyvinyl alcohol, PVA	Distilled water Distilled water	8-16 wt.% 4-10 wt.% 1-10 wt.%	
7	Polylactic acid, PLA	Dimethyl formamide Methylene chloride and Dimethyl formamide Dichloromethane Dichloromethane	 5 wt.%	Membrane for prevention of surfery induced-adhesion

3 main factors that considerably affect the process of electrospinning of different polymers are:

(i) Rheological properties of the solution such as elasticity, viscosity, surface tension etc., chemistry of the solution as well as the molecular weight of the solution.

(ii) Process related parameters, such as voltage, distance of the collector from the tip, flow rate etc.

(iii) Temperature, humidity and other environment related parameters

Most favorable combination of these electrospinning parameters should be generated to prepare nanoscale fibers with absence of beads.

2.7 RESEARCH AIM

The first aim of this thesis was to determine the different concentrations at which Iron oxide nanoparticles could be electrospun with Silk/PEO and different parameters suitable for electrospinning to have a bead-free magnetic mat. The second aim was to analyze the mats using different characterization techniques to figure out the most suitable mat for cell studies. The third aim was to analyze the growth and proliferation of Schwann cells on electrospun magnetic silk mats.

CHAPTER 3: MATERIALS AND METHODS

3.1 EXPERIMENT 1: FABRICATION OF MAGNETIC SILK SCAFFOLDS

3.1.1 SILK FIBROIN SOLUTION

Silk fibroin (SF) solution was prepared following a previously established processing procedure (Li et al., 2006; Schneider et al., 2009; Rockwood *et al.*, 2011; Figure 9). Cocoons of *Bombyx mori* silkworm (Tajima Shoji Co., LTD., Yokohama, Japan) were boiled for 30 min in an aqueous solution of 0.02M Na2CO3 to extract the glue-like sericin proteins. The degummed silk was rinsed thoroughly with distilled water and allowed to dry overnight. The dried silk fibroin was then dissolved in 9.3M LiBr solution at 60^{o}C for 4 h. Dissolved silk was dialyzed in distilled water using a Slide-a-Lyzer dialysis cassette (Pierce, MWCO 3,500) for 48 h and centrifuged to remove any particulate. It resulted in 5-7% (w/v) silk fibroin solution.

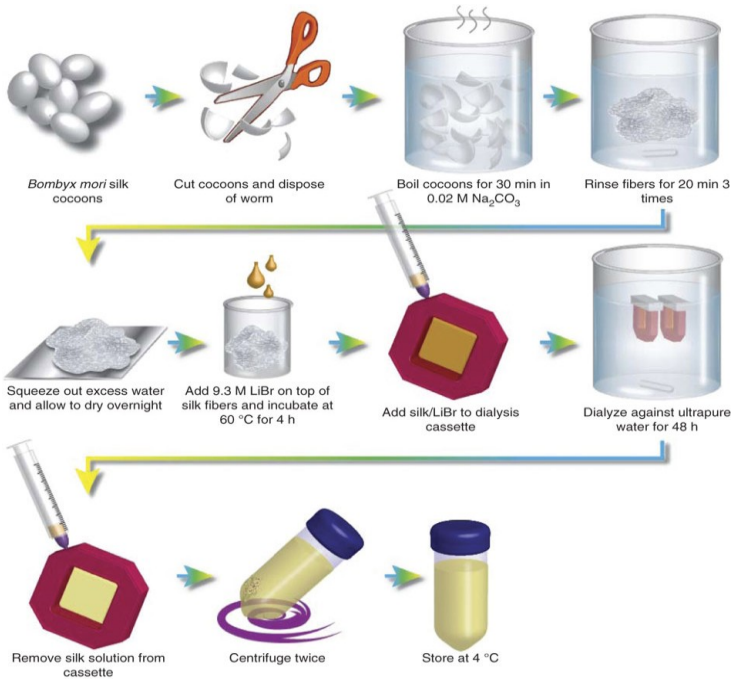

Figure 9: Schematic of the silk fibroin extraction procedure. Going from the raw material (cocoons) to the final aqueous-based solution takes 4 days. (Rockwood et al., 2011)

3.1.2 PREPARATION OF SILK-Fe_3O_4 BLEND SOLUTION

To prepare the electrospinning solution, 7 % silk fibroin solution was mixed with 5 wt. % PEO (900,000 g/mol). The addition of PEO to silk solutions generated a viscosity and surface tension suitable for electrospinning (Jin et al., 2002). PEO solution of 5wt. % was prepared by directly adding the PEO to deionized water. Homogeneous solutions were obtained by stirring for at least 5 days at room temperature (Li et al., 2006).

To make the mats magnetic, Iron (II, III) oxide (Fe_3O_4) nanopowder, with less than 50 nm particle size, stabilized with PVP coating (Sigma Aldrich) was added to the silk fibroin solution.

To start the experiments, five parts silk fibroin solution was blended with two parts PEO resulting in 7ml of final solution.Fe_3O_4 nanopowder was mixed with DI water to form 10% (v/v) Fe_3O_4 solutions which was then added to 7ml of SF/PEO solution in variable amounts.

These experiments were performed at different flow rates and voltages to be able to make the scaffolds magnetic and also to obtain a mat without any bead formation in the mat.

For final experiments, four parts silk fibroin solution was blended with one part 5% PEO. The Silk: PEO solution was kept as 4^oC prior to electrospinning.Fe_3O_4 nanopowder was added directly into 5 ml of Silk/PEO blend solution in different concentrations. Six groups of scaffolds were prepared. Blend concentrations of 0.0 wt. %, 1.0 wt. %, 3.0 wt. %, 5.0wt. %, 7.0wt. % and 10.0 wt. % for Fe_3O_4 were chosen (Table 7) .Addition of Fe_3O_4 nanopowder was followed by manual stirring to allow dispersion and prevent aggregation (Figure 10)

Table 7: Different concentrations of Fe_3O_4 nanopowder and silk

Samples	Ratio of Silk (7%): PEO (5%)	Amount of solution used (ml)	Total Silk in the solution (gms)	Amount of Fe_3O_4 (% by weight)	Total Iron oxide(Fe_3O_4) in the solution (gms)	Ratio of weight of silk: weight of iron oxide
Group I	4:1	5	0.28	0%	0	--------
Group II	4:1	5	0.28	1%	0.05	5.6::1
Group III	4:1	5	0.28	3%	0.15	1.8::1
Group IV	4:1	5	0.28	5%	0.25	1.12::1
Group V	4:1	5	0.28	7%	0.35	0.8::1
Group VI	4:1	5	0.28	10%	0.50	0.56::1

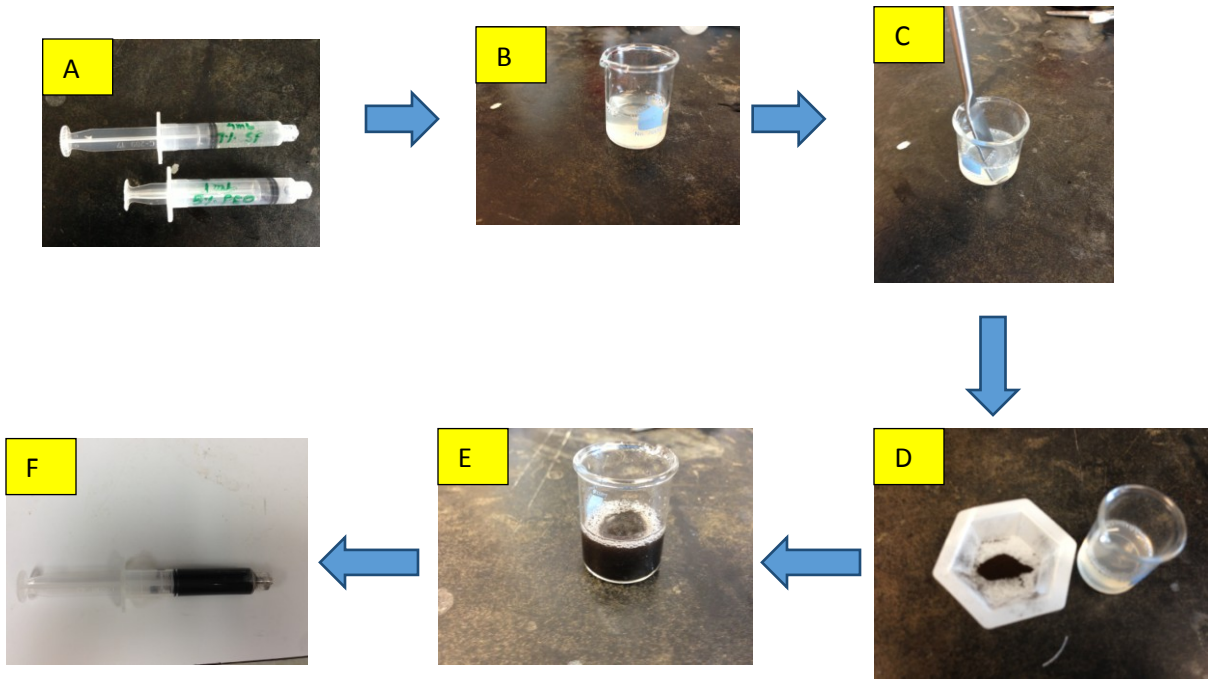

Figure 10: Protocol for preparing the SF/PEO/Fe_3O_4 nanopowder solution. A) 4 ml of Silk fibroin solution (7%) and B) 1 ml of PEO (5%) are added together to form a blend solution, C) and manually stirred. D) Required concentration of Fe_3O_4 is added to the blend solution and stirred to homogenously disperse the particles, E). F) The solution is then collected in a syringe to electrospin.

3.1.3 ELECTROSPINNING SET UP

The pre-existing set up includes a chamber composed of plexi-glass in which the electrospinning procedure takes place. The chamber contains a shelf supported by a scissor lift that controls the needle to target spacing. An 18 gauge needle is mounted within an aluminum counter electrode disk and is connected to the syringe pump. The counter electrode helps to shape the electric field and propel the silk solution downward toward the target. An Orion Sage M362 syringe pump (Thermo Electron Corporation) sits on top of the chamber that controls the flow rate of the electrospinning solution and an ES30P-5W high voltage power supply (Gamma High Voltage Research, Inc.) is outside of the chamber that provides voltage to the needle between 10 KV to 30 KV (Figure 11 A).

Modifying the collector shape and size directly influences the properties of the resulting material (Yarin *et al*., 2001). Initially random fibers were collected using a stationary circular aluminum collector and aligned fibers were collected using a rotating mandrel collector configuration (Kenawy et al., 2009, Figure 12). Due to certain difficulties in using the above mentioned collectors, the most suitable collector chosen for final experiments was the rotating plate collector. A flat cardboard of dimensions 19cm* 10cm was used instead of the metallic plate and was taped to the rotating support at the bottom. The rotational speed was set at 16 rpm. The entire surface was then covered with non- stick aluminum foil to collect the fibers and was grounded to the power supply using 18 gauge wire (Figure 11 B).

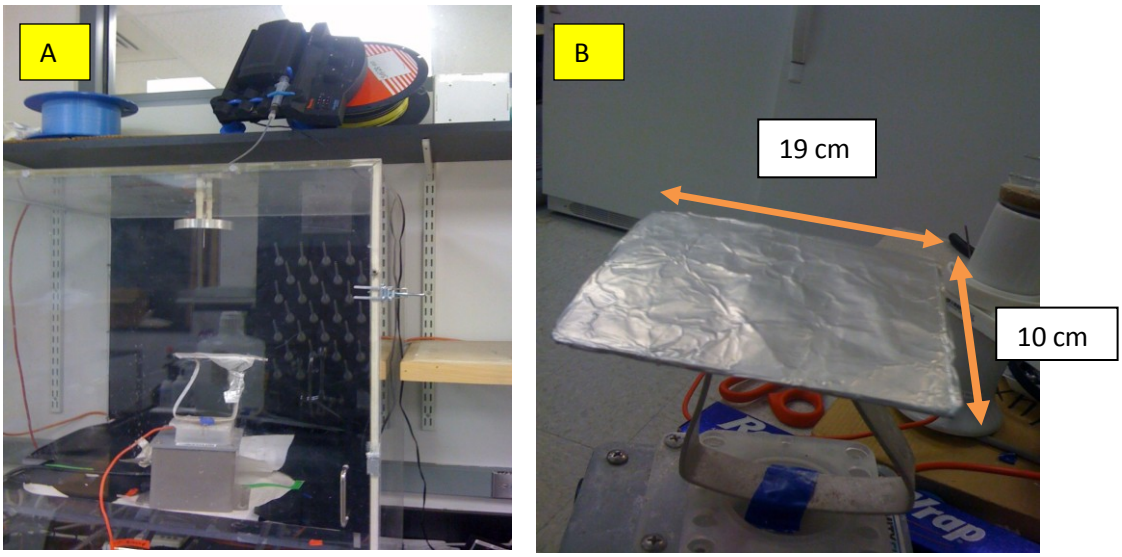

Figure 11: (A) Pre-existing electrospinning set up (B) Flat rotating cardboard collector covered with non-stick aluminum foil rotating at 16rpm

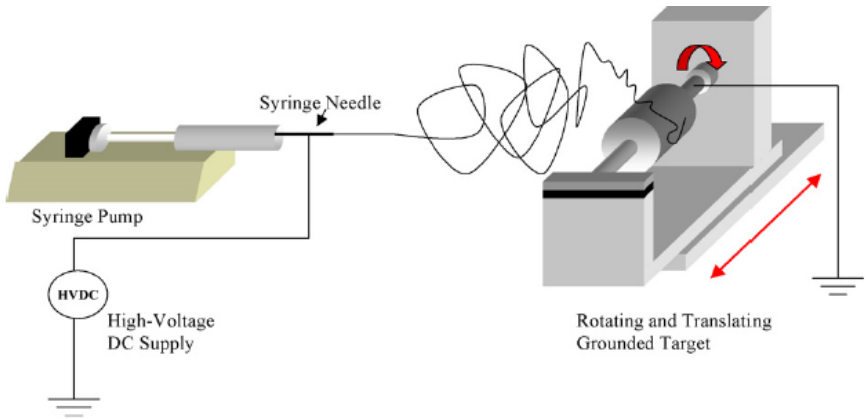

Figure 12: Schematic of rotating mandrel electrospinning configuration (Kenawy et al., 2009)

3.1.4 SELECTION OF ELECTROSPINNING PARAMETERS

SF/PEO and SF/PEO/Fe_3O_4 nanocomposite fibers were prepared using the electrospinning method. Tip to target distance was held 19 cm and the polymer solution was 7 wt. % for all the experiments. Flow rate was maintained at 0.03 ml/ min. Experimental voltage effect analysis was performed for the SF and SF/PEO/Fe_3O_4 electrospinning solution using an output voltage range between 15 kV and 25 kV (Table8).

The only two parameters that were changed during the experiment were voltage and Fe_3O_4 nanopowder concentration in the solution. For every output voltage value, 6 electrospun mats were prepared using different concentrations of Fe_3O_4 nanopowder, that is, 0 wt. %, 1 wt. %, 3 wt. %,5 wt. %, 7 wt. % and 10 wt. %. Briefly, at 15 KV, 1 electrospun scaffolds was prepared in each group, listed above, which resulted in 6 electrospun scaffolds at a particular voltage. Similarly, 6 electrospun scaffolds were prepared at 20 KV and 6 electrospun scaffolds at 25 KV.

Table 8: List of parameters used for Electrospinning

Total amount of SF/PEO solution used (ml)	5
Concentration of Fe_3O_4 nanopowder used (wt %)	0, 1, 3, 5, 7, 10
Spacing between the tip of the needle and the collector (cm)	19
Flow rate (ml/min)	0.03
Voltages used (KV)	15, 20, 25
Total electrospun scaffolds prepared at each voltage	6
Total electrospun scaffolds prepared	18

3.1.5 WATER ANNEALING AND WATER LEACHING

The electrospun scaffolds were water annealed by placing them on a shelf in a valved container partially filled with water. Next, a 24 mmHg vacuum was pulled within the container, and once vacuum was reached the valve was placed in the closed position. This produces a saturated water vapor environment that induces β-sheet secondary structure formation within the silk film (Lawrence et al., 2010). The films were left within the water vapor environment for an 8 hour period. The scaffolds were then water

leached using DI for 48 hours. The scaffolds were submerged in 4 liters of DI water separately and water was changed after every 12 hours. Water leaching helped to remove 5% PEO from the fibers.

3.2 EXPERIMENT 2: CHARACTERIZATION OF THE SCAFFOLDS

3.2.1 IMAGING TECHNIQUES

3.2.1.1 LIGHT MICROSCOPE

To confirm the presence of the iron oxide particles in the mats, particles were characterized visually by light microscopy (Rudge et al., 2010).Samples characterized were: SF/PEO mats, SF/PEO/1 wt. % Fe_3O_4, SF/PEO/3 wt. % Fe_3O_4, SF/PEO/5 wt. % Fe_3O_4, SF/PEO/7 wt. % Fe_3O_4 and SF/PEO/10 wt. % Fe_3O_4 prepared at 20 KV. 2 images were taken for each sample at 2 different areas on the sample. Magnification was 20 X for all the images. Size range of the aggregates was compared between different samples by measuring the diameter of 5 random aggregates in each image for each sample using Image J software.

3.2.1.2 SCANNING ELECTRON MICROSCOPY

After the process of leaching, electrospun scaffolds were allowed to dry. A small section of the sample was cut from the scaffold from a random position and then mounted on aluminum stubs using copper or carbon tape and sputter coated with Pt/Pd for 60 seconds. The samples were imaged using scanning electron microscopy (SEM) with a Zeiss SUPRA 55VP FESEM (Harvard University). The samples were mounted in the SEM using a 9 pin stub holder mount so that the surface morphology could be easily assessed. An accelerating voltage of 5 kV was applied to the samples and Everhart-Thornley side or an Inlens side secondary electron detector was used for imaging. Samples electrospun at different voltages and different concentration of Fe_3O_4 were analyzed.

After comparing the morphology of the mats using the SEM images of the mats electrospun at 15 KV, 20 KV and 25 KV, mats electrospun at 20 KV were chosen for further characterization and cell studies.

3.2.1.3 TRANSMISSION ELECTRON MICROSCOPY

Samples were collected for transmission electron microscopy (TEM) during electrospinning to observe the location of Fe_3O_4 in the electrospun mats. Fibers were electrospun directly onto 300 mesh copper Formvar/carbon coated grids for 10 s. The fibers were then imaged using a Zeiss Libra 120 Energy Filtered Transmission Electron Microscope (Harvard University). An accelerating voltage of 120 kV was used during imaging and the Omega filter was utilized for some of the samples. Samples electrospun at 20 KV with different concentrations of Fe_3O_4 were analyzed.

3.2.2 IMAGE ANALYSIS

3.2.2.1 FIBER DIAMETER DISTRIBUTION

To analyze fiber thickness and fiber distribution of different samples, Image J software was used. With approximately 5 fibers in each image, the number of fibers analyzed for diameter analysis was typically on the order 90 from 6 images. Each fiber was measured about 3 times along its length and then an average was calculated for it to ensure measurement precision. Scale bar was 2 μm and magnification was 20 kX.

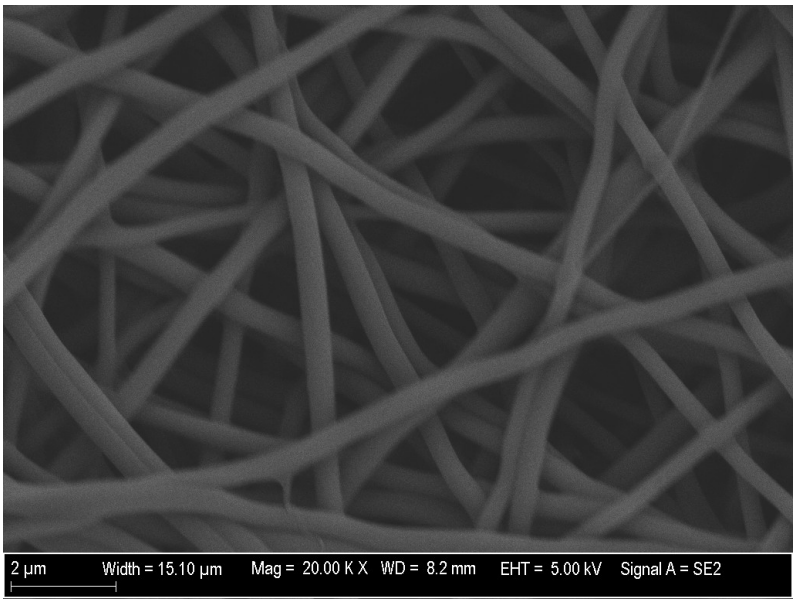

Figure 13: SEM image of the fibers electrospun at 20 KV. Scale bar is 2 µm.

3.2.2.2 MESH CHARACTERIZATION-VOID AREA FRACTION ANALYSIS

3 SEM images taken by a Zeiss SUPRA 55VP FESEM (Harvard University) using the SE2 side of the detector at magnification 10 kX from each group of electrospun mats were analyzed using Image J software. The groups analyzed were: SF/PEO mats, SF/PEO/1 wt. % Fe_3O_4, SF/PEO/3 wt. % Fe_3O_4, SF/PEO/5 wt. % Fe_3O_4, SF/PEO/7 wt. % Fe_3O_4 and SF/PEO/10 wt. % Fe_3O_4.

The threshold of each image was set to exclude void space as demonstrated in Figure 14. The ratio of excluded pixels to total pixels per image was used to estimate void area fraction of the entire mat (Jose et al., 2012).

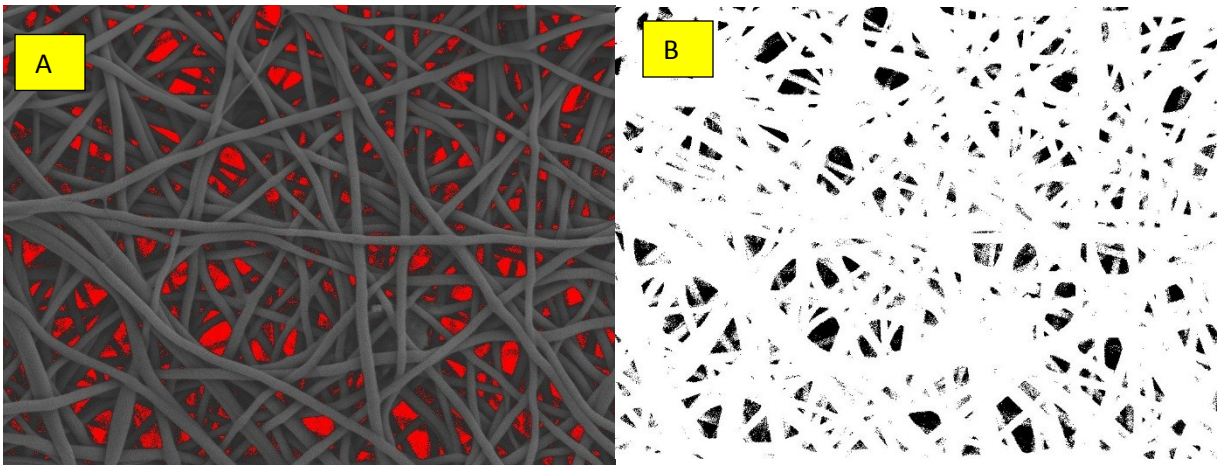

Figure 14: Demonstration of Image J processing to calculate porosity. (A) Threshold set to exclude void space (Red). (B) Processing completed revealing void area fraction (black). (Jose et al., 2012).

3.2.3 STRUCTURAL ANALYSIS

3.2.3.1 XRD ANALYSIS

The crystal structure of the SF/PEO fibers and SF/PEO/Fe_3O_4 fibers were investigated by powder X-ray diffraction. The powder X-ray diffraction analysis of the samples electrospun at 20 KV and the received Fe_3O_4 powder was carried out using Philips PW1830 Diffractometer with optically encoded goniometer PW 3020 operating with a Cu-Kα radiation source(λ =0.1542 nm) operating in the reflection mode. The electrospun mats were loaded on the aluminum holders (Figure 15). XRD scans were recorded from 5˚ to 80˚ for 2θ with a 0.02 step-width and counting time for each step of 2 sec/step.

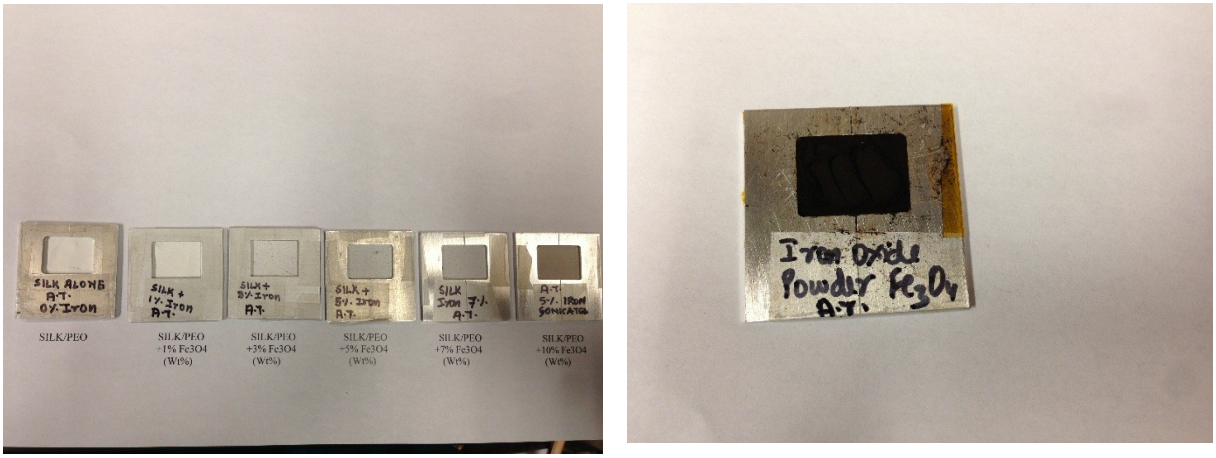

Figure 15: Samples prepared for X- ray diffractometer on aluminum holders.

3.2.3.2 FTIR ANALYSIS

FTIR spectra were obtained to estimate the secondary structure of the SF/PEO and SF/PEO/Fe_3O_4 fibers prepared by electrospinning. For each sample, a measurement of 32 scans was collected at a resolution of 4 cm^{-1}, which were acquired over a wavenumber range of 600-4000 cm^{-1}. Quantification of silk secondary structure was based on analyzing the amide I region (1,600–1,700 cm-1). The amide I region was selected from the entire spectrum and a linear baseline was applied to the spectrum (Lawrence et al., 2008)

Fourier self-deconvolution was used to determine β-sheet content in silk electrospun mats prepared at 20 KV as explained in detail by Hu *et al.* (2006). The average percent composition of fibroin secondary structure for the electrospun mats specifically the amount of β-sheet structure, was assessed by integrating the area of each deconvoluted curve and then normalizing to the total area of the amide I region of the fitted spectra(Lawrence et al., 2008).

3.2.3.3 THERMAL GRAVIMETRIC ANALYSIS (TGA)

To analyze the exact concentration of Fe_3O_4 in the scaffolds and to study the degradation rate of the samples, TG was performed on a TA Instruments Q500 thermo-gravimetric analyzer at a heating rate of 2 °C min^{-1} from room temperature to 300 °C in a nitrogen purge gas flow of 50.0 mL min^{-1}. To prevent the

powdered Fe_3O_4 sample from being blown out of the pan by nitrogen gas flow, the samples were encapsulated in aluminum DSC pans during heating. Several holes were made on DSC lids to let the sample surface be exposed to the atmosphere, to allow the degradation products escape. Silk scaffolds were cut into small pieces and placed directly on the TGA basket. Before each run, the empty pan with platinum TGA basket was used to calibrate the zero point of the total mass. The initial sample mass ranged between 6.0 and 10.0 mg.

3.2.4 MECHANICAL TESTING

Mechanical testing was performed on an Instron model 3366 universal testing machine (Instron, Norwood, MA) to compare the mechanical properties of SF electrospun mat and Fe_3O_4 embedded mats. All the samples were fully hydrated for 2 hours in DI water before performing the test and were immersed in PBS bath during the experiment. The dimensions of all the samples were kept the same, 15 mm (length) * 10 mm (Width).Thickness varied for all the samples. Blue Hill software was used to set pre-configured test method to Tension and samples were being pulled at the rate of 5 mm per minute until failure.

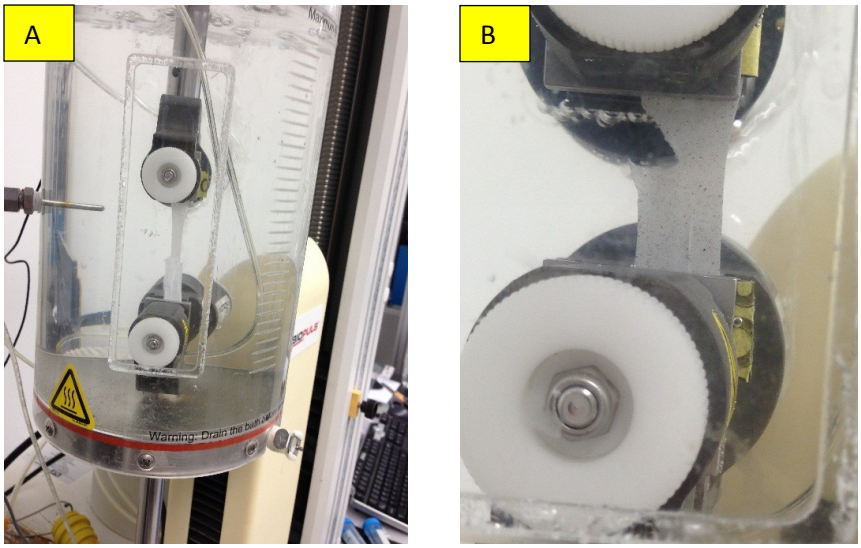

Figure 16: (A) Fully hydrated sample between the clamps immersed in PBS bath being pulled at the rate of 5 mm per minute. (B) Close view of the sample nearing failure of the test.

3.2.5 MAGNETIC MEASUREMENTS

Saturation magnetization and Magnetic coercivity measurements were made on electrospun mats prepared at 20 KV using a Quantum Design (MPMSXL) SQUID magnetometer at Northeastern University. 42 data points were recorded at 300 Kelvin between 10,000 Oe to -2000 Oe. The dimensions of all the samples were kept constant at 1cm (length)* 1cm (width) and the samples were weighed individually before the experiment on a weighing scale.

The coercivity (Hc, Oe) is the external applied magnetic field necessary to return the material to a zero magnetization condition and saturation magnetization is the point where there is no effect on the material's magnetization with the increase of magnetic field strength (Ms) (Figure 17).

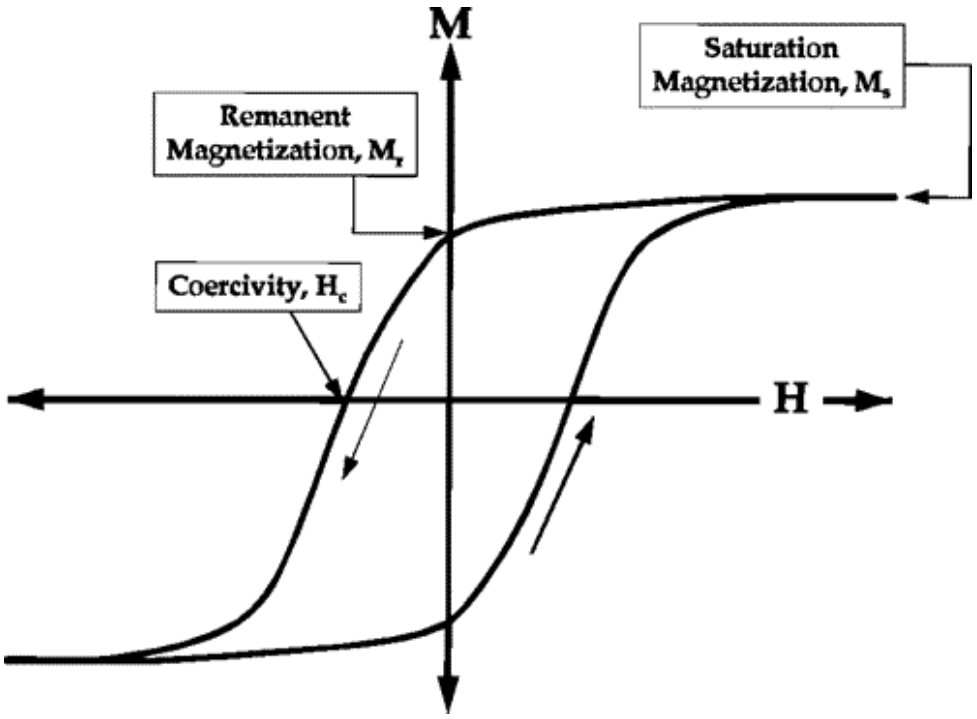

Figure 17: Important parameters obtained from a magnetic hysteresis loop. The saturation magnetization, Ms, remanent magnetization, Mr, and coercivity, Hc, are shown (Chem. Mater., 1996)

3.3 EXPERIMENT 3- SCHWANN CELL CULTURE

3.3.1 CELL CULTURE

Neuronal Schwann cells (ATCC, Manassas, VA), originating from ENU (N-ethyl-N-nitrosourea) induced rat peripheral neurotumor, RT4 were used for all the experiments. The cells were expanded in T175 tissue culture flasks. Briefly, frozen cells were thawed and resuspended in ATCC formulated Dulbecco's Modified Eagle's Medium (DMEM). The cell suspension was centrifuged for 10 minutes at a speed of 1200 rpm at 4˚C. After centrifugation, the pellet of cells obtained on the bottom of the centrifuge tube was resuspended in complete media consisting of 10% Fetal Bovine Serum (Sigma Aldrich) and 1% Anti-Anti (Sigma Aldrich).The cells were seeded onto flasks at a density of 5700 cells/cm2. Media was renewed every 2 to 3 days. Schwann cells were passaged at 70-80% confluency and all experiments used Schwann cell passage numbers between P1-P4.

For passaging the cells, Trypsin-EDTA (0.25%) (Invitrogen, NY) was used to detach the cells for the tissue culture flasks. The cell solution was then diluted in complete medium to inactivate the trypsin. A hemocytometer slide was used to estimate number of trypsinized cells and subcultivation ratio of 1:10 was maintained.

3.3.2 SURFACE PREPARATION AND SC SEEDING ONTO MAGNETIC SILK SCAFFOLDS

The SF/PEO and SF/PEO/Fe_3O_4 electrsospun mats prepared at 20 KV were used for in-vitro cell studies. All the mats were wetted prior to being cut to fit into a 24 well plate. A biopsy punch of 13mm diameter was used to cut all the mats and 6 samples were prepared in each condition. The samples were then placed in sterile 24 well plates. To ensure sterilization of the mats, 1 ml of 70% ethanol was added to each well and was exposed overnight to ultraviolet (UV) light in a laminar flow hood.

After surface preparation, Schwann cells were plated at a density of 25,000 cells per well in 3 wells from each group. The other 3 wells from the same group were used as controls and no cells were added in

those wells.1 mL of the complete media was added to each well including cells or without cells (controls). Complete media was renewed every 2 days to ensure growth and survival of the cells. Spent media was carefully pipetted out.

3.3.3 CELL VIABILITY ASSAY: ALAMAR BLUE®

To track cell viability and proliferation, alamar Blue®(Invitrogen, NY) assay was used. The alamar Blue ® assay was performed on Day 1, Day 3, Day 5 and Day 7 of the first week. A solution containing complete media and alamar Blue® in the ratio 10:1 was prepared and 1mL of the solution was added to each well. After 2 hours of incubation the plate was read using a spectrophotometer plate reader (SpectraMax M2e UV-Vis) in the fluorescence mode. The cells were excited at 530nm and the emission was measured at 590nm. alamar blue® was fully reduced by the method of autoclaving and was also read on the spectrophotometer plate reader, to make a comparison between the sample fluorescence values and alamar Blue's fully reduced value.

3.3.4 SCANNING ELECTRON MICROSCOPY

Prior to alamar Blue® testing, in order to look at the growth of the cells on the electrospun mats, samples of SC loaded mats were fixed with 4% Paraformaldehyde in PBS for 20 minutes and washed 2 times in PBS. The mats were then dehydrated by using increasing concentration of ethanol, that is, 60% ethanol, 70% ethanol, 80% ethanol, 90% ethanol and 100% ethanol for 10 mins each. The mats were then allowed to dry in the hood for a few minutes. After dehydration, the mats were mounted on aluminum stubs using copper tape and sputter coated with Pt/Pd. The samples were then loaded into Zeiss SUPRA 55VP FESEM (Harvard University) using a 9 stub holder and viewed under an accelerating voltage of 5 kV.

3.3.5 ENZYME-LINKED IMMUNO SORBENT ASSAY (ELISA)

After 4 days of culture, the culture medium was collected and scaffolds were suspended in HFIP for analysis of Nerve Growth (NGF). The analysis was done using the DuoSet ELISA development Kit (R&D Systems, MN). The assay was performed following the manufacturer's instructions. Briefly, a 96-well microplate was coated with capture antibody (goat anti-rat β-NGF) and incubated overnight at room temperature. The plate was then washed 3 times with the wash buffer (0.05% Tween®20 in PBS) and incubated for 1 hour with Reagent Diluent (1% BSA in PBS).Samples and standards were then added to the plate and incubated for 2 hours. Following incubation, Streptavidin conjugated to HRP was added to the plate and incubated for 20 minutes. Substrate solution (1:1, H_2O_2: Tetramethylbenzidine) was added following incubation and the reaction was stopped using a Stop solution (2N H_2SO_4).

Absorbance was measured at 450 nm and 540 nm in a microplate reader (SpectraMax M2e UV-Vis). Standard curve was generated using known amount of growth factors. The standard curves for nerve growth factor provided linear plot of absorbance versus concentration. The linear plot was used to determine the concentration of nerve growth factor. All the experiments were performed in duplicates.

To analyze the NGF content in the electrospun silk fibroin scaffolds, the mats were suspended in 250 µl of HFIP in lo-bind Eppendorf tube, which helped in releasing the growth factors. The tube was closed and incubated overnight as described in Wang et al. (2010). HFIP was then evaporated by flowing air through the tube and dried protein was resuspended in 1ml PBS. 100 µl sample prepared using this method was then added to the plate as mentioned above.

3.3.6 STATISTICAL ANALYSIS

All results are expressed as the mean ± the standard deviation. For comparing 6 groups, Analysis of variance (ANOVA) was used with Tukey's Multiple Comparison Post-test to compare the relative and adjusted values of different groups for 4 different time-points. Significant levels were set at $p < 0.05$.

CHAPTER 4- RESULTS AND DISCUSSION

4.1 ELECTROSPINNING

As noted earlier, 5 ml of SF/PEO (4:1) solution and different concentrations of Fe_3O_4 powder was used for electrospinning the mats at various voltages using 3 different collectors.

The collectors used to collect the fibers were:

1) Stationary circular aluminum collector
2) Rotating mandrel collector
3) Flat surface rotating collector

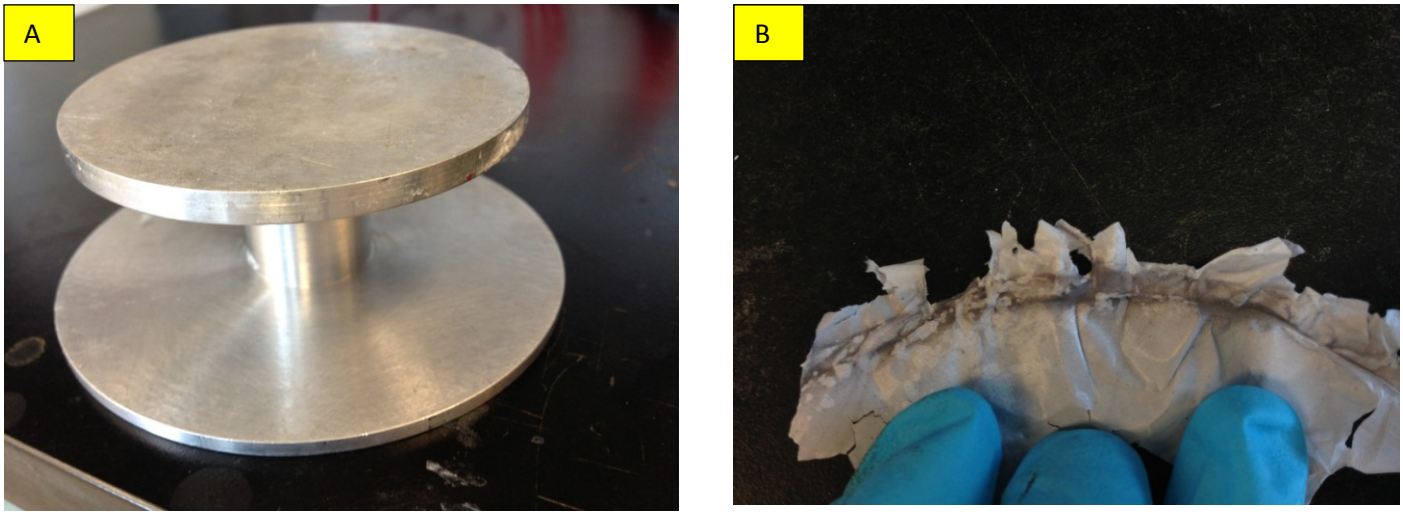

Figure 18: A) Stationary circular collector used initially for spinning scaffolds. B) For the samples prepared using this collector, uneven distribution of Fe_3O_4 was noticed.

Figure 18 show the electrospun mat prepared using the stationary circular Aluminum collector. These mats appeared greyer on the outside circumference as compared to the center region of the mat, which was due to the accumulation of the iron oxide particles or aggregates. It not only resulted in uneven thickness of the mat at the outer circumference but also uneven distribution of the iron oxide particles within the mat.

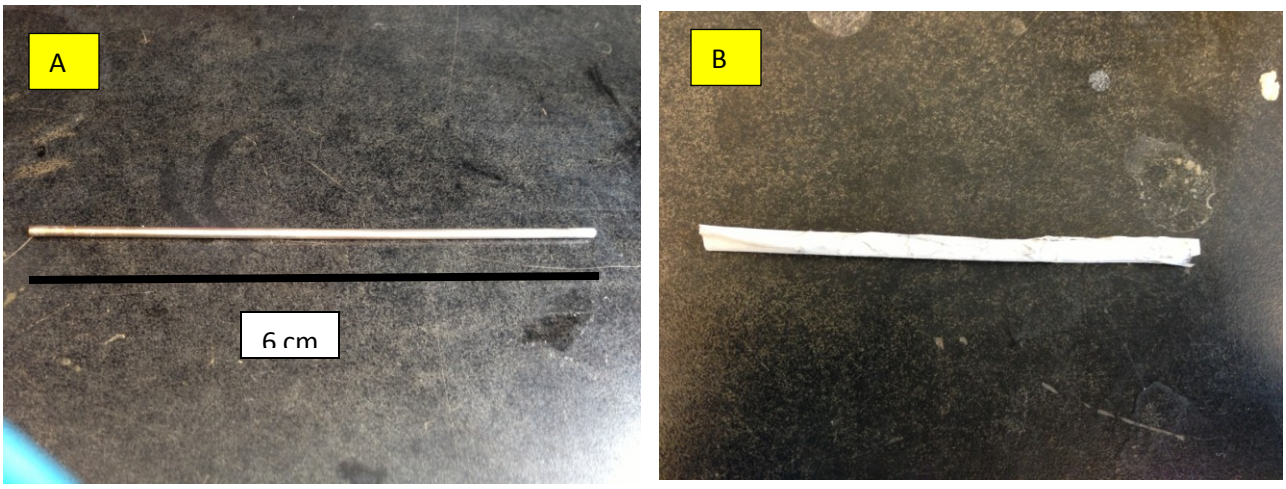

Figure 19: A) Thin rotating mandrel used for electrospinning the mats at different concentrations of Fe_3O_4.B) The sample prepared using thin rotating mandrel that had uneven surface ad uneven distribution of Fe_3O_4.

Figure 19 shows the electrospun mat prepared using the rotating mandrel collector. This collector was used to collect aligned fibers but due to high rotation speed, the mats had uneven surface with the appearance of spikes in certain regions. The fibers alignment started to go astray after a few minutes of electrospinning. The loss of alignment and uneven surface characteristics were attributed to the accumulation of charge on the fibers deposited. As more fibers were being collected on the mandrel, accumulation of charges may have caused the incoming fibers to be repelled resulting in less oriented fibers.

The samples that were prepared using the flat surface rotating collector had uniform thickness and the appearance of the gray/black color throughout the mat gave the impression of iron oxide nanoparticles being equally distributed over the entire region of the mat. As a result, flat surface rotating collector was chosen to prepare all the samples at different voltages and different concentrations of Iron oxide (Fe_3O_4).

To introduce the magnetic properties to the electrospun SF/PEO mats, Fe_3O_4 nanopowder was added to the SF/PEO solution in different amounts as described earlier. For lower concentration of Fe_3O_4 nanopowder (1 wt. %, 3 wt. %, and 5 wt. %), the particles were uniformly suspended in the solution before and during electrospinning. But with increase in the concentration of Fe_3O_4 nanopowder (7 wt. and 10 wt. %) , more aggregate formation was noticed in the solution. Nanoparticles aggregate forming clusters of colloids with an isotropic shape, most probably due to van der Waals attractions and weak magnetic attractions.

Manual stirring lead to homogenous dispersion of Fe_3O_4 particles throughout the solution. During electrospinning, due to the high density of the Fe_3O_4 particles, the particles tend to settle down at the bottom of the syringe in small negligible amounts. To overcome that problem, the syringe pump was placed vertically on top of the electrospinning chamber to allow the flow of the nanoparticles towards the syringe.

The mats electrospun at higher concentrations of Fe_3O_4 nanopowder than 10 wt. %, did not seem to be thick and stable enough as compared to the other mats.

It is well known that in traditional electrospinning process the applied voltage is one of the most important parameters that can influence the formation of ultrafine and nano fibers (Liu et al., 2010). To investigate the effect of applied external voltage on the morphology of the SF/PEO/Fe_3O_4 nanopowder mats and fiber diameter distribution and to prepare a bead-free mat, mats were electrospun at 3 different voltages of 15KV, 20 KV and 25 KV and images taken using SEM were analyzed (Figure 20, Figure 21, Figure 22 respectively).

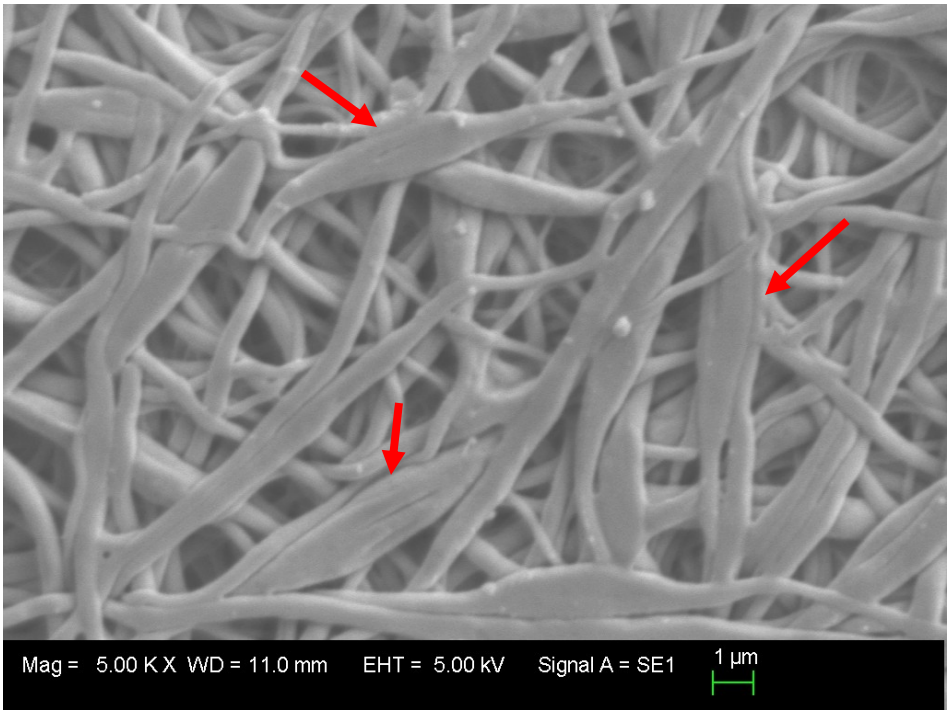

Figure 20: SEM image of the SF/PEO mat electrospun at 15 KV and with 3 wt. % Fe_3O_4 nanopowder. The fibers have spindle shaped beads in it (red arrows) and are not continuous

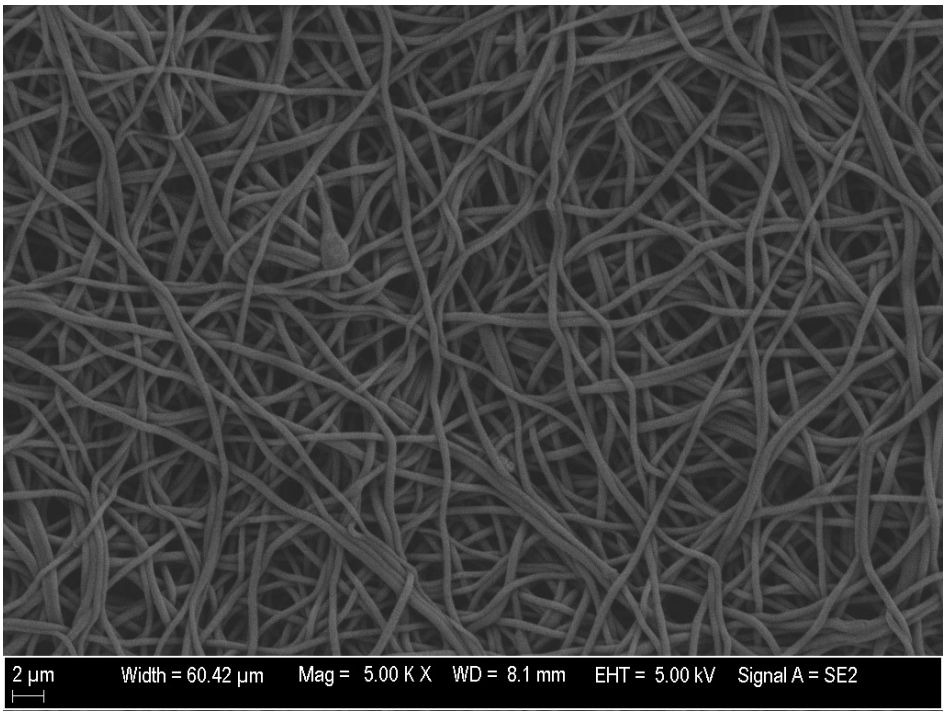

Figure 21: SEM image of SF/PEO mat electrospun at 20 KV with 3 wt. % Fe_3O_4 nanopowder. The mat has continuous fibers and no beads are present.

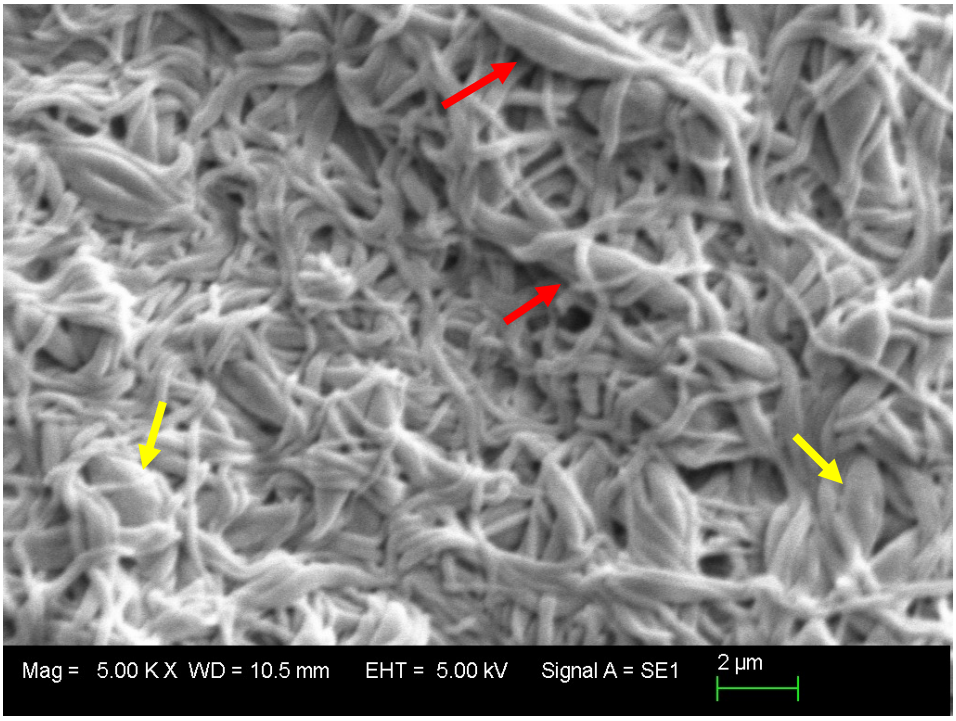

Figure 22: SEM image of SF/PEO mat electrospun at 25 KV with 3 wt. % Fe_3O_4 powder. The mat has spindle shaped (red arrows) and circular beads (yellow arrows) in it and the fibers are discontinuous and tightly packed.

All other electrospun mats prepared with different concentrations of Fe_3O_4 nanopowder, apart from the ones shown above (3 wt. %), also had the same morphology. The mats prepared at 15 KV had spindle shaped beads in it for all other concentrations of Fe_3O_4 nanopowder and the mats electrospun at 25 KV were very densely packed and had spindle shaped as well as circular beads and discontinuous fibers. As a result, these mats were not considered suitable enough for cell studies and further characterization.

There are many factors affecting the occurrence of beads, such as applied voltage, visco-elasticity of the solution, charge density and surface tension of the solution. Since all other parameters were kept constant, there were chances that applied voltage had an effect on the morphology of the fibers.

Also, fiber jet stability is closely associated with the applied voltage during the electrospinning process. When the voltage was at 15 kV, solution droplets were found to be dropping down continuously from

the tip of the needle. But with an increase in the voltage to 25 KV, the jet started to become quite unstable, resulting in two fiber jets at the tip of the needle occasionally.

Based on the morphology of the fibers, the samples that were chosen for further characterization such as fiber diameter distribution, magnetic measurements, mechanical testing etc. were the ones electrospun at 20 KV since the mats had continuous fibers and were bead free.

A few other parameters were varied such as the flow rate and the distance between the tip of the needle and the collector to optimize the morphology of the mats (Data not shown).The most suitable values of flow rate and distance were chosen to be 2 mL/hr and 19 cm respectively.

Testing different voltages, concentration of Fe_3O_4 nanopowder, flow rates (images not shown) and distance between the tip of the needle and the collector yielded the most suitable parameters to electrospin SF/PEO solution with Fe_3O_4 nanopowder at different concentrations which have been listed in Table 9.

Table 9: Established parameters to electrospin SF/PEO with Fe_3O_4 nanopowder.

Applied Voltage	20 KV
Ratio and concentrations of the solution	4:1 blend solution of 7% SF: 5% PEO
Flow rate	2 mL/hr
Distance between tip of the needle and collector	19 cm
Maximum concentration of Fe_3O_4 nanopowder in 5ml of SF/PEO solution	10 wt. %
Collector	Flat surface rotating collector

4.2 LIGHT MICROSCOPY IMAGE ANALYSIS

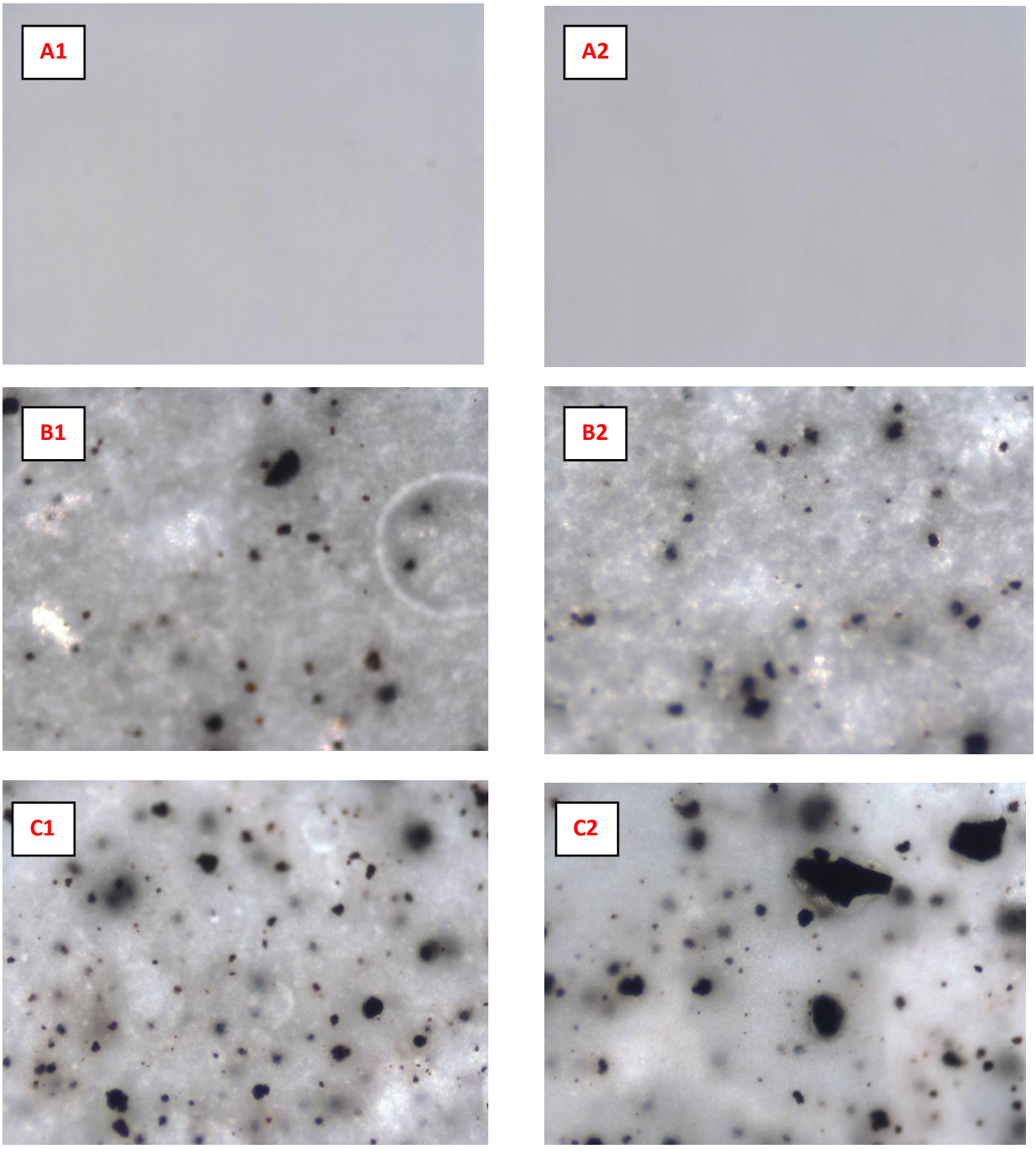

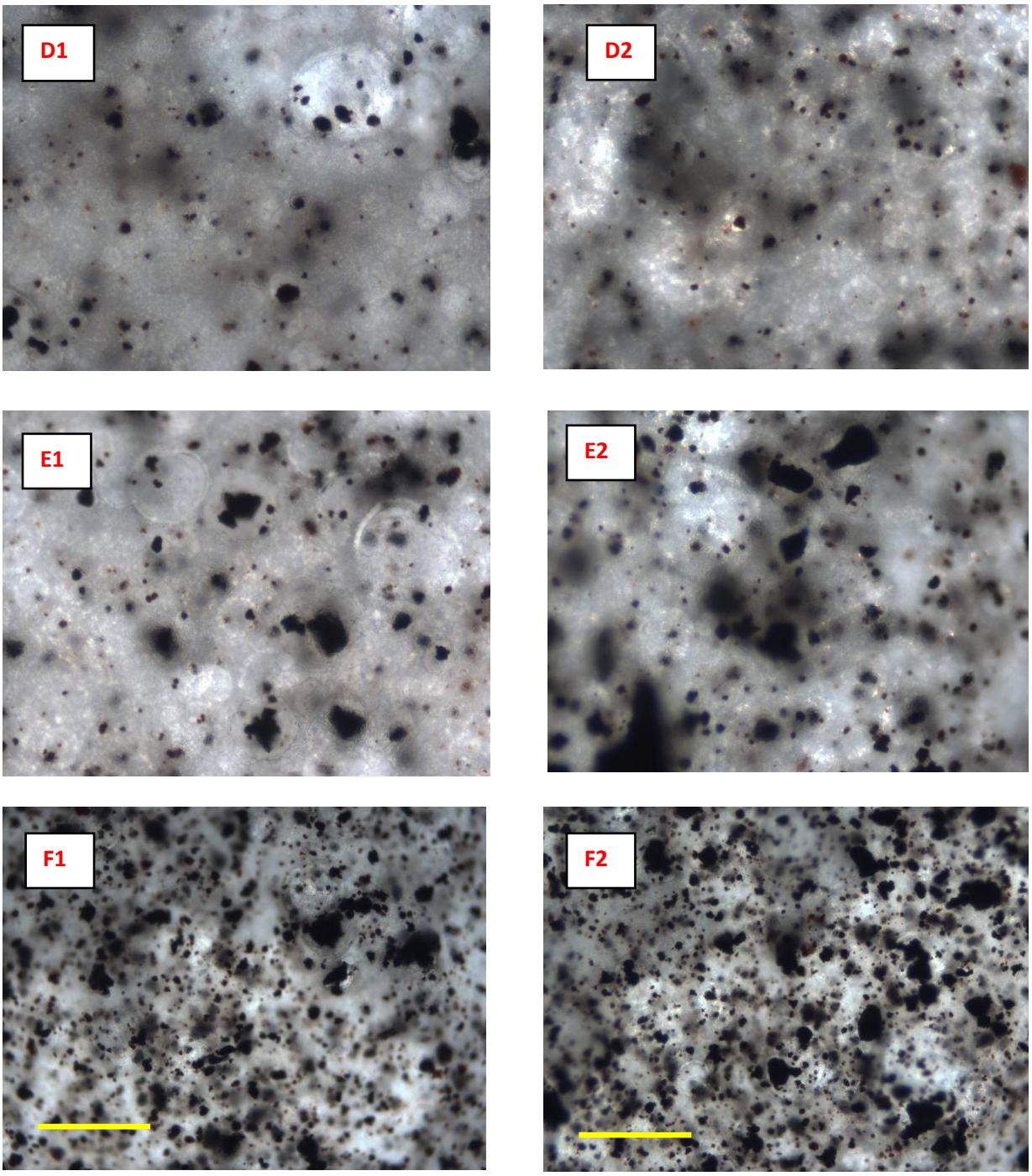

Figure 23: Light microscope images at magnification of 20X of the samples prepared at 20 KV.**A1, A2**: SF/PEO mat with no Fe_3O_4 particles.**B1, B2**: SF/PEO/1 wt. % Fe_3O_4 mat.**C1, C2**: SF/PEO/3 wt. % Fe_3O_4 mat.**D1, D2**: SF/PEO/5 wt. % Fe_3O_4 mat.**E1, E2**: SF/PEO/7 wt. % Fe_3O_4 mat. **F1, F2**: SF/PEO/10 wt. % Fe_3O_4 mat. **Scale bar- 100 µm**

As shown in Figure 23 above, SF/PEO electrospun mat with no particles in it had no dark regions in the mat when seen under the light microscope at magnification 20 X whereas a few particles were seen in the SF/PEO/1 wt. % Fe_3O_4 mat. The average aggregate size was 195 ± 118 nm. The SF/PEO/3 wt. % Fe_3O_4 mat had more particles per unit area and the average aggregate size was 251 ± 134 nm. As the concentration of Fe_3O_4 was increased in the solution, the mats appeared greyer with more particles per unit area such as SF/PEO/5 wt. % Fe_3O_4 mat. The average aggregate size was 287 ± 221 nm. As expected, maximum number of particles per unit area was observed in SF/PEO/10 wt. % Fe_3O_4 mat under the microscope with particles in SF/PEO/7 wt. % Fe_3O_4 mat being only a little less than the former mat. The average aggregate size for the mats electrospun using 7 wt. % Fe_3O_4 and 10 wt. % Fe_3O_4 were 370 ± 241 nm and 433 ± 155 nm.

The increase in the average aggregate size of Fe_3O_4 particles is directly related to the increase in the concentration of Fe_3O_4 nanopowder. Due to nanoparticles' high surface area to volume ratio, more aggregates are formed because of attractive van der Waals forces between the particles which bring together the nanosized particles to reduce the energy associated with the high surface area to volume ratio.

4.3 SEM IMAGE ANALYSIS

SEM image analysis was done on mats electrospun at 20 KV using different concentrations of Fe_3O_4 to reveal fiber morphology and fiber diameter distribution and to determine the exact position of the particles on or inside the mats (Figure 24-29).

A

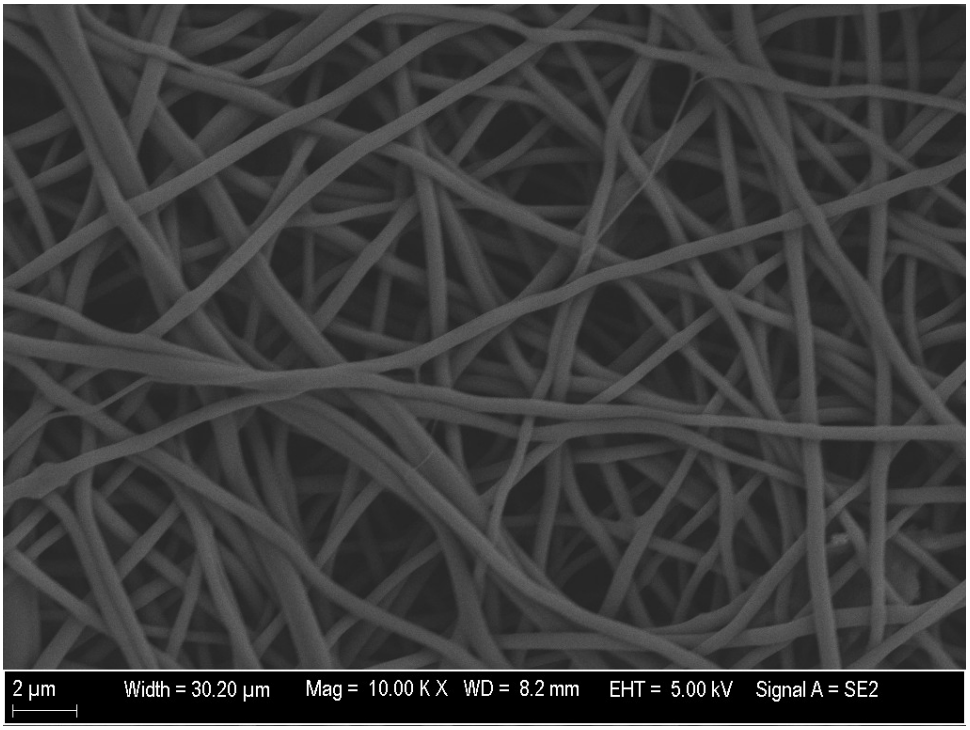
2 µm
Width = 30.20 µm
Mag = 10.00 K X
WD = 8.2 mm
EHT = 5.00 kV
Signal A = SE2

B

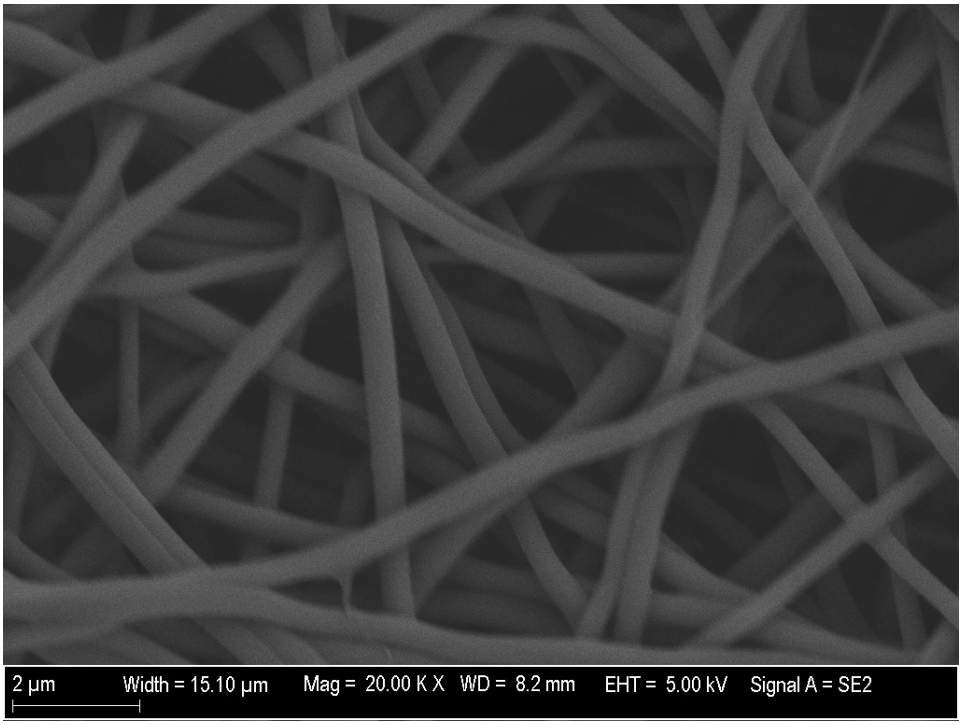
2 µm
Width = 15.10 µm
Mag = 20.00 K X
WD = 8.2 mm
EHT = 5.00 kV
Signal A = SE2

C

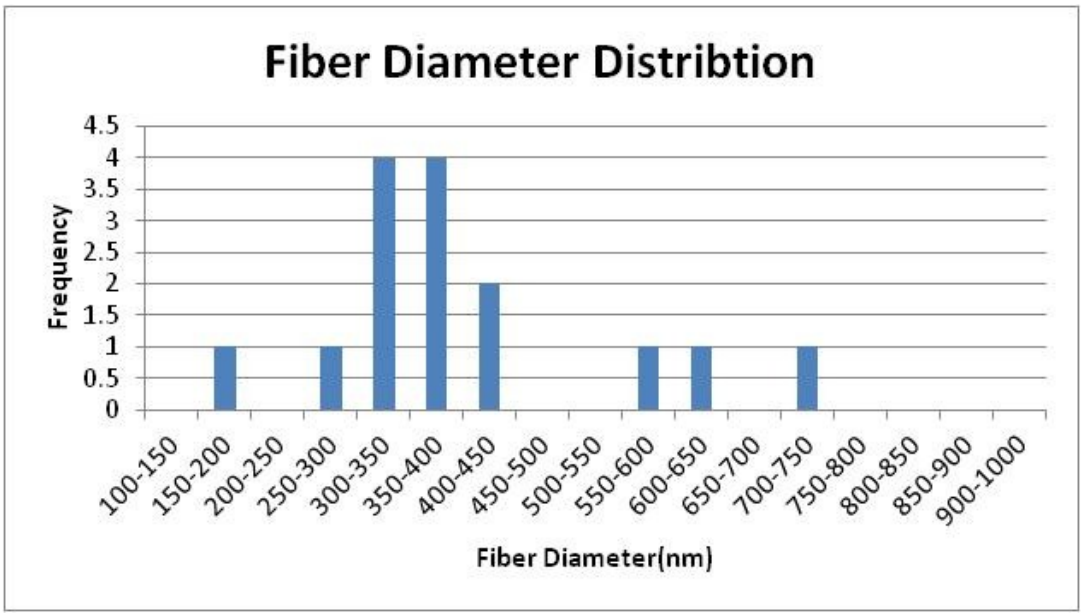

Figure 24: SEM image of SF/PEO mat electrospun at 20 KV. A) At 10 kX. B) At 20 kX C) Fiber diameter distribution.

A

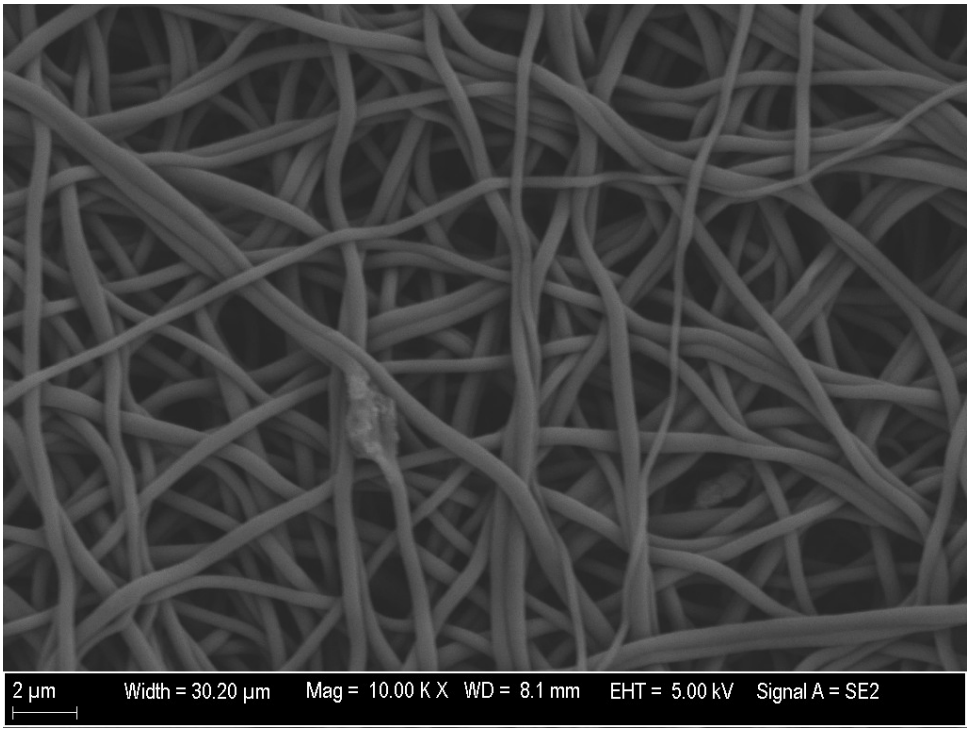
2 µm
Width = 30.20 µm
Mag = 10.00 K X
WD = 8.1 mm
EHT = 5.00 kV
Signal A = SE2

B

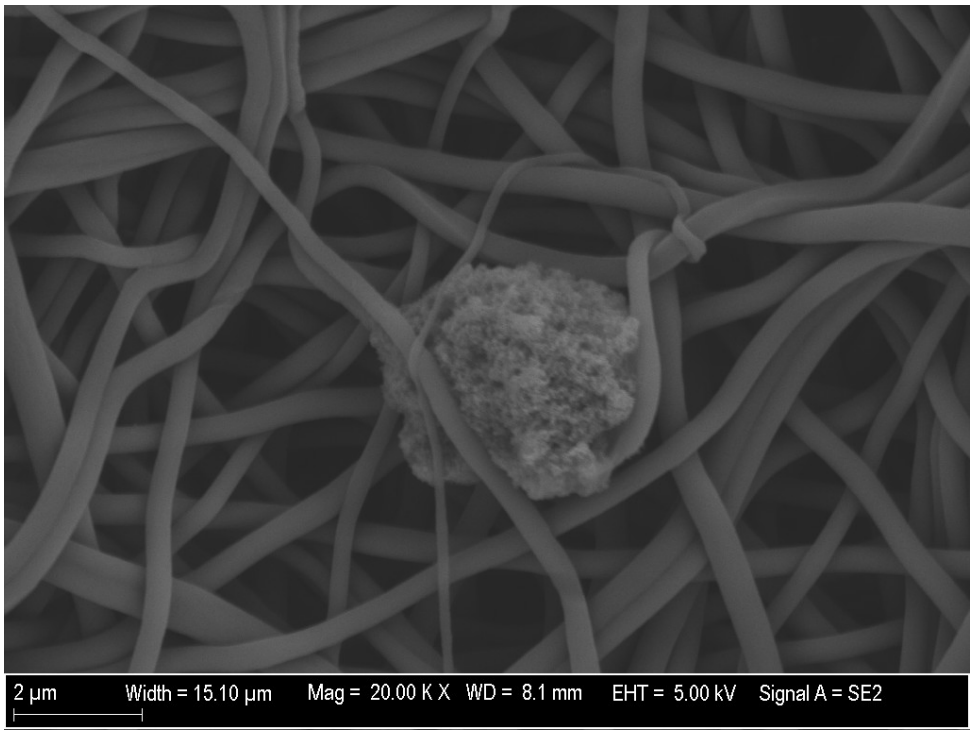
2 µm
Width = 15.10 µm
Mag = 20.00 K X
WD = 8.1 mm
EHT = 5.00 kV
Signal A = SE2

C

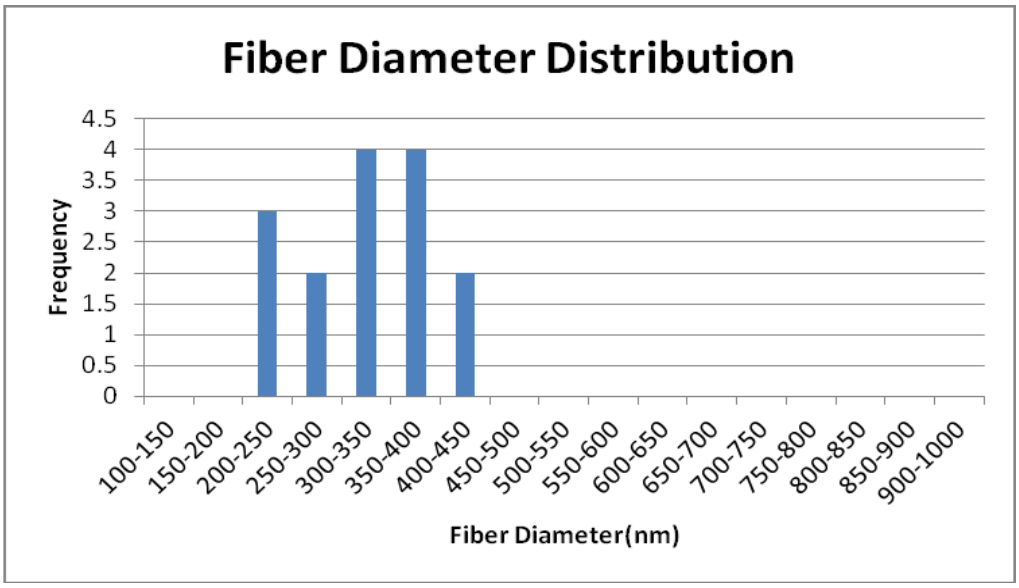

Figure 25: SEM image of SF/PEO/1 wt. % Fe_3O_4 mat electrospun at 20 KV. A) At 10 kX. B) At 20 kX C) Fiber diameter distribution.

A

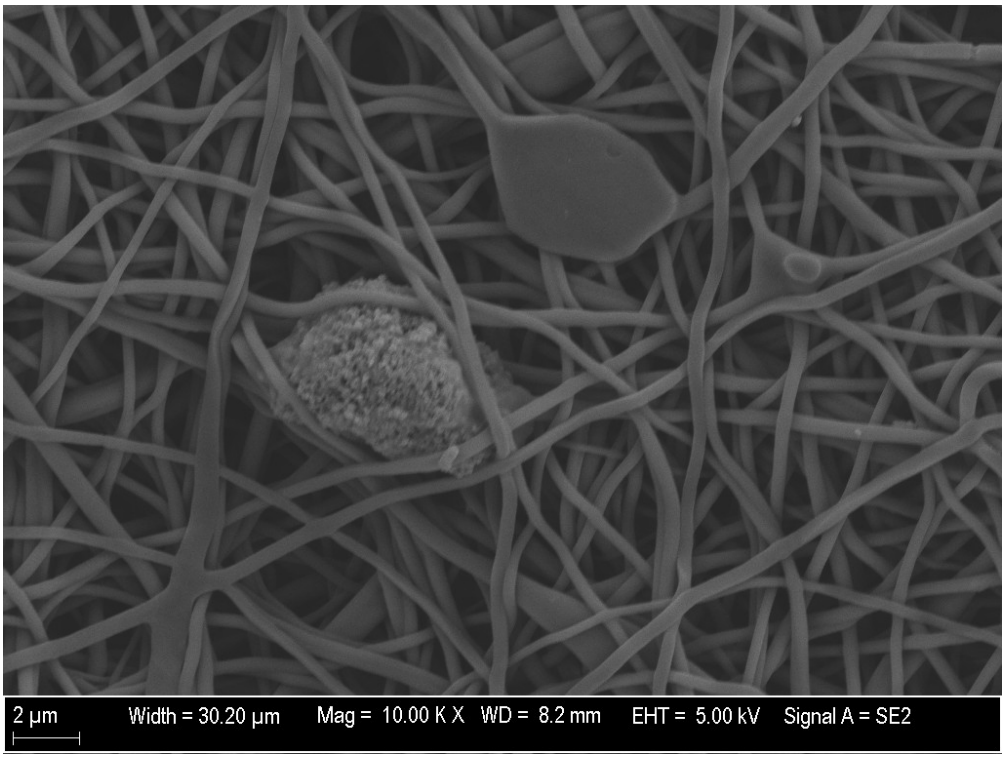
2 µm
Width = 30.20 µm
Mag = 10.00 K X
WD = 8.2 mm
EHT = 5.00 kV
Signal A = SE2

B


1 µm
Width = 15.10 µm
Mag = 20.00 K X
WD = 8.2 mm
EHT = 5.00 kV
Signal A = SE2

C

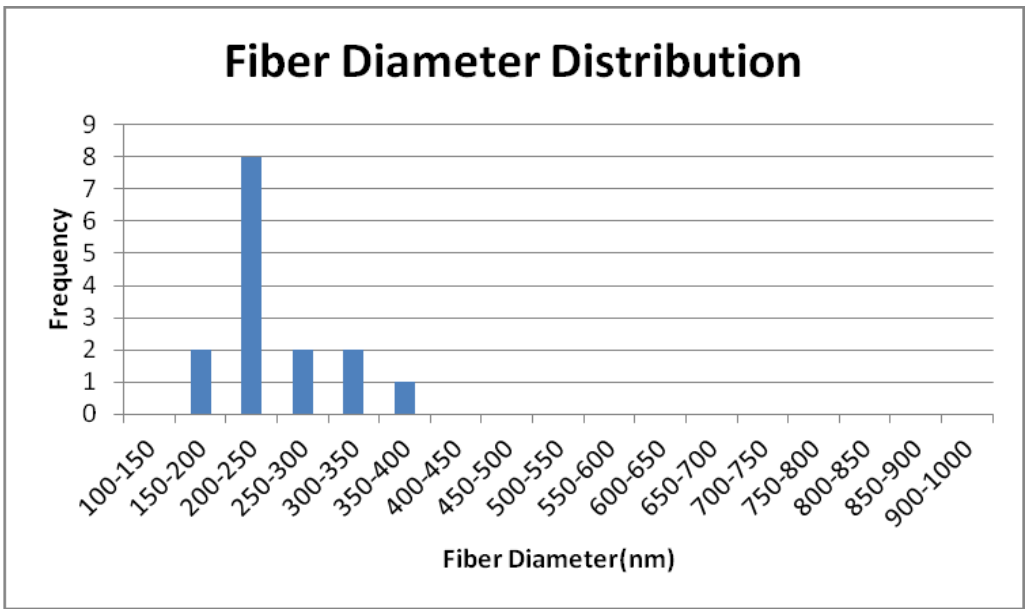

Figure 26: SEM image of SF/PEO/3 wt. % Fe_3O_4 mat electrospun at 20 KV. A) At 10 kX. B) At 20 kX C) Fiber diameter distribution.

A

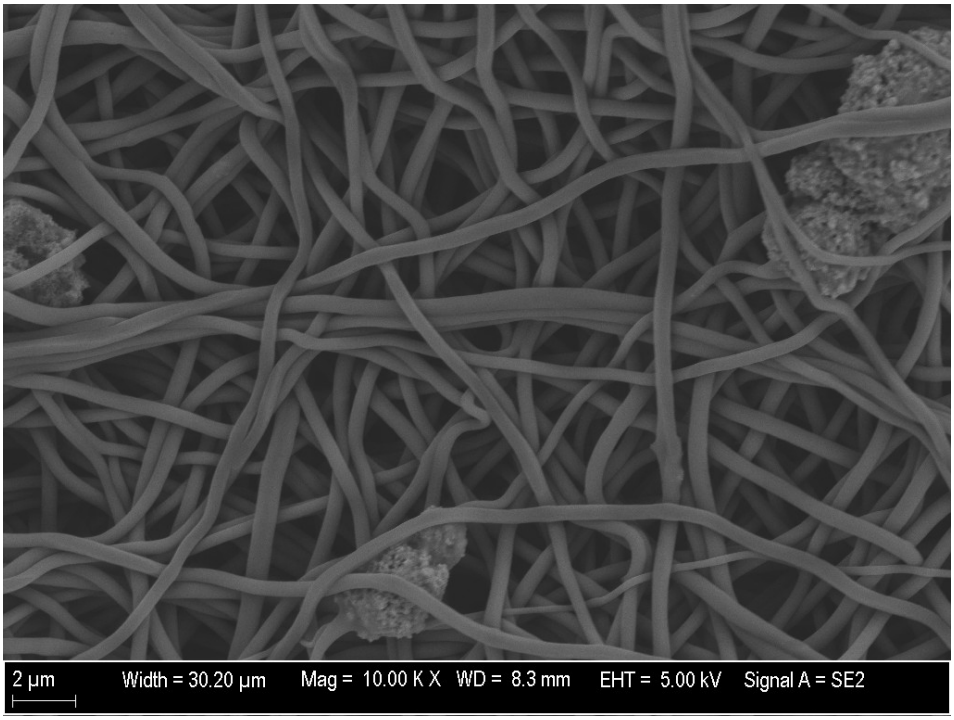
2 µm
Width = 30.20 µm
Mag = 10.00 K X
WD = 8.3 mm
EHT = 5.00 kV
Signal A = SE2

B


2 µm
Width = 15.10 µm
Mag = 20.00 K X
WD = 8.3 mm
EHT = 5.00 kV
Signal A = SE2

C

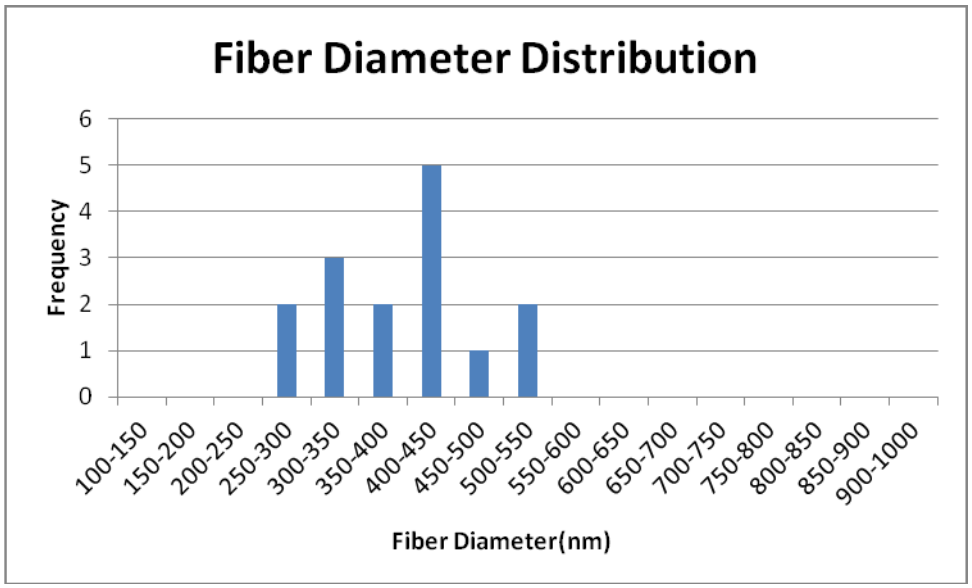

Figure 27: SEM image of SF/PEO/5 wt. % Fe_3O_4 mat electrospun at 20 KV. A) At 10 KX. B) At 20 KX C) Fiber diameter distribution.

A

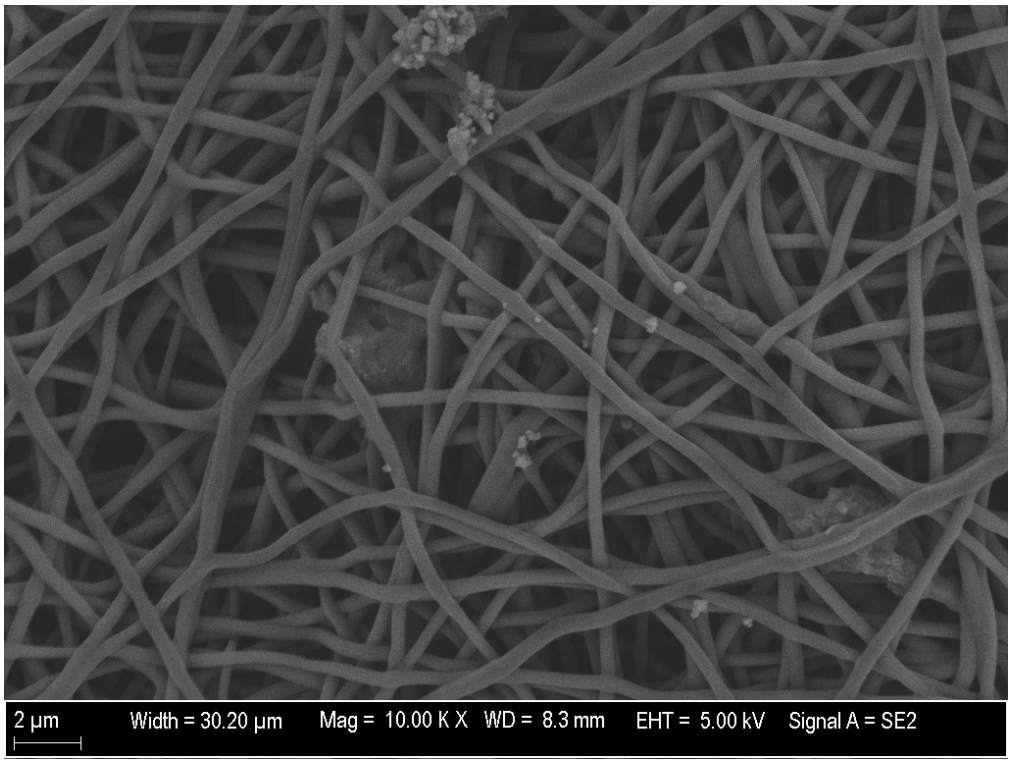
2 µm
Width = 30.20 µm
Mag = 10.00 K X
WD = 8.3 mm
EHT = 5.00 kV
Signal A = SE2

B

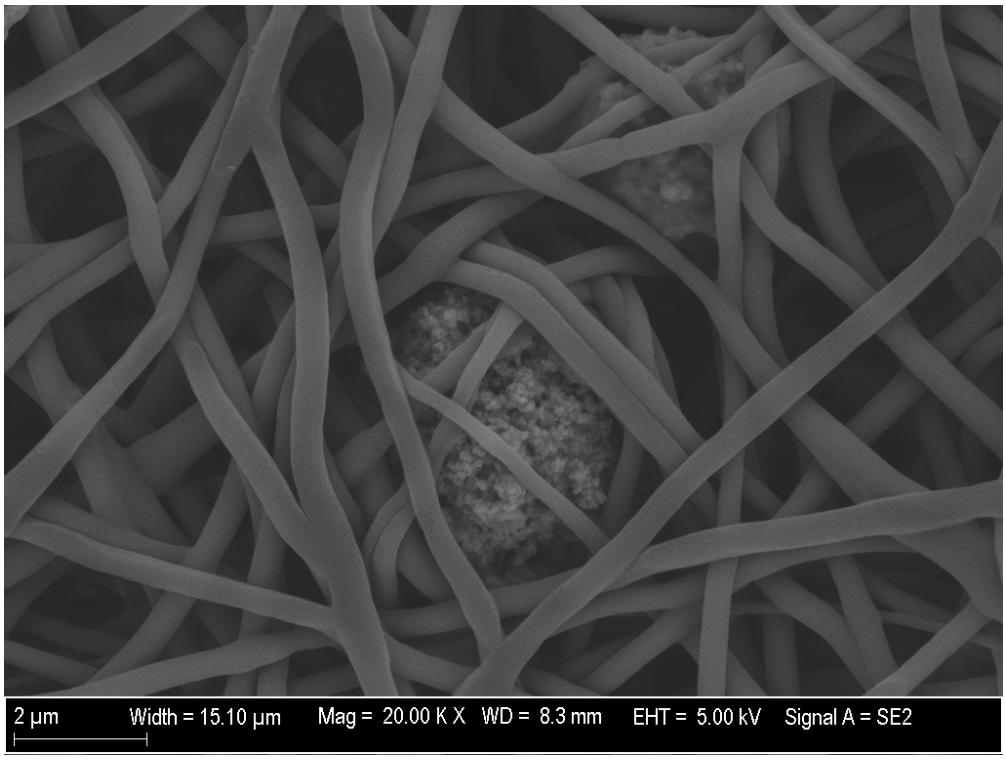
2 µm
Width = 15.10 µm
Mag = 20.00 K X
WD = 8.3 mm
EHT = 5.00 kV
Signal A = SE2

C

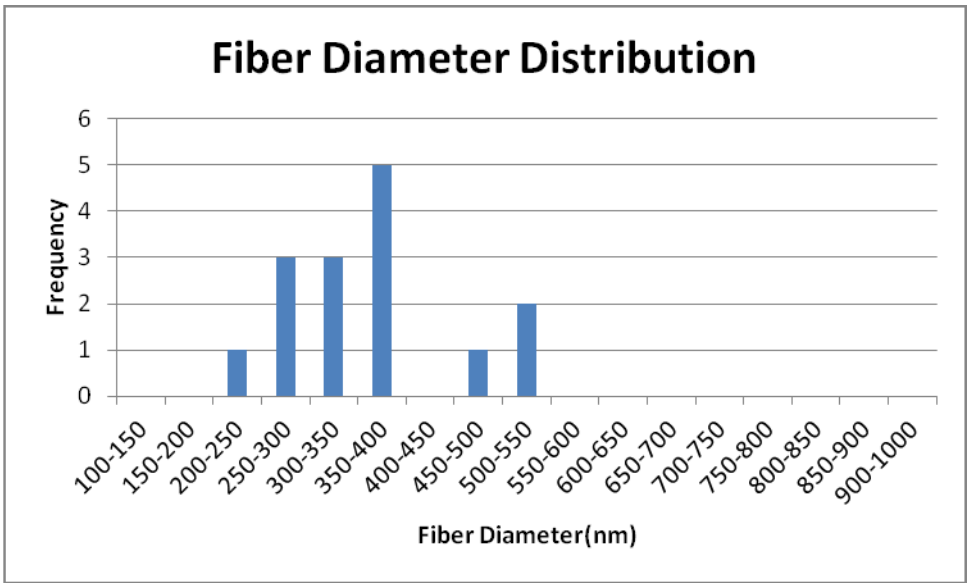

Figure 28: SEM image of SF/PEO/7 wt. % Fe_3O_4 mat electrospun at 20 KV. A) At 10 kX. B) At 20 kX C) Fiber diameter distribution

A

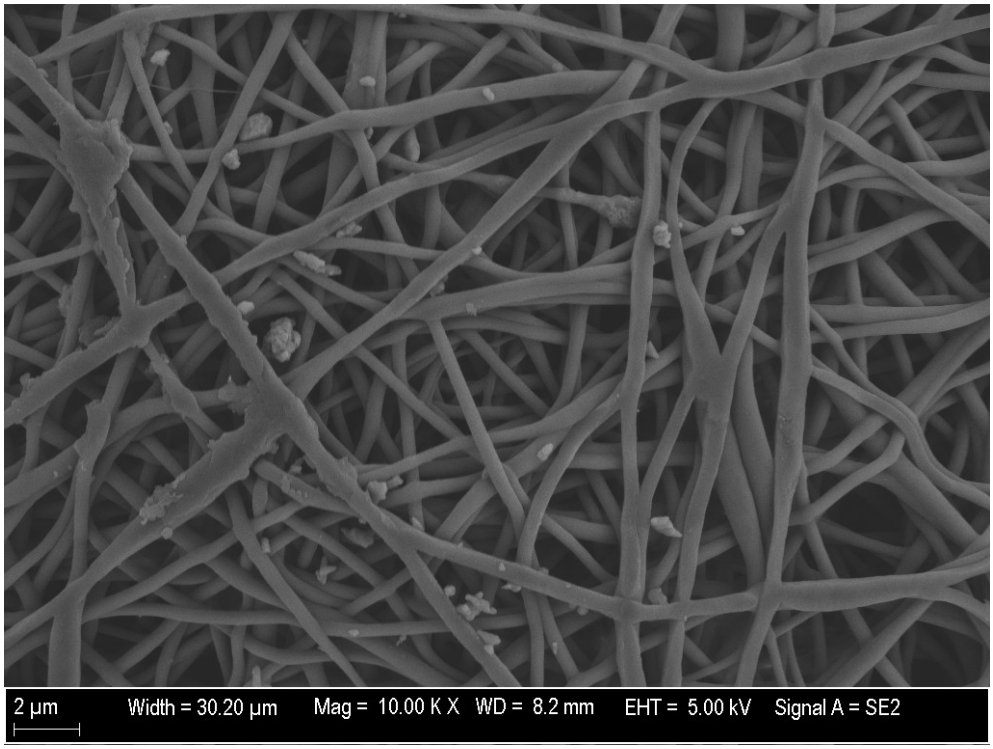
2 µm
Width = 30.20 µm
Mag = 10.00 K X
WD = 8.2 mm
EHT = 5.00 kV
Signal A = SE2

B

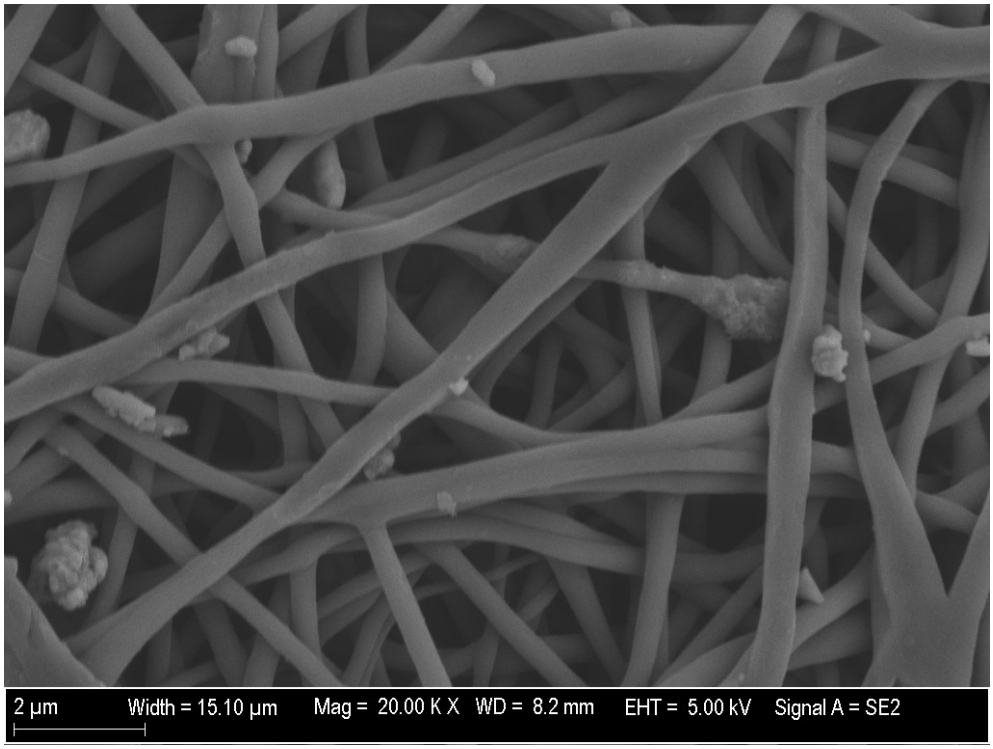
2 µm
Width = 15.10 µm
Mag = 20.00 K X
WD = 8.2 mm
EHT = 5.00 kV
Signal A = SE2

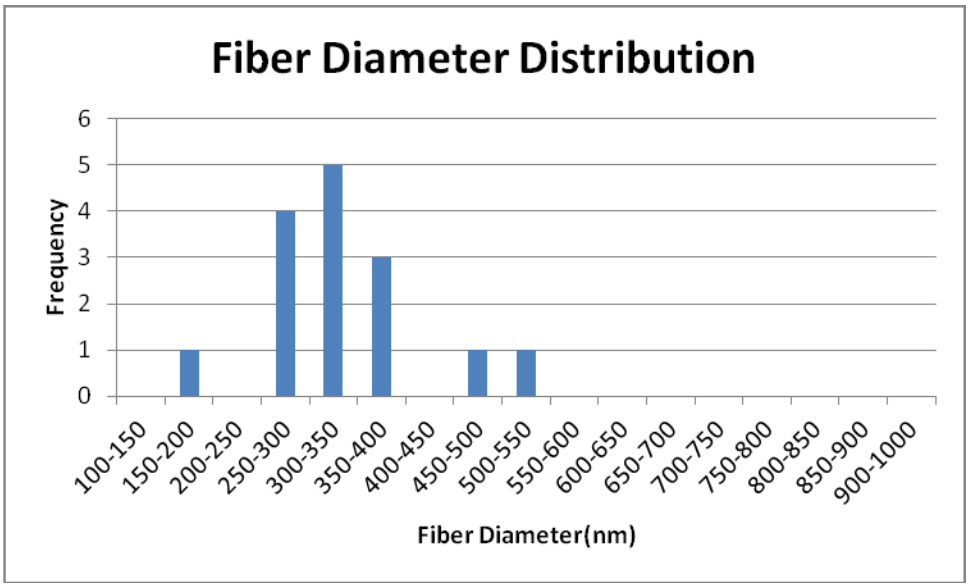

Figure 29: SEM image of SF/PEO/10 wt. % Fe_3O_4 mat electrospun at 20 KV. A) At 10 kX. B) At 20 kX C) Fiber diameter distribution.

Table 10: Fiber Diameter Distribution of electrospun mats at variable concentrations of Fe_3O_4

Electrospun mats	Average Fiber Diameter (nm)
Silk fibroin	640 ± 155.4 nm
Silk + 1 wt. % Fe_3O_4	543.2 ± 74.2 nm
Silk + 3 wt. % Fe_3O_4	452.3 ± 56.6 nm
Silk + 5 wt. % Fe_3O_4	399.2 ± 80.2 nm
Silk + 7 wt. % Fe_3O_4	360.9 ± 80.2 nm
Silk + 10 wt. % Fe_3O_4	338.2 ± 80.4 nm

Figure 24 A) and 24 B) shown above, are the SEM image of the SF/PEO mat electrospun at 20 KV taken at 10 kX and 20 kX magnification respectively. The mats were bead free and there were no signs of discontinuity of fibers. This was a result of the stable Taylor cone formation at 20 KV and 2 ml/hr flow rate. The average fiber diameter for the SF/PEO mat was 640 ± 155.4 nm as seen in Figure 24 C).

With the addition of the Fe_3O_4 particles to it at concentration of 1 wt. %, the fiber diameter reduced to 543.2 ± 74.2 nm (Figure 25 A), B) and C)). The presence of Fe_3O_4 particles in the form of aggregates was also noticed. Figure 26 shows the SEM images of the SF/PEO/3 wt. % Fe_3O_4 electrospun mats at high magnifications of 10kX (Figure 26A) and 20 kX(Figure 26B).The average fiber diameter further reduced to 452.3 ± 56.6 nm (Figure 26 C), as summarized in Table 10, and more Fe_3O_4 particles seen per unit area as compared to SF/PEO/1 wt. % Fe_3O_4 electrospun mats.

Further increase in the concentration of Fe_3O_4 particles from 3 wt. % to 5 wt. % to 7 wt. % and finally to 10 wt. % not only reduced the fiber diameter but also made visible more and more particles on the surface of the mats.

The average fiber diameter for the SF/PEO/5 wt. % Fe_3O_4 electrospun mat was 399.2 ± 80.2 nm, for SF/PEO/7 wt. % Fe_3O_4 electrospun mat was 360.86 ± 80.2 nm and for SF/PEO/10 wt. % Fe_3O_4 electrospun mat was 338.2 ± 80.4 nm as shown in the Figures 27(A, B, C), Figure 28(A, B, C) and Figure 29(A, B, C) respectively.

For the highest concentration of Fe_3O_4 particles at 10 wt. %, the mats had the maximum number of particles or aggregates visible on the surface of the mat, in between the layers of the mats and in between the fibers.

The reason for thinning of fibers could be due to the effects of viscosity, conductivity, surface tension, solution composition or solution concentration.

4.4 TEM IMAGE ANALYSIS

To further investigate the morphology and the location of the Fe_3O_4 particles in the mats, TEM was performed. With TEM, due to the variations in electron wave scattering between different materials, contrast was seen between the silk fibers and the Fe_3O_4 particles. The particles were more clearly identified as they appeared darker due to the contrast.

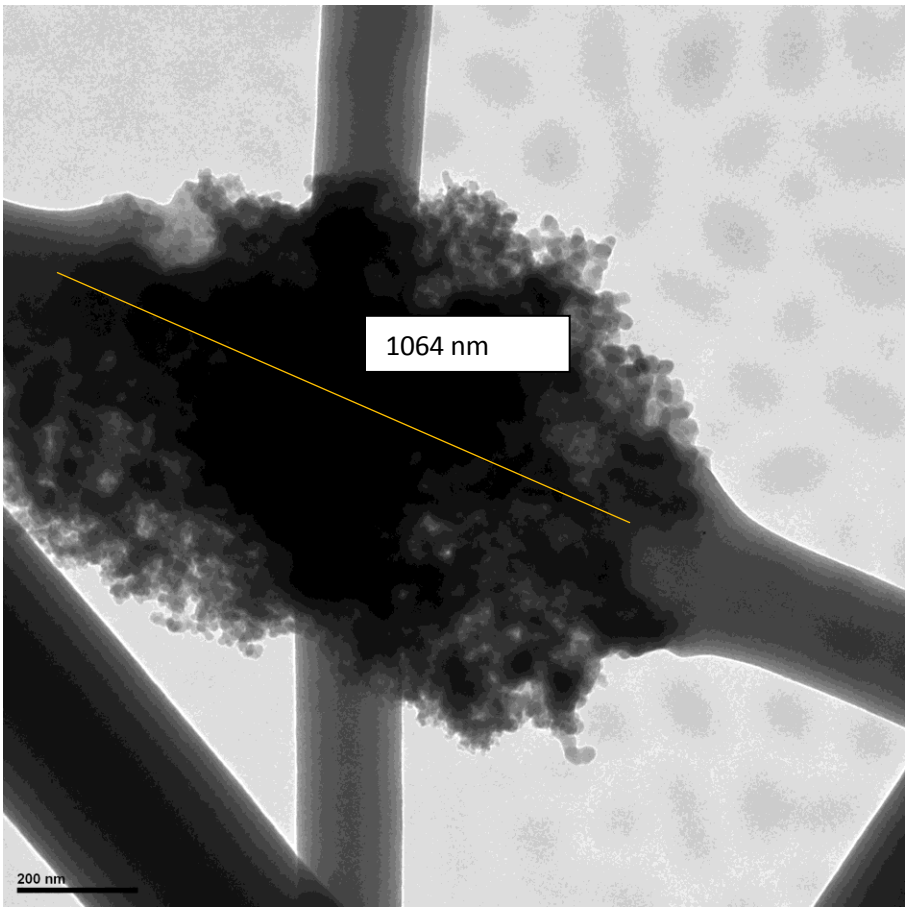

Figure 30: TEM image of SF/PEO fiber containing 1 wt. % Fe_3O_4. The particles serve as a part of the fiber, holding the SF fibers together. **Scale bar- 200 nm**

As shown above in Figure 30, the Fe_3O_4 aggregate of 1064 nm length was seen in between the two end of the silk fibers. The aggregate was holding the Silk fibroin fiber together but was also serving as a part of the fiber. In other words, aggregates served as a bridge to maintain the continuity of the mat.

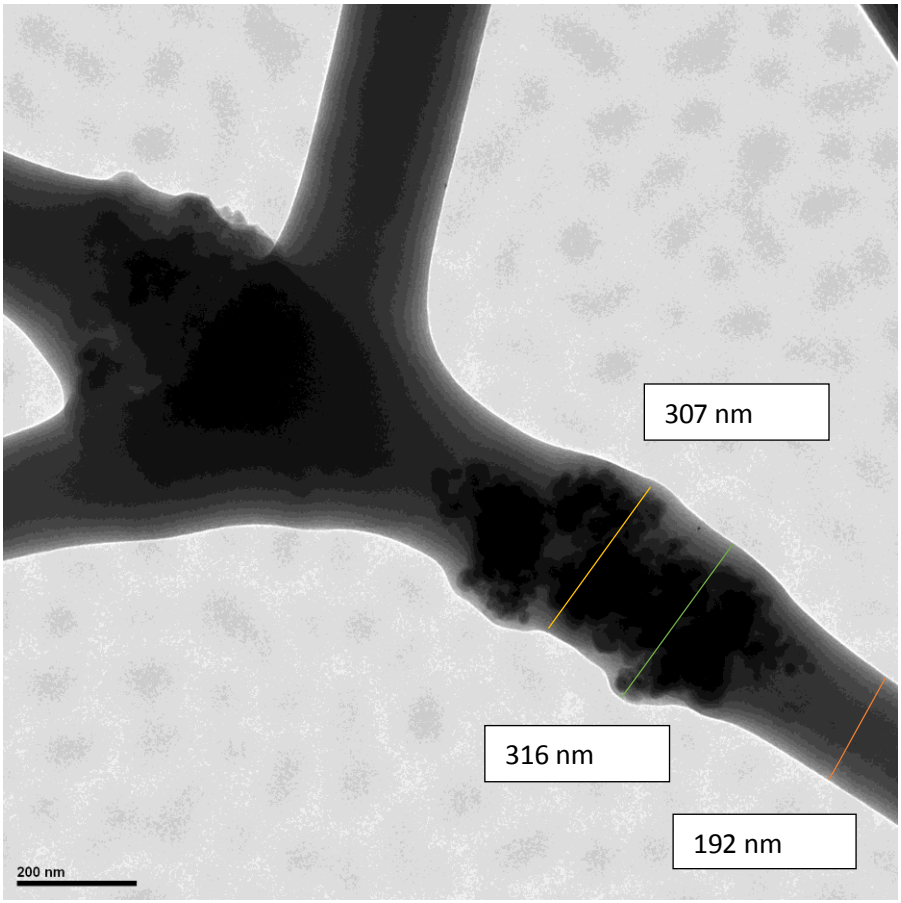

Figure 31: TEM image of SF/PEO fiber containing 3 wt. % Fe_3O_4.Particles were seen concentrated within Silk fibroin fibers. **Scale bar- 200 nm**.

Fe_3O_4 particles and aggregates not only served as a bridge between the silk fibroin fibers but were also seen present inside the fibers. Figure 31 clearly shows that small aggregates as well as individual particles that had diameter less than the diameter of the silk fibroin fiber were able to be concentrated inside the fiber resulting in a bumpy structure of the fibers. The thickness of the fibers, as measured using image J, without any particles inside it, was about 192 nm. Due to the Fe_3O_4 particles incorporation in the fibers, the thickness of the fibers increased more than 1.5 times to 316 nm. As shown below in

Figure 32, Fe_3O_4 particles were found concentrated on top of the fibers and partially forming a part of the fiber.

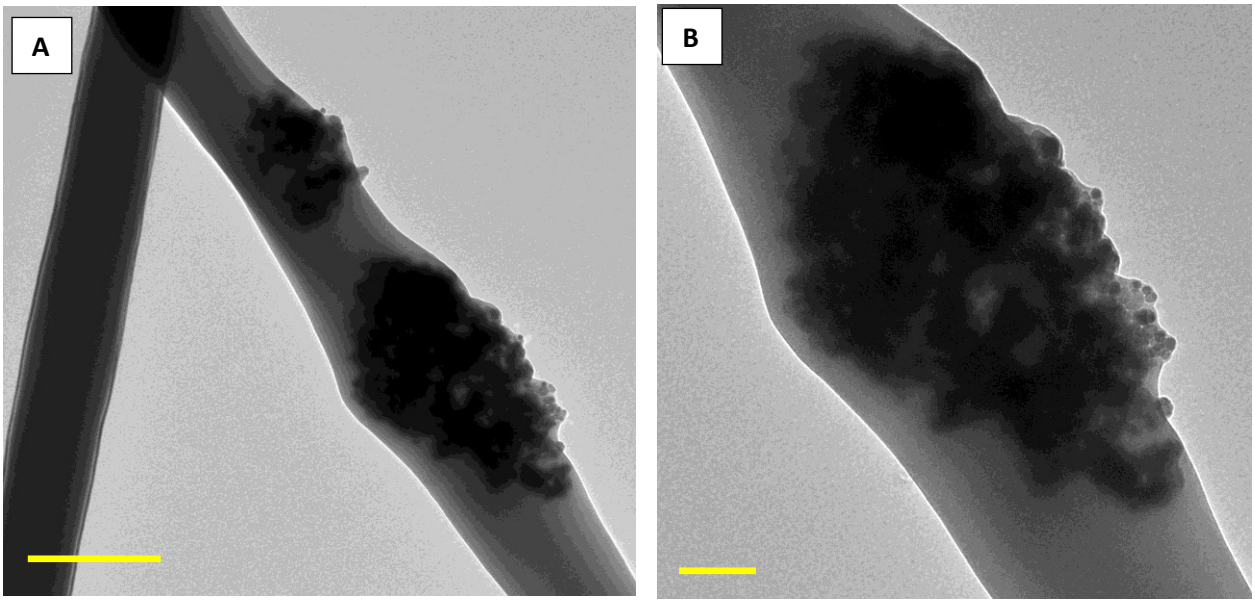

Figure 32: TEM images of SF/PEO fiber containing 7 wt. % Fe_3O_4.A) Scale bar-0.5 µm. B) Scale bar-200 nm.

The morphology of Fe_3O_4 particles within the mats was similar for all the mats electrospun at different concentrations of Fe_3O_4. The presence of Fe_3O_4 particles and aggregates was seen on the fibers, within the fibers and as a bridge holding the fibers.

4.5 MESH CHARACTERIZATION- VOID AREA FRACTION ANALYSIS

Using Image J software, SEM images of the electrsopun mats prepared at 20 KV were processed to estimate the void area fraction by setting the threshold to exclude void spaces to compare the porosity between the mats.

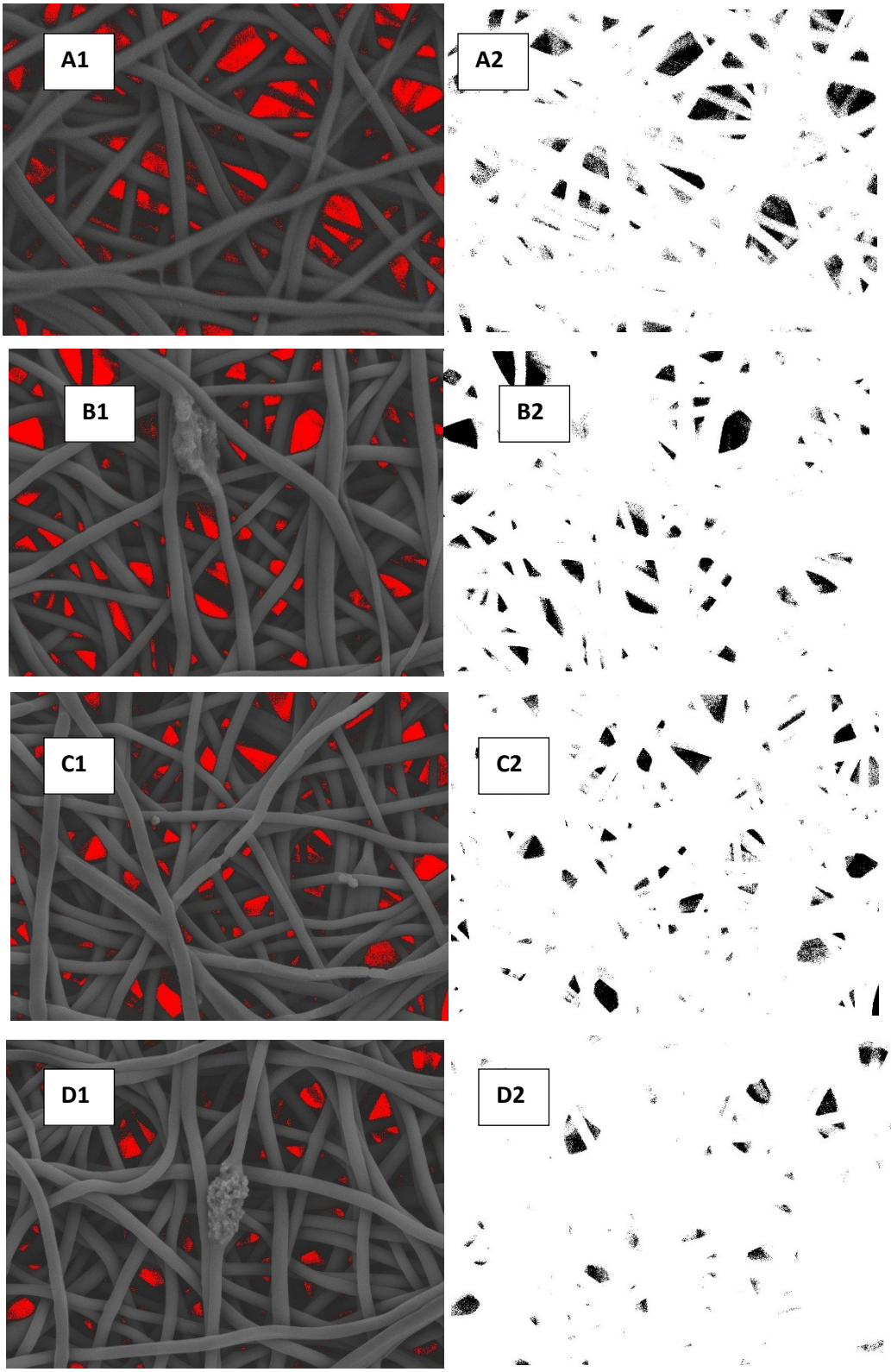
A1
A2
B1
B2
C1
C2
D1
D2

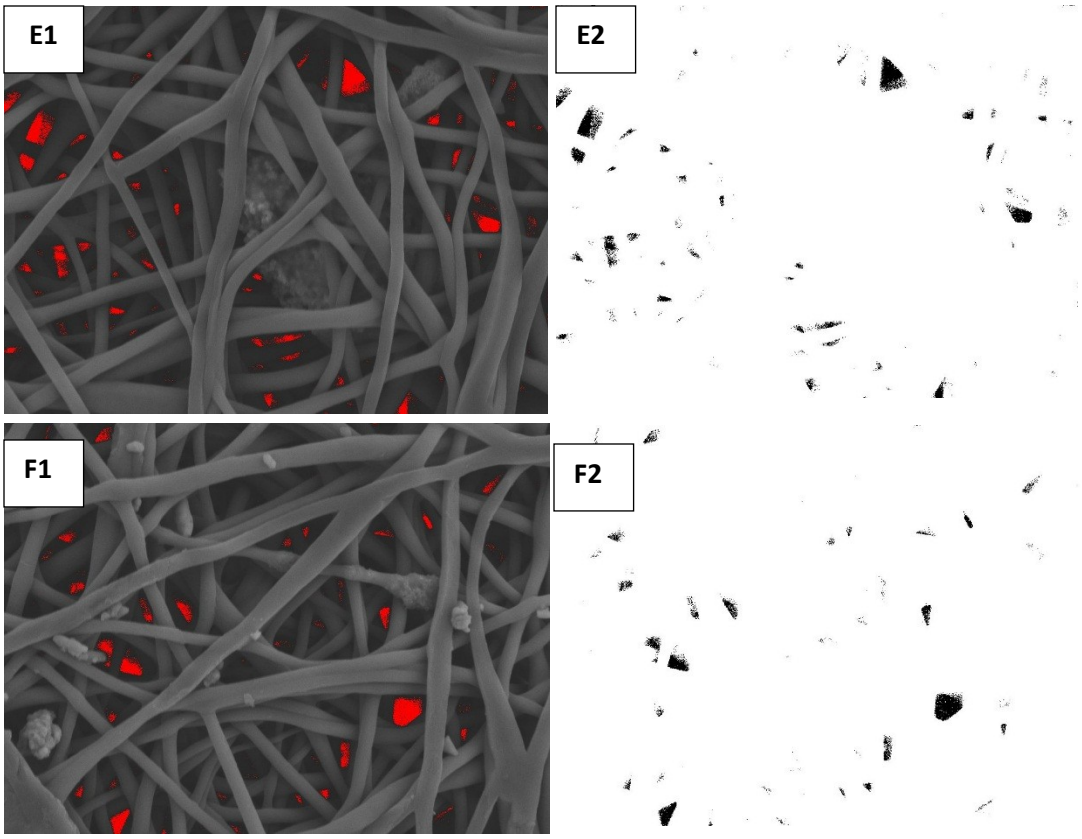

Figure 33: Comparison of void area fraction among the samples.A1, A2- SF/PEO mats, B1, B2- SF/PEO/1 wt. % Fe_3O_4, C1, C2- SF/PEO/3 wt. % Fe_3O_4, D1, D2- SF/PEO/5 wt. % Fe_3O_4, E1, E2- SF/PEO/7 wt. % Fe_3O_4, F1, F2- SF/PEO/10 wt. % Fe_3O_4.

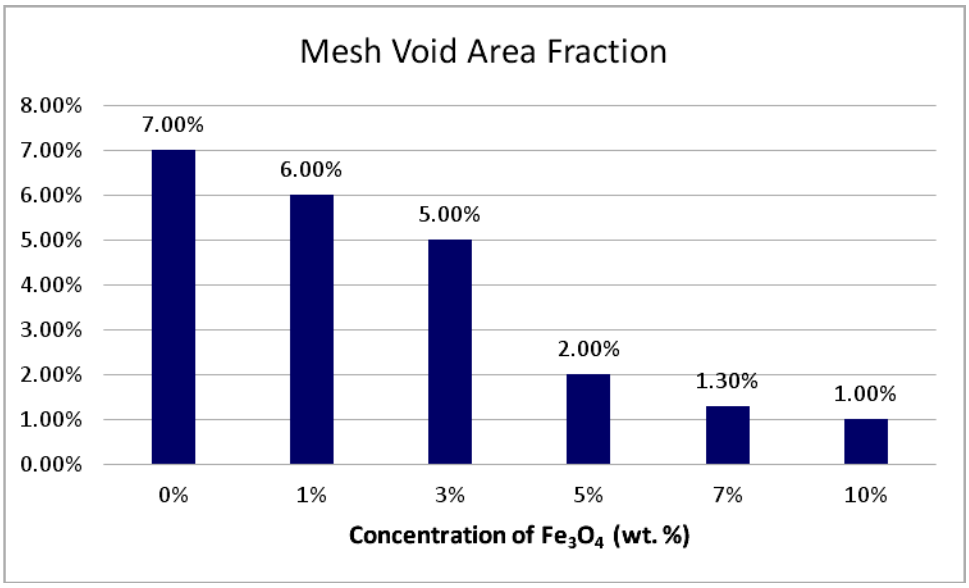

Figure 34: Graphical representation of the Void Area Fraction for the samples at different concentration of Fe_3O_4.

SEM images of the samples, that were prepared using the method described above, were taken using the Everhart-Thornley secondary electron detector at 20 kX. 1 image was analyzed from each sample and comparison between void area fraction for each sample was calculated (Table 11).

Table 11: Calculated result of void area fraction of all the samples.

Conc. Of Fe_3O_4 (wt. %)	Void area fraction (%)
0	7.0
1	6.0
3	5.0
5	2.0
7	1.3
10	1.0

The mat electrospun using SF/PEO with 0 wt. % Fe_3O_4 concentration had the maximum void area fraction of 7.0% which was approximately 14 times more than the void area fraction of 6.0% for the mat with 1 wt. % Fe_3O_4 concentration. Void area fraction further decreased to 5.0% and 2.0% for the samples with 3 wt. % Fe_3O_4 and 5 wt. % Fe_3O_4 respectively. The samples prepared using 7 wt. % Fe_3O_4 had half void area fraction than that of the 5 wt. % at 1.3%. The electrospun mat with the maximum concentration of the

Fe_3O_4 (10 wt. %) had the lowest void area fraction value of 1.00% which was 7 times less than the value of the electrospun mat prepared using SF/PEO and similar to that of the sample with 7 wt.% concentration of Fe_3O_4.

The reduction in the void area fraction of the samples with the increase in the concentration of Fe_3O_4 can be attributed to the decrease in the fiber diameter with the increase in the concentration of Fe_3O_4. As a result of the fiber thinning, the fibers in the mat were closely packed leading to the reduction in the void area fraction. Also, Fe_3O_4 particles and aggregates that occupy the space within the void in the mat, on the surface of the mat or within 2 layers of the mat decrease the amount of void area in the mat.

4.6 X-RAY DIFFRACTION ANALYSIS

The electrospun mats prepared at 20 KV were analyzed for determining the changes in the structure of silk fibroin with the addition of Fe_3O_4 particles using X-ray diffraction. Figure 35 shows the XRD data and the lattice planes for mats electrospun using varying concentration of Fe_3O_4 described above.

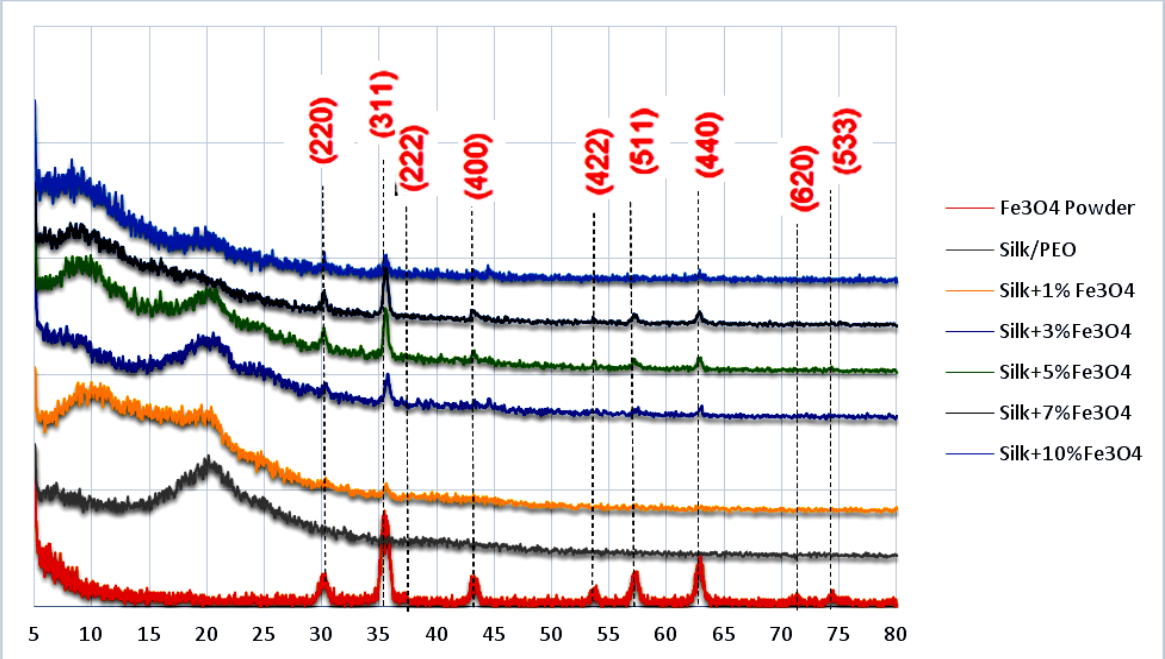

Figure 35: XRD analysis of the electrospun mats at variable concentrations of Fe_3O_4.

With increase in concentration of Fe_3O_4 in the samples, the peaks related to Fe_3O_4 nanopowder at 2θ= 30.3˚, 35.58˚, 43.34˚, 53.86˚, 57.26˚, 62.9˚, 71.66˚ and 74.58˚ became sharper and more prominent except for the samples prepared using 10 wt. % Fe_3O_4. The peaks corresponding to the lattice planes of 311 and 440 had the sharpest peaks followed by peaks corresponding to lattice planes 511, 220 and 400 (Kavich et al., 2010). Diffraction peaks at 10.9 ˚ and 20.4˚ were found in all the samples corresponding to silk I crystalline structure (Q. Lu et al., 2010). Also, peaks at 9.8˚ and 24.3˚ corresponding to silk II crystallite structure were observed in all the samples and became prominent with the increase of Fe_3O_4 in the samples (J. Zhu et al., 2007).

Based on the observation of the diffraction peaks given by Fe_3O_4 in low Fe_3O_4 content mats, it can be concluded that some Iron was not dispersed at the molecular level. Also too much Fe_3O_4 reduces the scattering of the silk. The penetration of the X-rays into the sample depends upon the atomic number of the elements. With large amounts of Fe_3O_4 (7% and 10%) the silk shows only a weak scattering pattern. Strength of the Fe_3O_4 peaks grows systematically with their content, but only up to 7 wt. % concentration. The reason for the weak peaks of Fe_3O_4 in 10 wt. % Fe_3O_4 samples can be attributed to the fact that since it was comparatively difficult to electrospin with such high concentration of Fe_3O_4 powder, Fe_3O_4 worth 10 wt. % was not fully incorporated into the mats. Mats with 7 wt. % Fe_3O_4 had the strongest peaks in comparison to the peaks observed in Fe_3O_4 powder alone signifying that the most effective concentration of Fe_3O_4 powder to be electrospun into mats is 7 wt. %.

The lowest large broad peak from silk is below 10˚ signifying that the mats were more consistent with Silk II structure (J. Zhu et al., 2007). The results of XRD were in accordance with the FTIR deconvolution results.

4.7 FTIR DECONVOLUTION

Fourier transform infrared spectroscopy (FTIR) is a powerful technique to analyze the protein conformation and has been widely used to study the protein structure of silk fibroin. The electrospun mats prepared at 20 KV using variable concentrations of Fe_3O_4 were analyzed using FTIR (Figure 36) to determine the structure of the mats and deconvolution of the data (Figure 37) was done to understand the protein structure in detail (Table 12).

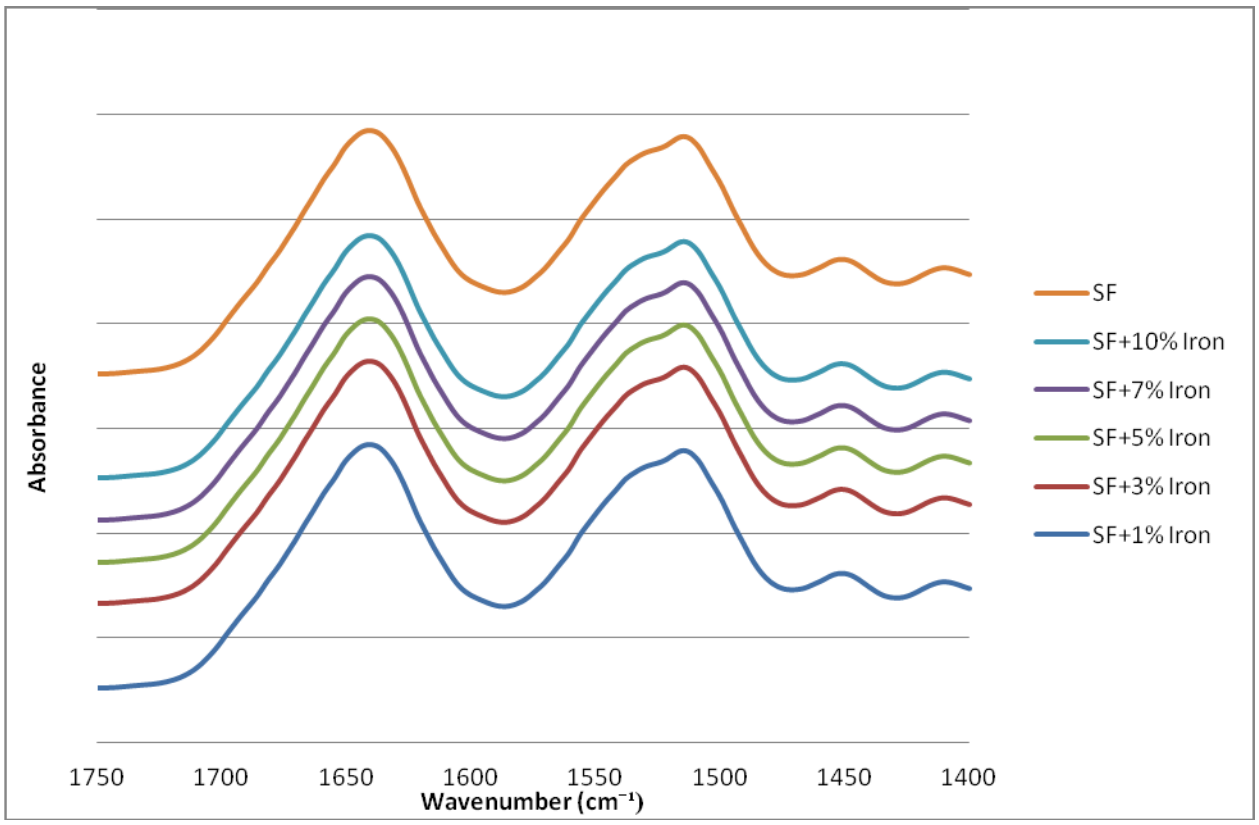

Figure 36: FTIR spectra of silk fibroin scaffolds prepared by using variable concentration of Fe_3O_4 and Fe_3O_4 powder.

The infrared absorption by peptide backbone of amide I (1700-1600 cm^{-1}) and amide II (1600-1500 cm^{-1}) of silk fibroin were analyzed. The peaks corresponding to silk II (β-sheet) structure at 1610-1635 cm^{-1} and 1695-1700 cm^{-1} were seen in the spectra in all the scaffolds. The absorption peaks at 1535-1542 cm^{-1},

indicative of random coil structure according to some studies and silk I structure according to the others, were also seen (Q. Lu et al., 2010).

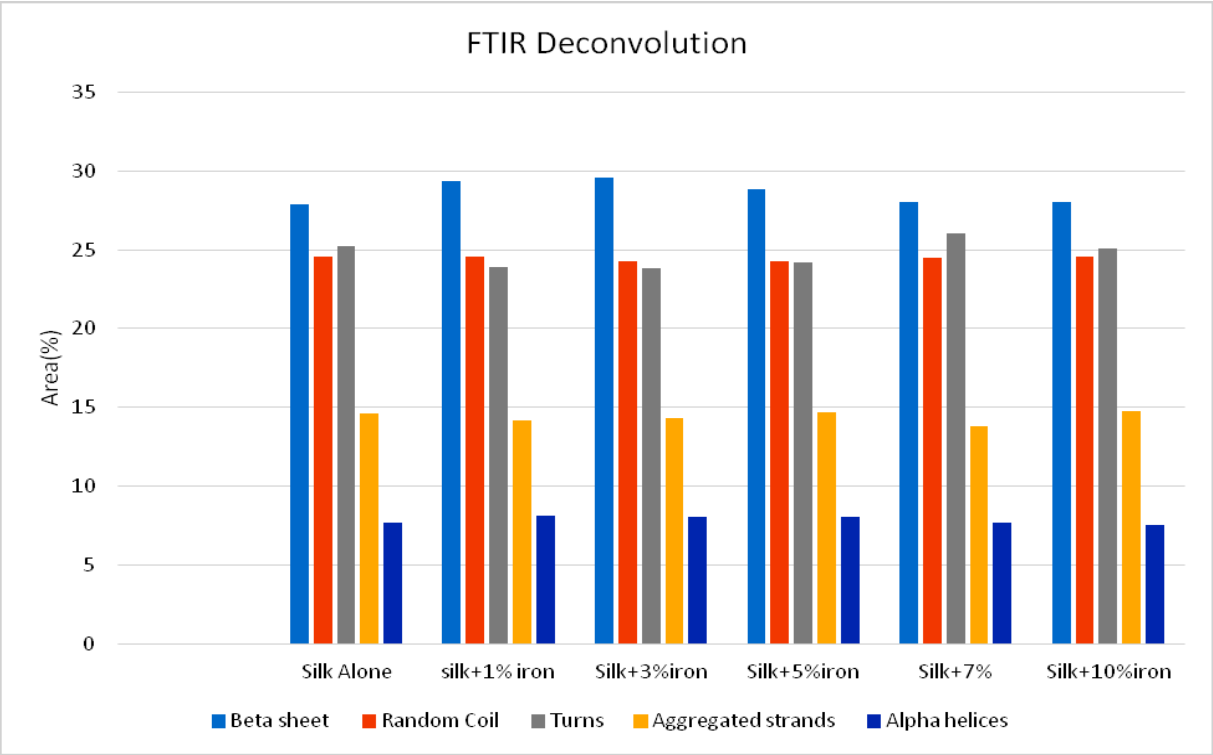

Figure 37: FTIR deconvolution data for electrospun mats prepared using variable concentration of Fe_3O_4.

Deconvoluted data, as shown in Figure 37 above suggests that silk II β-sheet structure, turns and random coil structure co-existed in all the samples. The α-helix structure content was found to be 75 % less than that of β-sheet content indicating the presence of silk II structure in all the mats.

Table 12: FTIR deconvolution results demonstrating the assignment of protein confirmation in the samples

Assignment (Area %)	Silk/PEO	Silk+1% Fe3O4	Silk+3 % Fe3O4	Silk+5% Fe3O4	Silk+7% Fe3O4	Silk+10% Fe3O4
Silk-II, Beta sheet	27.9	29.33	29.53	28.83	28.03	28.05
Random Coil	24.55	24.53	24.26	24.26	24.46	24.55
Turns	25.2	23.86	23.8	24.16	26.03	25.13
Aggregated strands	14.6	14.2	14.34	14.76	13.80	14.75
Alpha helices	7.7	8.1	8.03	8.03	7.72	7.55

The incorporation of Fe_3O_4 did not alter the protein confirmation of silk fibroin. No significant change in the structure of silk structure was observed despite a few small modifications. No additional bands were observed suggesting that there were no significant molecular interactions between silk fibroin and Fe_3O_4 nanoparticles.

4.8 THERMOGRAVIMETRIC ANALYSIS (TGA)

The TGA data was collected and was used to investigate the Fe_3O_4 content in the samples and thermal behavior of the samples with Fe_3O_4 (Figure 38). All the samples weighing 6-10 mg were heated to 600°C. The following calculation was done to estimate the iron content in each sample.

X*Iron weight residue (in %) + (1-X)*Silk weight residue (in %) = Sample weight residue
at 580°C at 580°C at 580°C

x = Iron content in the sample

The iron content calculated using the above formula was higher than expected for all samples. The reason for the higher calculated values could be the non-volatilized carbonaceous char from the silk in the sample (Cebe et al., 2013). Due to these higher calculated values, no result could be drawn regarding the iron content in the samples.

Based on the data, a few results could be drawn regarding the weight loss and effect of iron on the silk. There was minimal weight loss of 3.11 % from 120 to 700°C for Fe_3O_4 powder sample. Also, a difference in temperature was seen in the graph, to degrade the same quantity of sample. The silk degraded to 60% of its original weight at about 345°C which was less than the temperature required to degrade the same amount of silk + 5wt. % Fe_3O_4 scaffold at 360°C. Further increases in temperature degraded silk+10 wt. % Fe_3O_4 sample to 60% of its original weight at 411°C. These values indicated that the addition of Fe_3O_4 stabilized the silk scaffolds resulting in an increased temperature required to degrade the silk scaffolds.

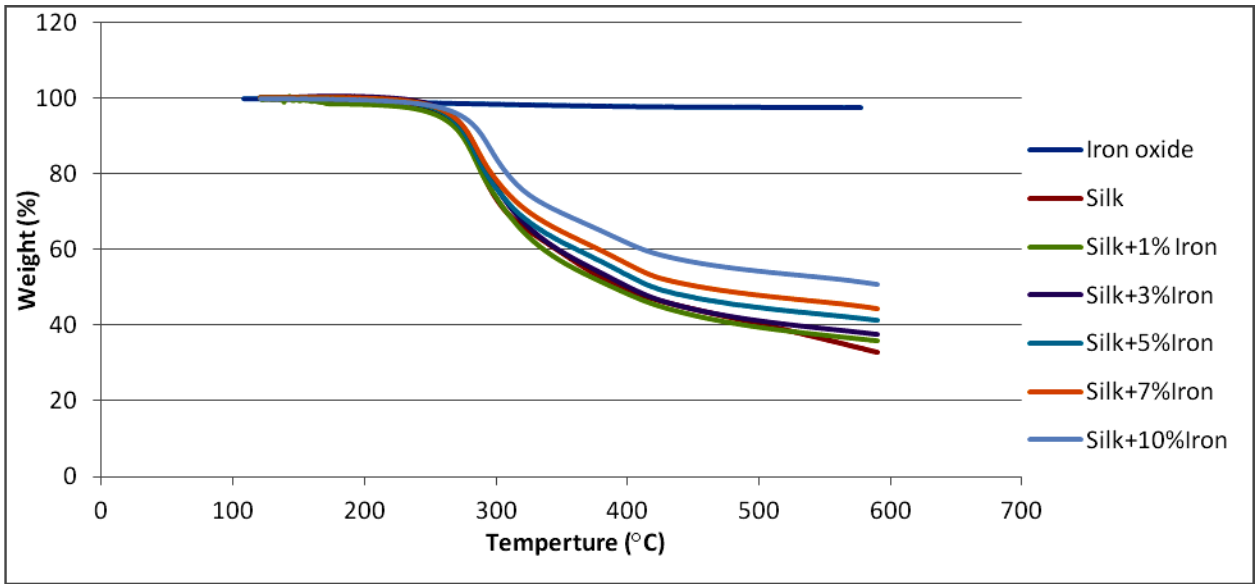

Figure 38: TGA curves of Fe_3O_4 powder and Silk scaffolds with variable concentrations of Fe_3O_4.

The thermograms obtained showed that the residue obtained for the silk + 10 wt. % Fe_3O_4 scaffold at 580°C was higher that obtained from other scaffolds prepared with lower concentrations of Fe_3O_4,

indicating that there might be more Fe_3O_4 content in silk + 10 wt. % Fe_3O_4 sample as compared to other samples with lower concentrations of Fe_3O_4.

4.9 MECHANICAL TEST ANALYSIS

Mechanical properties of the electrospun mats prepared at 20 KV using variable concentrations of Fe_3O_4 were analyzed. The mats were fully hydrated in DI water for 2 hours before the measurements and the measurements were carried out in PBS bath. The mats that were electrospun using SF/PEO produced an ultimate tensile strength (UTS) of 1.00 ± 0.3 MPa which was approximately 7 times more than that of the mat with highest concentration of Fe_3O_4 in it (10 wt. %) of 0.14 ± 0.02.

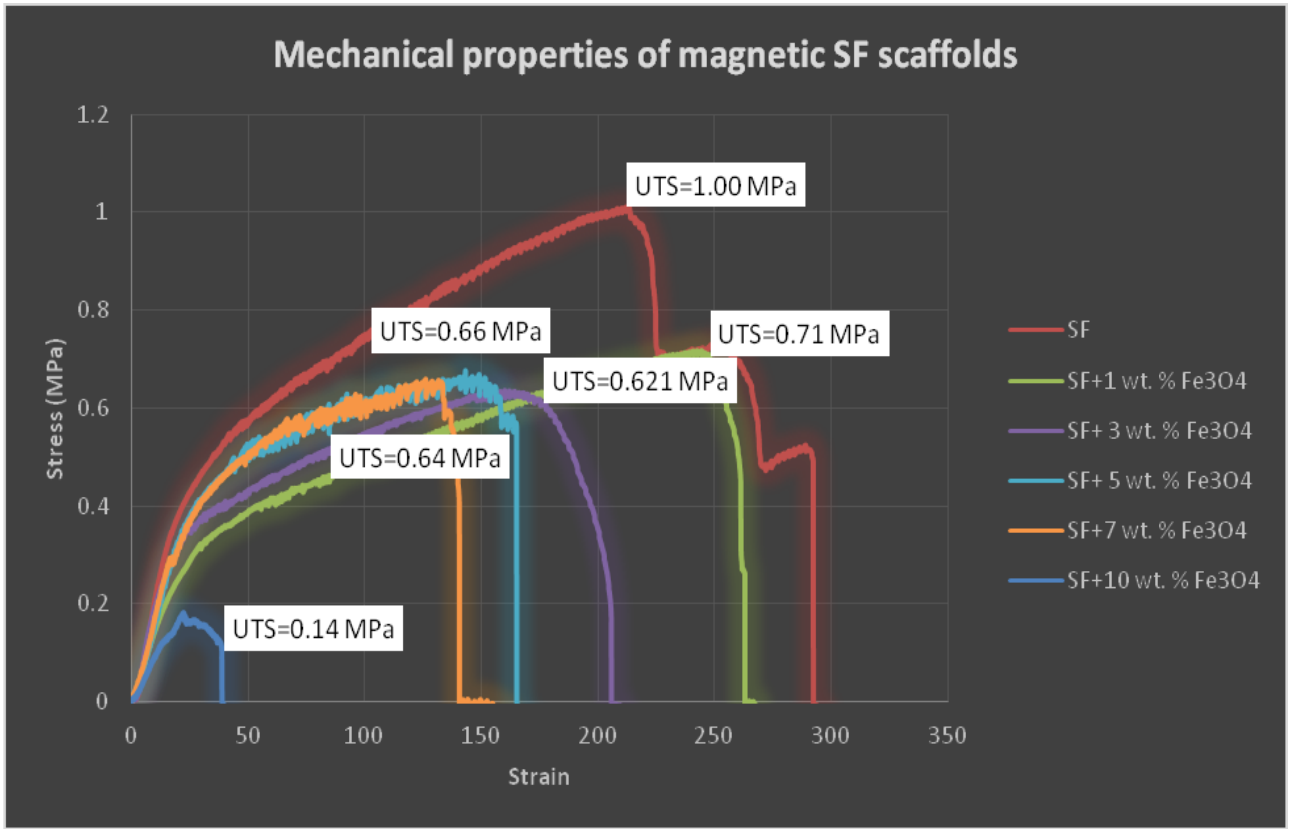

Figure 39: Demonstration of mechanical properties of the electrospun mats prepared at 20 KV with variable concentrations of Fe_3O_4.

The mats electrospun using SF/PEO produced a Young's Modulus of 3.34 ± 0.5 that made the mats 85 % stiffer than the mats electrospun with 10 wt. % Fe_3O_4 that produced the Young's modulus of 1.8 ± 0.12.

The decreased strength of the sample was most likely due to the fact that Fe_3O_4 particles or aggregates were forming a part of the fiber as seen under TEM which decreased the strength of the mat. It was easier to pull apart the mats that had fibers held by Fe_3O_4 particles as compared to SF mat consisting of only silk fibers. The mats prepared with lower concentrations of Fe_3O_4 had UTS and Young's Modulus lower than that of SF but higher than that of SF+ 10 wt. % Fe_3O_4 (Table 13).

Table 13: Summary of the mechanical properties of the electrospun mats with variable concentration of Fe_3O_4.

Sample	Ultimate Tensile Strength(UTS) (MPa)	Yield Strength (Mpa)	Young's Modulus (Mpa)
Electrospun Silk (7%)	1.00 ± 0.3	0.31 ± 0.03	3.34 ± 0.5
Silk+1%Fe_3O_4 (wt %)	0.710 ± 0.35	0.30 ± 0.09	2.56 ± 1.17
Silk+3%Fe_3O_4 (wt %)	0.62 ± 0.13	0.26 ± 0.01	2.4 ± 0.42
Silk+5%Fe_3O_4 (wt %)	0.66 ± 0.12	0.24 ± 0.02	2.3 ± 0.45
Silk+7%Fe_3O_4 (w %t)	0.64 ± 0.04	0.16 ± 0.02	2.1 ± 0.14
Silk+10%Fe_3O_4 (wt %)	0.14 ± 0.02	0.11 ± 0.01	1.8 ± 0.12

4.10 MAGNETIC MEASUREMENT ANALYSIS

To verify the magnetic properties of the samples electrospun at 20 KV with variable concentrations of Fe_3O_4, SQUID magnetometer was used. A comparison was made between the different samples based on its Magnetic Saturation and Magnetic Coercivity.

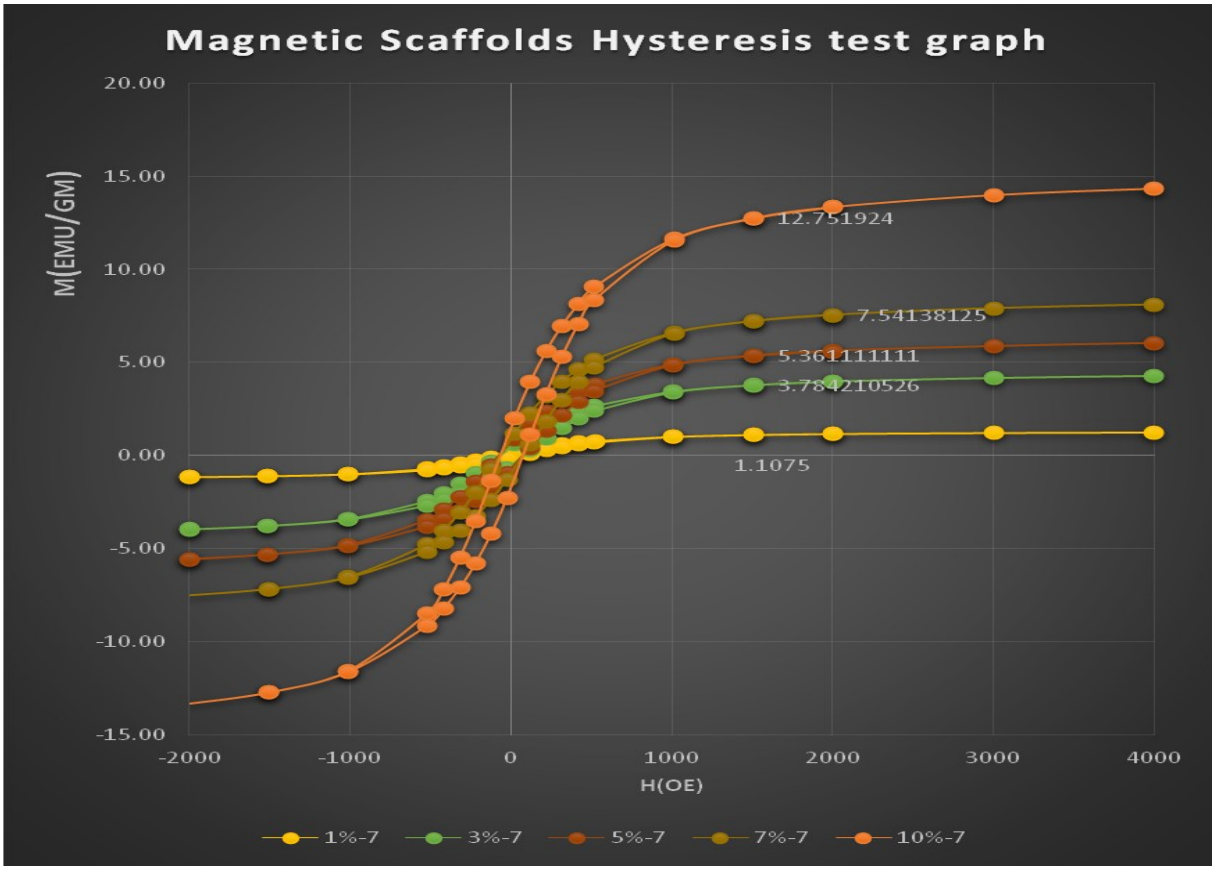

Figure 40: Hysteresis loop for the samples electrospun at 20 KV with variable concentrations of Fe_3O_4.All the samples were prepared using 7% SF and Fe_3O_4 concentrations of 1 wt. %, 3wt. %, 5 wt. %, 7 wt. % and 10 wt. %

Saturation magnetization (M_s) of the electrospun mat prepared using the maximum concentration of Fe_3O_4 (10 wt. %) was 12.75 emu/gm which was approximately 12 times more than that of the sample prepared using 1 wt. % Fe_3O_4 concentration of magnetic saturation value of 1.10 emu/gm. The magnetic saturation values of the samples electrospun using 3 wt. % Fe_3O_4, 5 wt. % Fe_3O_4 and 7 wt. % Fe_3O_4 were 3.74 emu/gm, 5.36 emu/gm and 7.54 emu/gm and was 70 %, 79 % and 85 % more than that of that of the sample prepared using 1 wt. % Fe_3O_4, respectively (Table 14).

Increase in the magnetic saturation with increase in the concentration of Fe_3O_4 is due to the increased number of magnetic domains in the Fe_3O_4 nanoparticles. To magnetically align all the domains in a

sample with high concentration of Fe_3O_4, more magnetic field is applied which further produces more changes in the magnetic flux leading to a high value of magnetic saturation.

Table 14: Comparison between magnetic saturation and coercivity values for all the samples with Fe_3O_4.

Fe_3O_4 (by wt)	Wt. of the sample(in gms)	Area of the sample(cm^2)	Magnetic Saturation, Ms (emu/gm)	Magnetic Coercivity, Hc (Oe)
1%	0.0040	1	1.1075	80 ± 5
3%	0.0019	1	3.743	80 ± 5
5%	0.0036	1	5.360	85 ± 10
7%	0.0016	1	7.541	85 ± 5
10%	0.0025	1	12.751	85 ± 5

The coercivity (Hc, Oe) is the external applied magnetic field necessary to return the material to a zero magnetization condition. As shown in Table 14, the coercivity increased from 80 ± 5 Oe for electrospun mats with 1 wt. % Fe_3O_4 to 85 ± 5 Oe for the mats with 10 wt. % Fe_3O_4. The enhanced coercivity of the samples with high concentration of Fe_3O_4 is due to the decreased interparticle dipolar interaction. This arises from the increased nanoparticle spacer distance for the single-domain nanoparticles as compared to the close contact of the pure iron oxide nanoparticles (Zhang et al., 2009). The interactions between the nanoparticles and SF solution can be responsible for coercivity enhancement.

4.11 CELL VIABILITY

The effect of the increase of Fe_3O_4 concentration in the electrospun mats on neuronal Schwann cells was evaluated using Alamar Blue. All the mats electrospun at 20 KV with variable concentrations of Fe_3O_4 had

shown to increase the cell growth between Day 1, Day 3, Day 5 and Day 7 signifying that silk fibroin scaffolds with Fe_3O_4 particles had no toxic effect on Schwann cells (Figure 41).

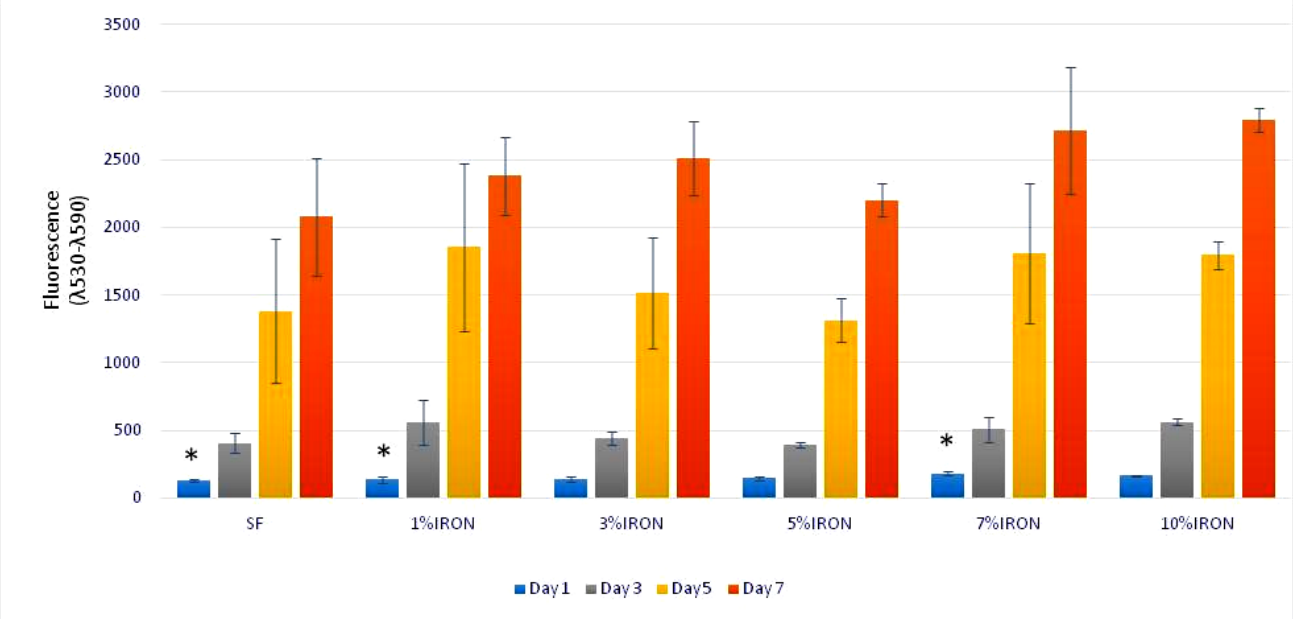

Figure 41: Alamar blue cell viability analysis for 6 different samples with variable concentrations of Fe_3O_4.

Although growth of Schwann cells was evident on all the samples by the end of Day 7, statistical differences were seen among 3 different scaffolds on Day 1. Schwann cells cultured on the scaffolds prepared using 7 wt. % Fe_3O_4 had shown to statistically reduce more Alamar blue indicating that there was an increase in the growth of the Schwann cells on these scaffolds as compared to the scaffolds prepared using SF with 0 wt. % Fe_3O_4 and 1 wt. % Fe_3O_4 on day 1. There was no significant difference seen among scaffolds prepared using variable concentration of Fe_3O_4 on Day 3, Day 5 and Day 7.Based on these results, it was confirmed that Fe_3O_4 content in the scaffolds, as high as 10 wt. %, did not affect the growth of Schwann cells and no signs of cytotoxicity were seen.

The increased growth of Schwann cells on scaffolds prepared using 7 wt. % Fe_3O_4 on Day 1 could be due to better cell adhesion and attachment on these scaffolds as compared to other scaffolds, which could

have led to more growth of Schwann cells on Day 1.Also, Schwann cell growth could have been stimulated by reactive oxygen species (ROS) induced by the metal ion, according to one of the hypothesis (Kim et al., 2011). It has been presumed that Fe ions are released from iron oxide nanoparticles inside the cells and these released ions enhance neurite outgrowth.

4.12 SEM IMAGES OF SCHWANNCELL GROWTH ON MAGNETIC SILK SCAFFOLDS

To better understand the morphology of the Schwann cells on magnetic silk scaffolds, the samples were fixed using paraformaldehyde and were imaged using scanning electron microscope. Everhart-Thornley side or an Inlens side secondary electron detector was used for imaging.

A very dense network of Schwann cells was seen on all the mats with different concentrations of Fe_3O_4 and on SF mats. The cells were seen well adhered to the mats and no signs of cytotoxicity were noticed even after Day 7. The cells seemed to be proliferating well and extending outgrowths on the mats. A lot of inter-connections were visible between the cells and multiple layers of cells were observed on mats with 10 wt. % Fe_3O_4 (Figure 42-43).

After one week of culture on the scaffolds, extracellular matrix was laid down by the Schwann cells. The extracellular matrix had both mesh-like areas and individual fibrils.

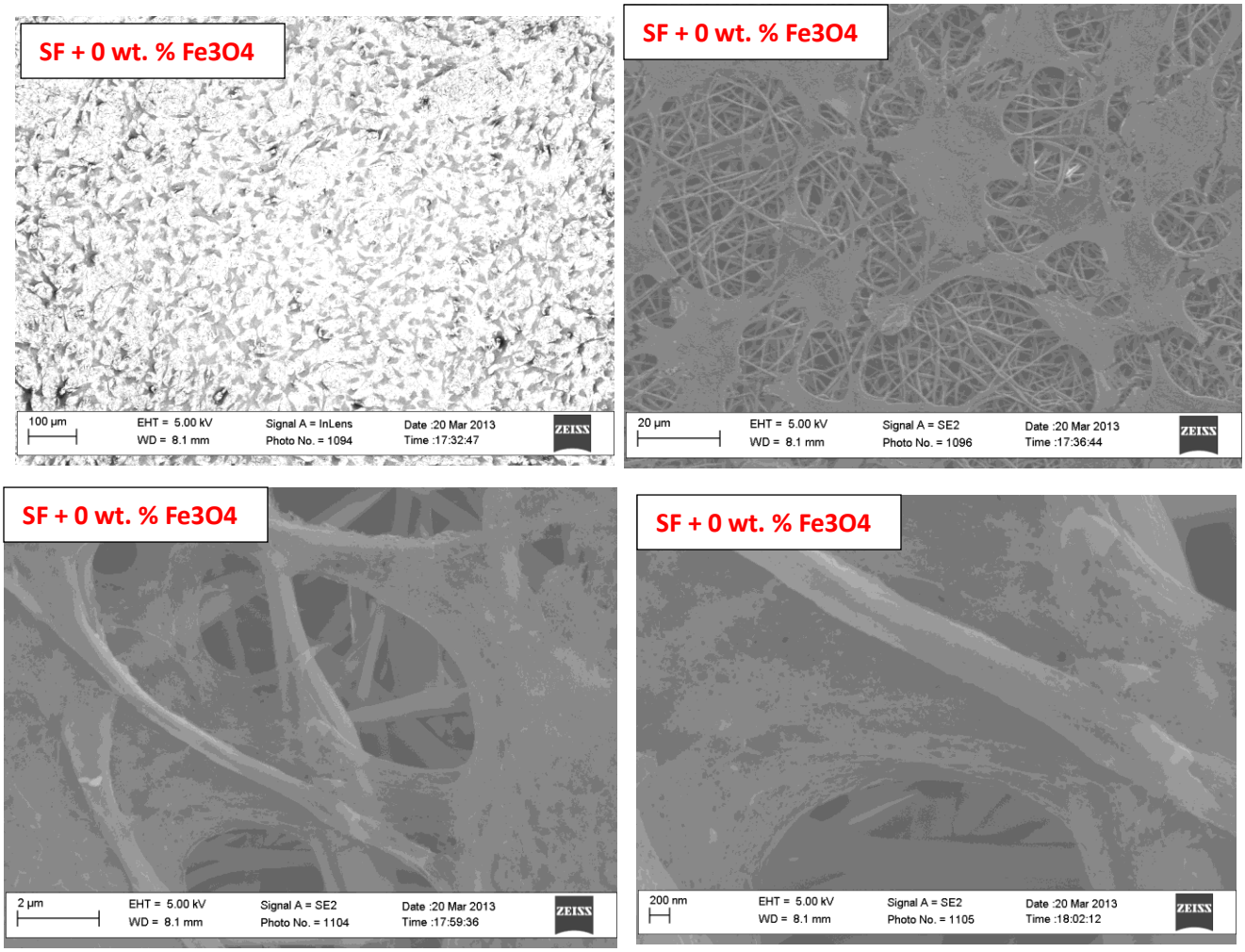

Figure 42: SEM images of the Schwann cells cultured on SF electrospun mats at low and high magnification.

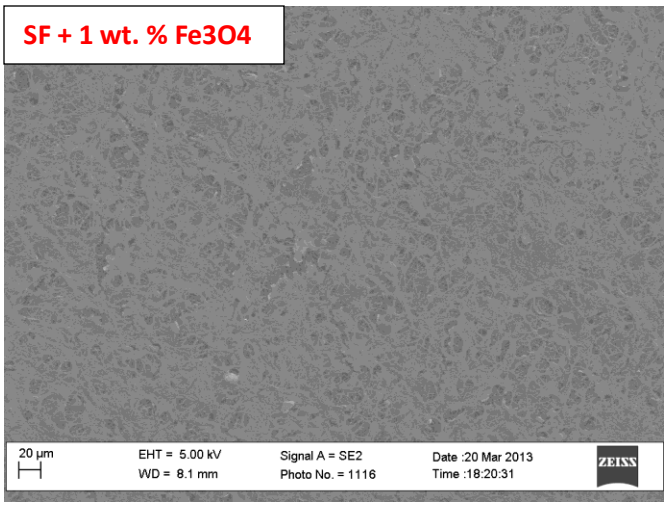
SF + 1 wt. % Fe3O4
20 µm
EHT = 5.00 kV
WD = 8.1 mm
Signal A = SE2
Photo No. = 1116
Date :20 Mar 2013
Time :18:20:31
ZEISS

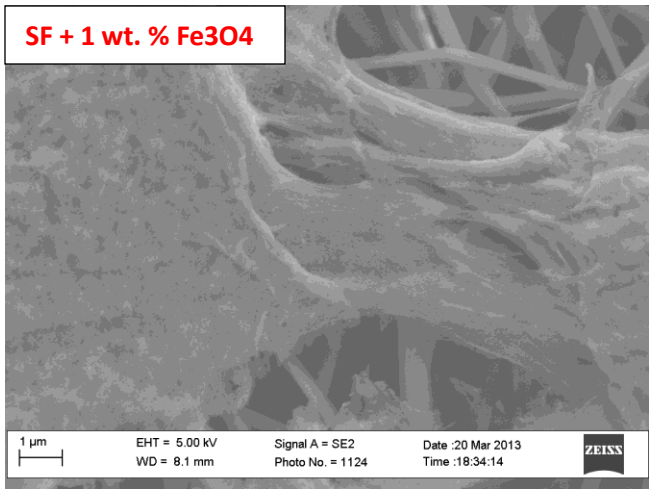
SF + 1 wt. % Fe3O4
1 µm
EHT = 5.00 kV
WD = 8.1 mm
Signal A = SE2
Photo No. = 1124
Date :20 Mar 2013
Time :18:34:14
ZEISS

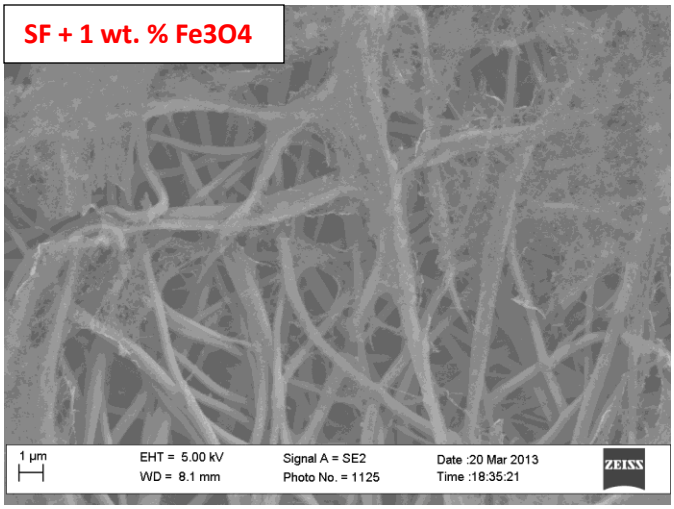
SF + 1 wt. % Fe3O4
1 µm
EHT = 5.00 kV
WD = 8.1 mm
Signal A = SE2
Photo No. = 1125
Date :20 Mar 2013
Time :18:35:21
ZEISS

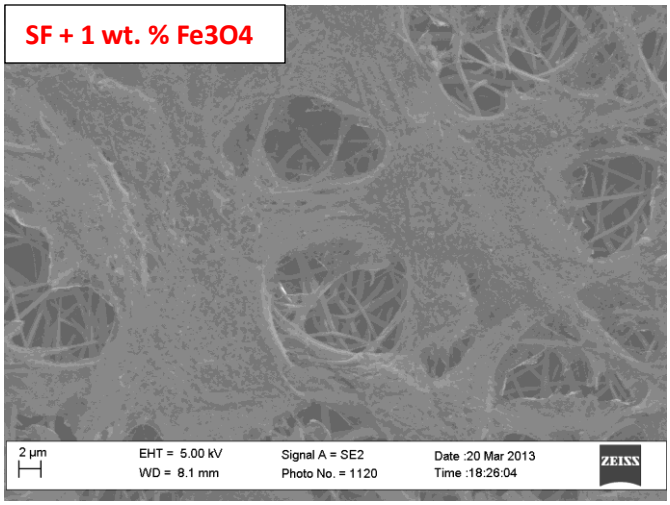
SF + 1 wt. % Fe3O4
2 µm
EHT = 5.00 kV
WD = 8.1 mm
Signal A = SE2
Photo No. = 1120
Date :20 Mar 2013
Time :18:26:04
ZEISS

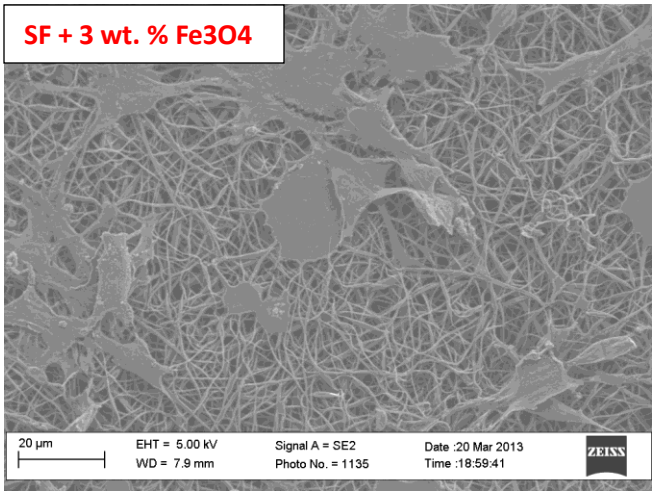
SF + 3 wt. % Fe3O4
20 µm
EHT = 5.00 kV
WD = 7.9 mm
Signal A = SE2
Photo No. = 1135
Date :20 Mar 2013
Time :18:59:41
ZEISS

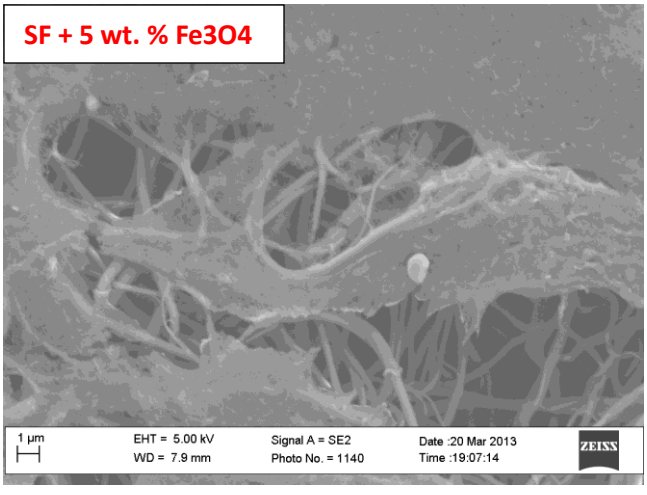
SF + 5 wt. % Fe3O4
1 µm
EHT = 5.00 kV
WD = 7.9 mm
Signal A = SE2
Photo No. = 1140
Date :20 Mar 2013
Time :19:07:14
ZEISS

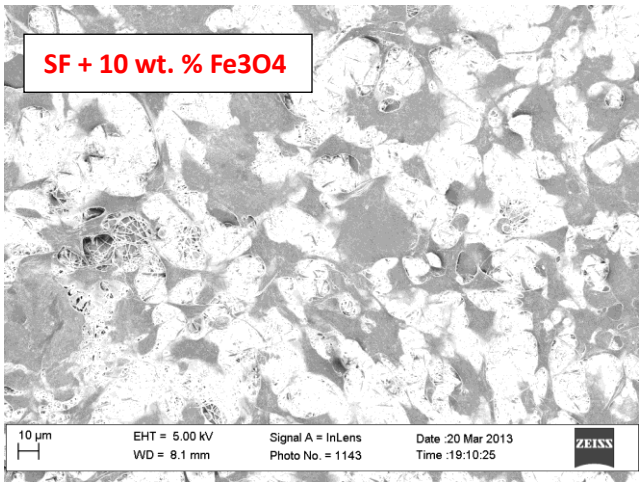

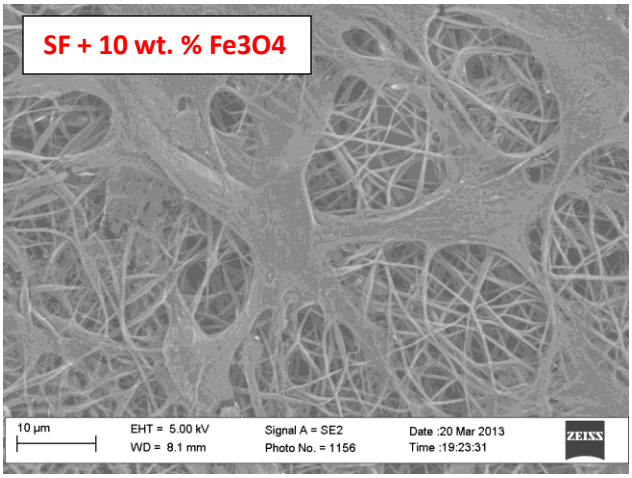

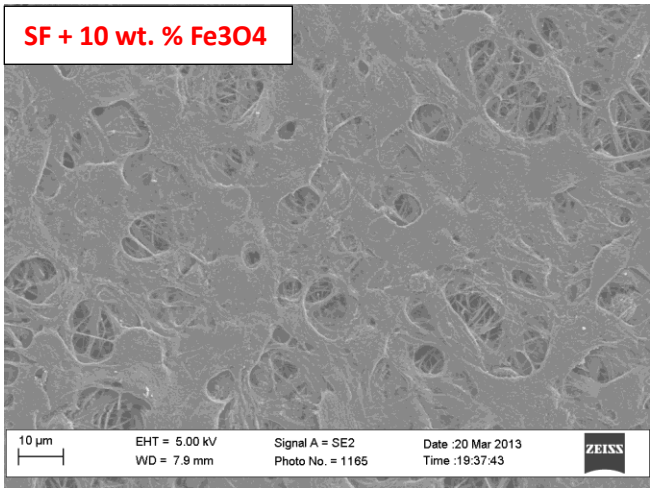

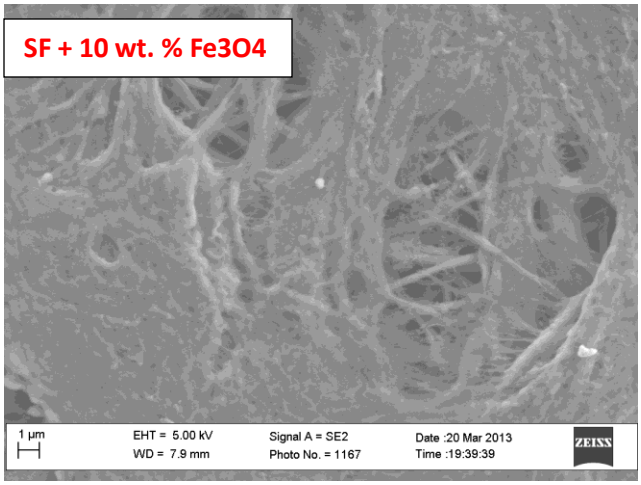

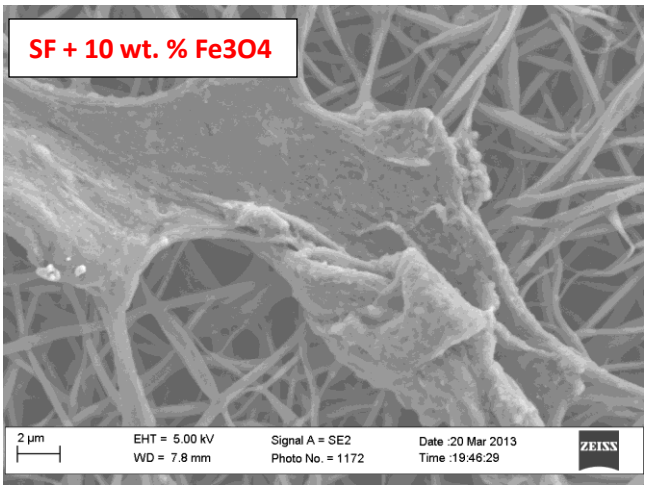

Figure 43: SEM images of the Schwann cells cultured for 7 days on SF electrospun mats with variable concentrations of Fe_3O_4, at low and high magnification.

Measurement and comparison of Schwann cell outgrowth was not possible due to the dense network of cells and inter-connections formed by Schwann cells with each other.

4.13 ELISA- NGF QUANTIFICATION

The level of Nerve growth Factor (NGF) was analyzed in the culture medium after Day 1 and Day 7 and also in the electrospun scaffolds by dissolving the mats in HFIP and resuspending in PBS, as described above, using enzyme linked immunosorbent assay.

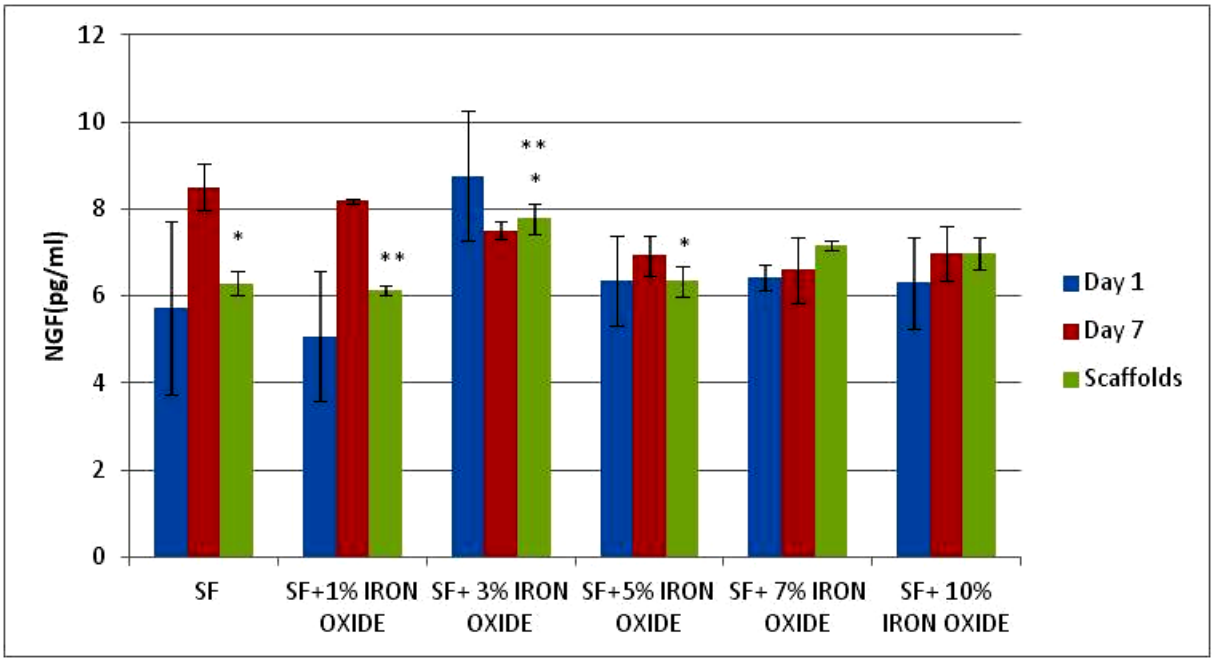

Figure 44: Quantification of NGF in culture media after Day 1 and Day 7 and in scaffolds at day 7.

The level of NGF in the culture medium on Day 1 and Day 7 for all the samples was similar and no significant difference was found . The result demonstrates that electrospun silk fibroin scaffold and scaffolds with Fe_3O_4 concentration as high as 10 wt.% did not affect the expression of NGF, indicating that there was no cytotoxic effect of the scaffolds on Schwann cells.

Also, based on ANOVA results, a significant increase in the NGF levels with increase in concentration of Fe_3O_4 in the scaffolds was seen when scaffolds were dissolved and resuspended. The scaffolds with Fe_3O_4 concentration of 3 wt % had more NGF (pg/ml) than the scaffolds with Fe_3O_4 concentration of 1 wt% and 0 wt%. On the contrary, there was a decrease in the NGF level in the scaffold with 5 wt. % Fe_3O_4.

The decrease in the NGF level in the scaffold with 5 wt. % Fe_3O_4 could be due to the low secretion of NGF by Schwann cells or due to less thickness of the mat as compared to the other mats. Since the data for the thickness of the mats is not available, the reason for low level of NGF in these mats is unknown.

CHAPTER 5: CONCLUSION

In conclusion, this work effectively designed magnetic electrospun silk fibroin scaffolds with varying concentrations of Fe_3O_4 using the technique of electrospinning. Processing parameters were established using SEM images. Voltage of 20 KV was used to electrospin all the samples and highest concentration of Fe_3O_4 nanopowder used was 10 wt. %. Total volume of the solution used was 5 ml for preparing all the samples at a constant flow rate of 2ml/hr and fixed distance of 19 cm using a flat rotating collector. It was demonstrated that Fe_3O_4 nanoparticles and aggregates were successfully incorporated in the mat using SEM and TEM analysis and fiber morphology was also studied using these techniques. The mechanical strength of the fibers was also tested and it was found out that SF mat had more strength than the mats with Fe_3O_4 nanoparticles incorporated in it. Magnetic measurements were carried out to verify the magnetic properties of the mat. As expected, the value of magnetic saturation increased with the increase in the concentration of Fe_3O_4 nanopowder in the electrospun mats. FTIR and XRD was performed to analyze the structural changes in the electrospun silk fibroin mats with the incorporation of Fe_3O_4. FTIR deconvolution lead to the result that strong beta sheet content indicating the presence of Silk II structure was dominant in all the samples. XRD analysis indicated the interactions between Silk and Fe_3O_4 particles. In vitro studies were carried out using neuronal Schwann cells. Growth and proliferation of Schwan cells were monitored over a period of one week. Seeding density was optimized to 25000 cells/ well. All the studies were carried out in triplicates. Neuronal Schwann cells attached and were viable on magnetic silk scaffolds over 1 week. Alamar blue test was done to test cell viability. Schwann cell outgrowth was observed on all the samples using SEM. Statistical analysis (ANOVA with multiple tukey's test) was performed and it was established that Schwann cell's growth & NGF levels in the dissolved scaffolds was supported on SF scaffolds as well as scaffolds with Fe_3O_4 in it.

CHAPTER 6: FUTURE DIRECTIONS

The novel magnetic silk scaffolds prepared during this study using variable concentrations of Fe_3O_4 were a part of the preliminary studies done to understand the response of Schwann cells toward the Fe_3O_4 nanoparticles embedded and incorporated in electrospun silk fibroin mats.

In the past, electrical stimulation of different cells has proven to be effective in enhancing the growth of the cells on different types of scaffolds. It would be interesting to magnetically stimulate the novel magnetic silk scaffolds prepared during this study and monitor their growth patterns.

Since Schwann cells play a major role in the axon regeneration, these magnetic silk scaffolds can serve as scaffolds to study the co-cultures of nerve cell lines such as PC-12 cells and Schwann cells without and with the presence of magnetic fields.

These studies can be carried out with some variations such as dip coating method to coat the already prepared electrospun silk mats to increase the contact surface area of magnetic particles with Schwann cells and other cell lines.

Different types of rotating mandrel collectors, other than the ones used in this study, can be optimized to electrospin these magnetic silk scaffolds to prepare mats with aligned fibers and also to prepare those mats as nerve conduits that can be magnetically stimulated to study Schwann cells and other nerve cells seeded on the conduits.

One exciting possibility of magnetic hyperthermia offered by magnetic nanoparticles can be exploited on these mats to study the effects of heat generated by magnetic nanoparticles when magnetically stimulated on cancerous cell lines.

These mats can be implanted in vivo and the magnetic particles incorporated in the mats can serve as contrast agents if labelled or as drug delivery carriers if coated with drugs which can then be stimulated to release drugs and the mats can serve as scaffolds for cell growth on the same site.

WORK CITED

Altman, G. H., Diaz, F., Jakuba, C., Calabro, T., Horan, R. L., Chen, J., ... & Kaplan, D. L. (2003). Silk-based biomaterials. *Biomaterials*, *24*(3), 401-416.

Bonhoeffer, F. (1994). Perspectives on axonal regeneration in the mammalian CNS. Trends *in neurosciences*, 17(11), 473-479.

Bunge, R. P. (1994). The role of the Schwanncell in trophic support and regeneration. *Journal of neurology*, *242*(1), S19-S21.

Cebe, P., Hu, X., Kaplan, D. L., Zhuravlev, E., Wurm, A., Arbeiter, D., & Schick, C. (2013). Beating the Heat-Fast Scanning Melts Silk Beta Sheet Crystals. *Scientific reports*, *3*.

Chen, L., Xie, J., Yancey, J., Srivatsan, M., & Varadan, V. K. (2007, April). Experimental investigation of magnetic nanotubes in PC-12 neuron cells culturing. In The 14th International Symposium on: *Smart Structures and Materials & Nondestructive Evaluation and Health Monitoring* (pp. 65280L-65280L). International Society for Optics and Photonics.

Chicea, D. (2009). Revealing Fe_3O_4 nanoparticles aggregation dynamics using dynamic light scattering. *Optoelectronics and Advanced Materials–Rapid Communications*, 3(12), 1299-1305.

Christopherson, G. T., Song, H., & Mao, H. Q. (2009). The influence of fiber diameter of electrospun substrates on neural stem cell differentiation and proliferation. *Biomaterials*, 30(4), 556-564.

Deumens, R., Bozkurt, A., Meek, M. F., Marcus, M. A., Joosten, E. A., Weis, J., & Brook, G. A. (2010). Repairing injured peripheral nerves: bridging the gap. *Progress in neurobiology*, *92*(3), 245-276.

Dunning, M. D., Lakatos, A., Loizou, L., Kettunen, M., Brindle, K. M., & Franklin, R. J. (2004). Superparamagnetic iron oxide-labeled Schwann cells and olfactory ensheathing cells can be traced in vivo by magnetic resonance imaging and retain functional properties after transplantation into the CNS. *The Journal of neuroscience*, *24*(44), 9799-9810.

Evans, G. R. (2000, October). Challenges to nerve regeneration. In *Seminars in surgical oncology* (Vol. 19, No. 3, pp. 312-318). John Wiley & Sons, Inc.

Feinberg, A. W. (2012). Engineered tissue grafts: opportunities and challenges in regenerative medicine. *Wiley Interdisciplinary Reviews: Systems Biology and Medicine*, 4(2), 207-220.

Guest, J. D., Hesse, D., Schnell, L., Schwab, M. E., Bunge, M. B., & Bunge, R. P. (1997). Influence of IN-1 antibody and acidic FGF-fibrin glue on the response of injured corticospinal tract axons to human Schwanncell grafts.*Journal of neuroscience research*, *50*(5), 888-905

Heath, C. A., & Rutkowski, G. E. (1998). The development of bioartificial nerve grafts for peripheral-nerve regeneration. *Trends in biotechnology*, 16(4), 163-168.

Hu, A., Zuo, B., Zhang, F., Lan, Q., & Zhang, H. (2012). Electrospun silk fibroin nanofibers promote Schwanncell adhesion, growth and proliferation. *Neural Regeneration Research(English)*, *7*(15).

Hu, X., Kaplan, D., & Cebe, P. (2006). Determining beta-sheet crystallinity in fibrous proteins by thermal analysis and infrared spectroscopy.*Macromolecules*, *39*(18), 6161-6170

Huang, W., Begum, R., Barber, T., Ibba, V., Tee, N. C. H., Hussain, M., ... & Priestley, J. V. (2012). Regenerative potential of silk conduits in repair of peripheral nerve injury in adult rats. *Biomaterials*, *33*(1), 59-71.

Huang, Y. C., & Huang, Y. Y. (2006). Biomaterials and strategies for nerve regeneration. *Artificial organs*, 30(7), 514-522..

Huang, Y. C., & Huang, Y. Y. (2006). Tissue engineering for nerve repair.*Biomedical Engineering: Applications, Basis and Communications*, *18*(03), 100-110.

Huang, Z. M., Zhang, Y. Z., Kotaki, M., & Ramakrishna, S. (2003). A review on polymer nanofibers by electrospinning and their applications in nanocomposites. *Composites science and technology*, *63*(15), 2223-2253.

Jin, H. J., Park, J., Karageorgiou, V., Kim, U. J., Valluzzi, R., Cebe, P., & Kaplan, D. L. (2005). Water-Stable Silk Films with Reduced β-Sheet Content.*Advanced Functional Materials*, *15*(8), 1241-1247

Johnsen, S., & Lohmann, K. J. (2005). The physics and neurobiology of magnetoreception. *Nature Reviews Neuroscience*, 6(9), 703-712.

Jose, R. R., Elia, R., Firpo, M. A., Kaplan, D. L., & Peattie, R. A. (2012). Seamless, axially aligned, fiber tubes, meshes, microbundles and gradient biomaterial constructs. *Journal of Materials Science: Materials in Medicine*,*23*(11), 2679-2695.

Kavich, D. W., Hasan, S. A., Mahajan, S. V., Park, J. H., & Dickerson, J. H. (2010). Field dependence of the spin relaxation within a film of iron oxide nanocrystals formed via electrophoretic deposition. *Nanoscale research letters*, 5(10), 1540-1545.

Keirstead, H. S., Nistor, G., Bernal, G., Totoiu, M., Cloutier, F., Sharp, K., & Steward, O. (2005). Human embryonic stem cell-derived oligodendrocyte progenitor cell transplants remyelinate and restore locomotion after spinal cord injury. *The Journal of Neuroscience*, *25*(19), 4694-4705.

Kenawy, E. R., Abdel-Hay, F. I., El-Newehy, M. H., & Wnek, G. E. (2009). Processing of polymer nanofibers through electrospinning as drug delivery systems. *Materials Chemistry and Physics*, *113*(1), 296-302.

Kim, J. A., Lee, N., Kim, B. H., Rhee, W. J., Yoon, S., Hyeon, T., & Park, T. H. (2011). Enhancement of neurite outgrowth in PC12 cells by iron oxide nanoparticles. *Biomaterials*, *32*(11), 2871-2877.

Lawrence, B. D., Omenetto, F., Chui, K., & Kaplan, D. L. (2008). Processing methods to control silk fibroin film biomaterial features. *Journal of materials science*, *43*(21), 6967-6985.

Lawrence, B. D., Wharram, S., Kluge, J. A., Leisk, G. G., Omenetto, F. G., Rosenblatt, M. I., & Kaplan, D. L. (2010). Effect of hydration on silk film material properties. *Macromolecular bioscience*, *10*(4), 393-403.

Levenberg, S., & Langer, R. (2004). Advances in tissue engineering. *Current topics in developmental biology*, *61*, 113-134.

Li, C., Vepari, C., Jin, H. J., Kim, H. J., & Kaplan, D. L. (2006). Electrospun silk-BMP-2 scaffolds for bone tissue engineering. *Biomaterials*, *27*(16), 3115-3124

Liu, Y., Dong, L., Fan, J., Wang, R., & Yu, J. Y. (2011). Effect of applied voltage on diameter and morphology of ultrafine fibers in bubble electrospinning.*Journal of Applied Polymer Science*, *120*(1), 592-598.

Lu, Q., Hu, X., Wang, X., Kluge, J. A., Lu, S., Cebe, P., & Kaplan, D. L. (2010). Water-insoluble silk films with silk I structure. *Acta biomaterialia*, *6*(4), 1380-1387.

Madduri, S., Papaloizos, M., & Gander, B. (2010). Trophically and topographically functionalized silk fibroin nerve conduits for guided peripheral nerve regeneration. *Biomaterials*, *31*(8), 2323-2334.

Markides, H., Rotherham, M., & El Haj, A. J. (2012). Biocompatibility and toxicity of magnetic nanoparticles in regenerative medicine. *Journal of Nanomaterials*, 2012, 13

Nectow, A. R., Marra, K. G., & Kaplan, D. L. (2011). Biomaterials for the development of peripheral nerve guidance conduits. *Tissue Engineering Part B: Reviews*, *18*(1), 40-50.

Pfister, B. J., Gordon, T., Loverde, J. R., Kochar, A. S., Mackinnon, S. E., & Cullen, D. K. (2011). Biomedical engineering strategies for peripheral nerve repair: surgical applications, state of the art, and future challenges. *Critical Reviews™ in Biomedical Engineering*, *39*(2).

Pisanic II, T. R., Blackwell, J. D., Shubayev, V. I., Fiñones, R. R., & Jin, S. (2007). Nanotoxicity of iron oxide nanoparticle internalization in growing neurons. *Biomaterials*, *28*(16), 2572-2581.

Rockwood, D. N., Preda, R. C., Yücel, T., Wang, X., Lovett, M. L., & Kaplan, D. L. (2011). Materials fabrication from Bombyx mori silk fibroin. *Nature protocols*, *6*(10), 1612-1631.

Rudge, S. R., Kurtz, T. L., Vessely, C. R., Catterall, L. G., & Williamson, D. L. (2000). Preparation, characterization, and performance of magnetic iron–carbon composite microparticles for chemotherapy. *Biomaterials*, *21*(14), 1411-1420.

Safarik, I., & Safarikova, M. (2009). Magnetically responsive nanocomposite materials for bioapplications. *Solid State Phenomena*, *151*, 88-94.

Šafařík, I., Horská, K., & Šafaříková, M. (2011). Magnetic nanoparticles for biomedicine. In *Intracellular Delivery* (pp. 363-372). Springer Netherlands.

Schmidt, C. E., & Leach, J. B. (2003). Neural tissue engineering: strategies for repair and regeneration. *Annual review of biomedical engineering*, 5(1), 293-347.

Schneider, A., Wang, X. Y., Kaplan, D. L., Garlick, J. A., & Egles, C. (2009). Biofunctionalized electrospun silk mats as a topical bioactive dressing for accelerated wound healing. *Acta biomaterialia*, 5(7), 2570-2578.

Siemionow, M., & Brzezicki, G. (2009). Current techniques and concepts in peripheral nerve repair. *International review of neurobiology*, 87, 141-172.

Valluzzi, R., Gido, S. P., Zhang, W., Muller, W. S., & Kaplan, D. L. (1996). Trigonal crystal structure of bombyx mori silk incorporating a threefold helical chain conformation found at the air-water interface. *Macromolecules*, *29*(27), 8606-8614

Wang, G., Hu, X., Lin, W., Dong, C., & Wu, H. (2011). Electrospun PLGA–silk fibroin–collagen nanofibrous scaffolds for nerve tissue engineering. *In Vitro Cellular & Developmental Biology-Animal*, *47*(3), 234-240.

Wang, X., Wenk, E., Zhang, X., Meinel, L., Vunjak-Novakovic, G., & Kaplan, D. L. (2009). Growth factor gradients via microsphere delivery in biopolymer scaffolds for osteochondral tissue engineering. *Journal of Controlled Release*, 134(2), 81-90.

Wang, X., Yucel, T., Lu, Q., Hu, X., & Kaplan, D. L. (2010). Silk nanospheres and microspheres from silk/pva blend films for drug delivery. *Biomaterials*, *31*(6), 1025-1035.

Wang, Y., Blasioli, D. J., Kim, H. J., Kim, H. S., & Kaplan, D. L. (2006). Cartilage tissue engineering with silk scaffolds and human articular chondrocytes. *Biomaterials*, *27*(25), 4434-4442.

Wood, M. D., Kemp, S. W., Weber, C., Borschel, G. H., & Gordon, T. (2011). Outcome measures of peripheral nerve regeneration. *Annals of Anatomy-Anatomischer Anzeiger*, *193*(4), 321-333.

Xie, J., MacEwan, M. R., Schwartz, A. G., & Xia, Y. (2010). Electrospun nanofibers for neural tissue engineering. *Nanoscale*, *2*(1), 35-44.

Xu, S., Yan, X., Zhao, Y., Wang, W., & Yang, Y. (2011). In vitro biocompatibility of electrospun silk fibroin mats with Schwann cells. *Journal of Applied Polymer Science*, *119*(6), 3490-3494.

Xu, X. M., Guénard, V., Kleitman, N., Aebischer, P., & Bunge, M. B. (1995). A combination of BDNF and NT-3 promotes supraspinal axonal regeneration into Schwanncell grafts in adult rat thoracic spinal cord. *Experimental neurology*,*134*(2), 261-272.

Yan, X., & Gevelber, M. (2010). Investigation of electrospun fiber diameter distribution and process variations. *Journal of Electrostatics*, *68*(5), 458-464.

Yang, Y., Ding, F., Wu, J., Hu, W., Liu, W., Liu, J., & Gu, X. (2007). Development and evaluation of silk fibroin-based nerve grafts used for peripheral nerve regeneration. *Biomaterials*, *28*(36), 5526-5535

Yarin, A. L., Koombhongse, S., & Reneker, D. H. (2001). Bending instability in electrospinning of nanofibers. *Journal of Applied Physics*, *89*(5), 3018-3026.

Yeong, W. Y., Chua, C. K., Leong, K. F., & Chandrasekaran, M. (2004). Rapid prototyping in tissue engineering: challenges and potential. *TRENDS in Biotechnology*, *22*(12), 643-652.

Zhang, D., Karki, A. B., Rutman, D., Young, D. P., Wang, A., Cocke, D., ... & Guo, Z. (2009). Electrospun polyacrylonitrile nanocomposite fibers reinforced with Fe_3O_4nanoparticles: Fabrication and property analysis. *Polymer*, *50*(17), 4189-4198

Zhang, X., Reagan, M. R., & Kaplan, D. L. (2009). Electrospun silk biomaterial scaffolds for regenerative medicine. *Advanced drug delivery reviews*, *61*(12), 988-1006

Zhu, J., Shao, H., & Hu, X. (2007). Morphology and structure of electrospun mats from regenerated silk fibroin aqueous solutions with adjusting pH.*International journal of biological macromolecules*, *41*(4), 469-474.

Ziv-Polat, O., Skaat, H., Shahar, A., & Margel, S. (2012). Novel magnetic fibrin hydrogel scaffolds containing thrombin and growth factors conjugated iron oxide nanoparticles for tissue engineering. *International journal of nanomedicine*, *7*, 1259.